A low–frequency hyperthermia system for *malignant cervic melanoma* treatment

Michał Patryk Dębicki

Ph.D. Thesis

Technical University of Gdańsk

Supervisor: Prof. Michał Mrozowski

Gdańsk 1999

"Są ludzie, którzy pragną wiedzieć jedynie po to, aby wiedzieć: jest to niska ciekawość. Inni chcą wiedzieć po to, aby w ten sposób zyskać rozgłos: jest to haniebna próżność (...). Są i tacy, którzy nabywają wiedzę, by za jej pośrednictwem zdobyć pieniądze lub zaszczyty: ich motyw jest wstrętny. Niektórzy jednak chcą wiedzieć w celu zbudowania: jest to miłość. Inni po to aby się zbudować: jest to mądrość.

Tylko ci, którzy należą do dwóch ostatnich kategorii nie nadużywają wiedzy, ponieważ jedynie oni chcą pojmować, by dobrze czynić."

Bernard z Clairvaux

Contents

Chapter 1

General introduction

1.1 Motivation and background

In recent years cancer has become one of the main reasons of human death. Among many different neoplasms, the carcinoma of the cervix is the one (after breast cancer), which is the most frequently observed in female population. In the United States the carcinoma of the cervix is diagnosed in under 16 thousand patients per annum with localized disease being present in 51%, regional disease in 33% and metastatic tumor in 8% of patients [42]. This malignancy, on the other hand, is much more common in Poland and it is also found with more advanced stages at diagnosis. This is reflected in the comparative death rate per 100,000 population in both countries. It is 2.6 per 100,000 in the United States and 7.7 in Poland [42].

The medicine uses several methods of cancer treatment with an alternate success, depending on a case and a stage of the disease. Usually, the combination of different methods increases the possibility of an effective treatment, thus already well founded modalities, like surgery, chemotherapy and radiotherapy are used synergetically.

In last decades also hyperthermia (HT) has been established as an adjuvant method to already existent ones. The HT is performed, in most cases, in combination with radiotherapy, yet also the fusion with other established techniques is common [27, 52].

1.1.1 Hyperthermia

1.1.1.1 Hyperthermia and its physiological effects

Hyperthermia is defined as an increase of tissue temperature above values set by a body's thermo-regulation mechanism, i.e. between 42°C and 48°C. This temperature increase has an equivalent implication to both malignant and healthy tissues and may destroy them by damage to cell nuclei, to membranes and other cytoplasmic components. Yet there are other mechanisms that play an important role in cancer

treatment. Hyperthermia, by delivering thermal energy, may stimulate an organism to increase a blood flow in order to remove the heat excess and supply cells with necessary nutrition material and oxygen. In malignant tumors, however, due to poor vascularization, the blood flow may not be increased and thus prolonged heating periods are much worse tolerated. Not only does this lead to necrotic areas in solid tumors, but also to low pH and deficiency of oxygen and nutritient, making the cells more sensitive to radiotherapy [51, 24, 78]. On the other hand, the HT enhances the effect of ionizing radiation on cells, inhibiting the repair of radiation induced DNA damage [33]. Moreover, it has been proved that the cells are the most sensitive to hyperthermia during the DNA reproduction phase (so called S–phase) [78], the phase that is the most resistant to radiation.

The thermo-tolerance, which is a transient state of resistance to heat treatment, is an important effect induced by the HT, which needs to be considered in order to determine the time interval between successive treatments. In vivo experiments show, that this phenomenon reaches its maximum 16 hours after the heat was brought on and totally disappears after 120 hours [36]. The thermo-tolerance also reduces the degree of thermal radiosensitisation.

1.1.1.2   Heating technology

Numerous means exist to raise a body temperature, among which the electromagnetic radiation is the most commonly used one. Due to different tumor placements in a human body, various methods of heat delivery into different regions have been developed. Depending on the volume of the heated region, one can differentiate the whole body, regional and local hyperthermia. Alternatively the hyperthermia can be divided into localized current field (LCF) (or low frequency), radio frequency (RF) and microwave, when the frequency of operation is applied as the main criterion.

The LCF HT systems operate in frequency range of 500 kHz to 1 MHz. The electrodes make a galvanic contact with tissue and the temperature is raised up by Joule's losses of conductive current flowing among electrodes.

The RF hyperthermia is characterized by two frequency ranges. The lower, between 8 and 30 MHz, usually used with interstitial or intracavitary applicators placed in plastic catheters (using capacitively coupled or inductive technique), and the upper, between 60 and 120 MHz, which is ordinarily applied with radiative phased arrays.

The microwave HT is defined above 300 MHz and the usual ISM frequencies are used (434, 915 and 2450 MHz). At these frequencies the conductive current is negligible and the displacement current due to dielectric losses make the tissue temperature raise up.

<center>a)   b)</center>
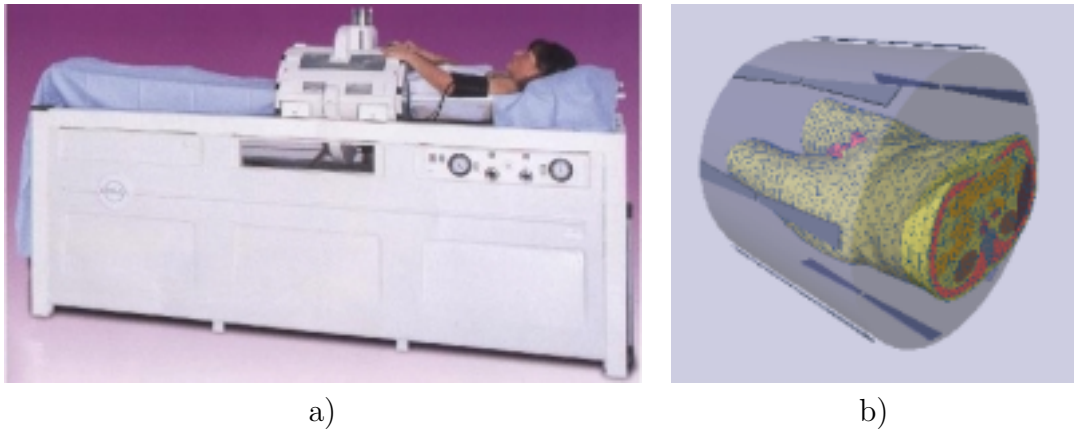
Figure 1.1: *BSD2000 device as an example of regional RF hyperthermia with annular array antennas (a) and a view of a treatment planning software (b), which identifies an internal organs based on magnetic resonance (MRI) slices. Such a device is very expensive, and a generation of a grid requires one day in order to adapt data obtained from the MRI*

The therapeutic effects of whole body hyperthermia is usually related to an upregulation of the immune response or to the temperature enhanced activity of cytostatic drugs and hence, in most cases, are not connected to the electromagnetic radiation.

The regional heating is usually applied to large, deep seated tumors with annular array antennas [58, 59, 35] (see Figure 1.1), waveguide systems [14], coaxial TEM waveguides [17] or capacitively coupled devices [23]. The main problem of the regional HT is precise focusing of the power in a tumor. This difficulty often leads to overheating of healthy regions and causes the lack of therapeutic temperature range in a pathological tissue. This problem is reflected in thermal stress and pain during treatment, which is the main reason of a trial suspensions [17, 19, 18, 68, 16, 57, 70, 64, 76]. Many problems have been overcome by precise treatment planning and optimization study with the sophisticated software systems [66, 61] which find the optimal configurations for applicator excitement (adjustment of amplitudes and phases) and a patients' position within an applicator. Nevertheless, one needs to keep in mind that these software systems rely on a high number of physical parameters (tissues such as skin, fat, bone, muscle with different perfusion rates are to be approximated) in conjunction with biological and subjective variations and in many cases it is still not possible to perform a successful treatment [20].

The local HT is applied to tumors which may be directly accessed with an applicator. Depending on a placement of neoplasm, different applicator types have

been developed:

- superficial, for tumors resident on or just beneath skin. These devices, mostly operating at microwave frequencies include different kinds of waveguides [38], horn or microstrip antennas [30] and monopoles or dipoles [11]

- intracavitary, for tumors accessible through natural body cavities, which include in most cases microwave applicators [53, 12, 80]. Capacitive heating [81] and LCF techniques are also being used.

- interstitial, which are invasively placed in malignant growth. These devices incorporate capacitive coupling [72] or LCF [50] or microwave [9, 54] techniques.

The possibility of a cancer treatment with the local HT depends on a tumor placement and its volume. The advantage of this method is that the heat is delivered directly to malignant cells, which allows for obtaining higher temperatures in the area. Also a computer simulation is simplified in the case of the local HT compared to the regional one, as a high power levels are usually concentrated in one or two tissue types.

1.1.2   Brachytherapy

Brachytherapy (BT) is a type of radiation therapy in which materials are placed in direct contact with the tissue being treated. This type of therapy is applicable for those tumors, which might be directly accessed with interstitial or intracavitary brachytherapy applicators.

The BT for the cervical malignancies is usually carried out by means of a commonly used and commercially available cervical Fletcher–Suit Applicator (FSA) for Selectron[1] devices (Fig. 1.2a). This applicator consists of three subunits designed to accept radioactive Cs-137 pellets. When the applicator is assembled and placed in the desired treatment position (Fig. 1.2b) the Cs-137 sources are moved into their planned place according to the treatment plan. The source placement and their removal is accomplished with the use of compressed air. The irradiation lasts for about 10 hours. This therapy is reported to give an excellent results for small size tumors – for more advanced cases its efficiency decreases [6, 29].

1.1.3   Thermoradiotherapy in carcinoma of the cervix

The brachytherapy is combined with the regional [57, 23, 25] or local HT [62, 63, 80, 22, 81, 73] with the use of microwave or radio frequencies and intracavitary

---

[1]Nucletron Engineering BV., The Netherlands.

(a)   (b)
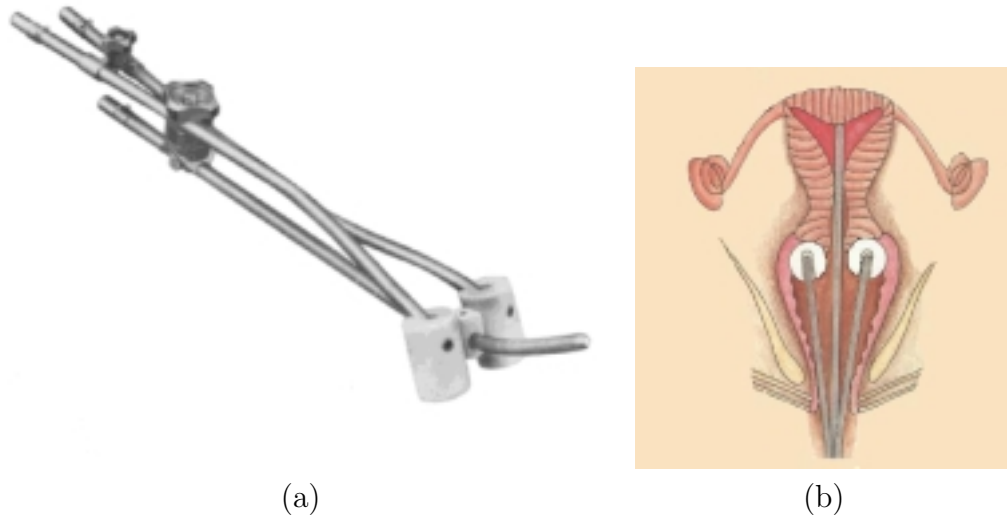
Figure 1.2: *View of a Fletcher–Suit applicator (a) and its position in the uterine cervix (b). After [37]*

[80, 15, 22, 81] or interstitial applicators [71, 13, 73]. The outcome of in vitro studies [47] as well as animal studies [39] and clinical trials [40] indicates that the synergy of these two methods may significantly improve treatment results [46, 41]. The European Society for Hyperthermic Oncology (ESHO) has performed a multi-center randomized trial, which is referred to as the ESHO protocol 3-85 [41]. The protocol indicates that radiation should be given in 3 fractions with four days' intervals in between and that the heat treatment should be applied after each of the radiation fraction within 30 minutes and should aim for a minimal tumor treatment temperature 43°C in 60 min.

1.1.4   The state of the art

The advantage of regional heating in combination with local irradiation is that those two treatments may directly follow each other without additional patient's discomfort nor long time interval. Unfortunately, as mentioned in section 1.1.1.2, the regional HT lacks the possibility of precise focusing of the power in a desired region and consequently the minimal treatment temperature of 43°C may be hard to obtain. Local HT solves the problem but the use of different applicators for the two treatments would prolong the time intervals between them, complicate the procedure and cause additional trauma to the patient (a brachytherapy applicator has to be removed and then a HT applicator has to be installed). For the case of interstitial HT (which is anyway an invasive method), the systems that use brachytherapy catheters for HT applicators have been developed [62, 9, 73]. For intracavitary HT,
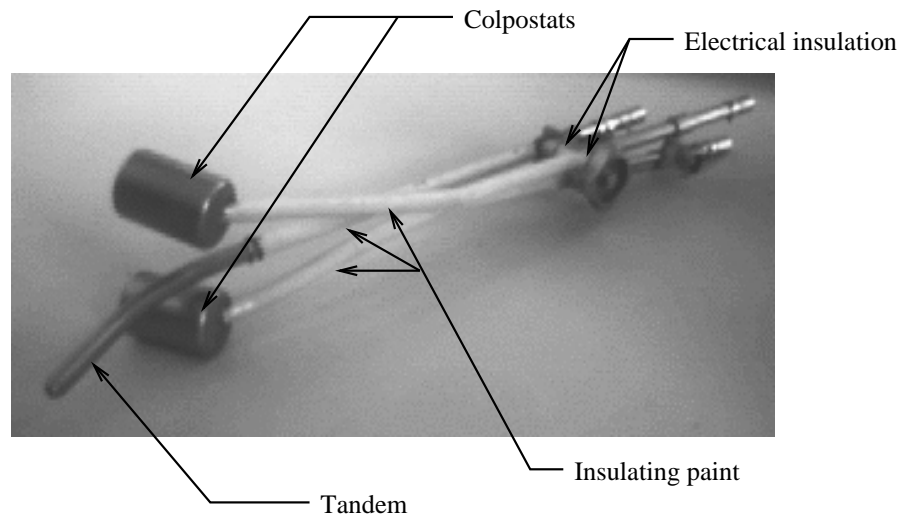
Figure 1.3: *Modified selectron compatible Fletcher-Suit cervical applicator. The colpostats are both 2 cm in diameter and 3 cm in length. The tandem is 0.6 cm in diameter and curved by 30 degrees. The tubes supporting the colpostats and the proximal part of the tandem are covered by insulating paint (white) in order to prevent health tissues from undesired heating. Each of the subunits are electrically insulated. The relative position of the colpostats and tandem depend on a patient. The thin metal foil, working as a ground electrode is additionally placed around a patient's lower abdomen*

however, only one case has been described in literature by Zimmermann *et. al.* in [81]. The system consists of a specially designed intracavitary "RF gamma applicator" and additional rectum and bladder applicators. The applicator induces heat using capacitively coupled technique and also is a source of gamma radiation. The system described in that report, however, requires rather complex instruments with the need for three electrodes inserted into the bladder, rectum and vagina.

1.1.4.1   Evaluation of the Fletcher–Suit applicator as a hyperthermia source
Another approach of incorporating standard brachytherapy intracavitary Fletcher-Suit applicator (FSA) as a hyperthermia source was proposed by professor Z. Petrovich from the University of Southern California. The advantage of using the FSA is that HT and brachytherapy may be delivered concurrently using the intracavitary device which has gained widespread acceptance. On the other hand, however, the applicator is of a specified shape and the major difficulty is to adopt the FSA as an electromagnetic source in order to obtain the best possible power and temperature distributions.

The FSA may not be used as an antenna at microwave or RF frequencies, because

of its construction, which has to be sustained for the brachytherapy treatments. The simplest method to solve the problem is to lower the frequency and use the applicator as a local current field source with electrodes which make a galvanic contact with tissue. The practical lower limit of the frequency to be used is 100 kHz, below which nerve and muscle fibers may be depolarized. The operating frequency was set to 500 kHz, at which the applicator capacitance is low and polarization mechanisms in tissue do not occur. In order to suit the FSA to work as source of an electric field some minor modifications were required (Fig. 1.3): (1) an electrical separation of the three subunits in order to function as three separate electrodes (2) an electrical insulation of these parts of the applicator, where heating is not desirable.

1.2   Scope, goals and claims of this work

The preceding section has shown the background and the application of the hyperthermia used in connection with the brachytherapy and has outlined the new approach, which has been proposed by clinicians and involves the application of a standard brachytherapy intracavitary Fletcher-Suit applicator as a hyperthermia source. Since the FSA has not been designed to be used as an electric field source, the main goal of this thesis is to analyze the possibility of effective heating of malignant tissue with the FSA and to undertake appropriate steps in order to make the hyperthermia treatments possible.

This thesis makes the following claims:

- **Effective heating of malignant cells located in different parts of the uterus is possible using the arms of the standard brachytherapy applicator as electrodes of low–frequency hyperthermia system.**

- **Novel numerical and visualization techniques enable one to carry out treatment planning within minutes while the patient awaits brachytherapy after the Fletcher–Suit applicator has been placed in a body.**

In order to prove the validity of these claims it is necessary to:

- define an electromagnetic and thermal problems;

- select an appropriate numerical method for solving the resulting boundary value problems;

- implement appropriate software tools, which would simulate the power and temperature distributions in a patient undergoing hyperthermia treatment and which would perform appropriate visualization of the obtained results;

- test the computational efficiency of the implemented software;

- demonstrate, via a number of numerical tests that, if properly excited, FSA performs adequately as a source for low–frequency hyperthermia allowing one to achieve elevated temperature in selected regions of the cervix;

- design a system for appropriate excitation of the FSA, which would also meet the medical requirements;

- verify the software and the device performing a number of phantom experiments;

- perform a number of simulations to find out, the distributions of temperature that van be obtained with the developed system;

Additionally, in order to familiarize the medical personnel with the capabilities and the limitations of the low–frequency hyperthermia system in treatment of the cervical malignancies, clinical trials have to be initiated.

The ultimate goal of this work, reaching however far beyond the scope of this thesis, is a complete system for treatment cervical malignancies with the low–frequency hyperthermia in connection with brachytherapy. At this point one may outline the main features of an ideal low–frequency hyperthermia system:

- Because a tumor can be positioned in different places, a system should have possibility of focusing the power in a specified volume.

- In order to control the focusing of heat, it would be desirable to have a method of measuring temperature in a heated volume.

- As a blood perfusion rate can change a temperature distribution, a method of its measuring would much help in optimization of excitation parameters.

In such a system it would be very easy to automate the treatment by using the temperature data as feedback. It must be clear, however, that with the current state of technology it is not possible to realize all the features of an ideal system because of the technical limitations (e.g. there is no way to measure the changes of blood perfusion rate during the treatment) or because of the ethical issues. Especially difficult are non–invasive temperature measurements in deep regions of the body during treatment. Invasive temperature measurements e.g. by means of temperature probes inserted in tumor cause trauma to the patients and are used reluctantly by clinicists. Therefore a number of experiments with phantoms were performed in order to verify the developed system and software (Chapter 7).

As stated above, the thesis makes two claims. The first claim is self-explanatory. In order to be of any practical use a hyperthermia system has to be able to elevate the temperature in the regions affected by a tumor. One has to demonstrate that this is indeed possible using the standard FSA rather then a separate set of electrodes.

The second claim of the thesis requires additional explanation. It is essential that the treatment planning software uses fast numerical techniques. The reason is that the problem is three dimensional, an electric boundary value problem has to be solved many times, followed by a solution of a thermal problem and additional grid conversions are necessary in some cases. Moreover, all this simulation has to be completed after the applicator is placed in a patient (in order to make an X-ray pictures of an applicator position) and before treatment initialization, in order to set appropriate excitation of arms of the applicator. The speed of the solver (treatment planning) reduces the patients trauma and this is the issue which is of the utmost importance from the clinical viewpoint.

1.3   Chapter outline

The outline of the thesis is as follows. The next chapter defines the problem in mathematical and physical terms and discusses the possible methods of its solution. Firstly, the electromagnetic formulations leading to a quasi–static approach of the solution are specified, which are followed by temperature formulations required for the solution of a bio–heat transfer equation. Secondly, the methods of solving the boundary value problems and discretization methods are discussed. The finite element approach with the multigrid iteration scheme based on a tetrahedral grid, which seemed to be the most optimal, is presented in details.

Chapter 3 describes, step by step, a treatment planning system, starting from the data input and grid generation, then describing the implementation of the numerical methods for the solution of the power and temperature distributions and ending on the visualization methods.

The numerical experiments, which compare different numerical approaches and find the most optimal solution configuration are presented in Chapter 4.

Chapter 5 gives guidelines for the future use of the treatment planning where a number of simulations for different patient geometries and different excitations of the FSA are analyzed.

Chapter 6 contains a description of devices used for the excitation of the FSA. First, the system prototype *HT–1*, which enabled only simple excitation modes is described. The second section of this chapter presents a new *HT-2* hyperthermia system, which has been designed according to the author's specifications.

The results of the experiments with solid and liquid phantoms, with the use of the new *HT-2* system, are given in Chapter 7. These experiments are very important before the system and the software use in the first clinical treatments, whose description can be found in Chapter 8. The final summary and conclusions are given in Chapter 9.

Appendices support some additional information. Appendix A presents an analytical solution of a bio–heat transfer equation in cylindrical coordinates, which is used in approximation of the blood perfusion rate in Section 2.1.2. Appendix B shows details of algorithms used for mesh conversions (from irregular tetrahedral grid to regular rectangular grid) and for the generation of the surface model of the applicator. The final, Appendix C, reveals the calibration procedure of the *HT-2* hyperthermia device.

Chapter 2

Solution of a boundary value problem

The problem under investigation is to find power and temperature distribution in a vicinity of the applicator, given the excitation parameters and estimated blood perfusion rate in a patient's body. In this chapter we shall define the problem in mathematical and physical terms (section 2.1) and discuss methods for its solution (section 2.2). The method selected is fully described at the end of this chapter.

2.1 Problem definition

The relations, which govern the pattern of the absorbed power density when the applicator is excited during the hyperthermia treatment are described in section 2.1.1. The issues pertaining to the modeling of the thermal problem are discussed in section 2.1.2.

2.1.1 Modeling of SAR distribution

The quantity known as the Specific Absorption Rate (SAR) is frequently used in bio–electromagnetic simulations in order to visualize the possible increase of tissue temperature. SAR expresses the amount of power absorbed by a mass volume of tissue and can be written as:

$$SAR = \frac{P}{\rho} \left[\frac{W}{kg} \right] \tag{2.1}$$

where $P \left[\frac{W}{m^3} \right]$ is absorbed power density and $\rho \left[\frac{kg}{m^3} \right]$ is tissue mass density.

2.1.1.1   Electromagnetic formulations

The relation between the vector of electrical field intensity and the absorbed power density is expressed as:

$$P = \frac{\sigma}{2}|\vec{E}|^2 \tag{2.2}$$

where σ represents the conductivity of a medium. The electromagnetic relations are governed by Maxwell's equations which, in frequency domain and in source-free medium, can be written as:

$$\nabla \cdot \vec{D} = 0 \tag{2.3}$$

$$\nabla \cdot \vec{B} = 0 \tag{2.4}$$

$$\nabla \times \vec{E} = -j\omega\mu\vec{H} \tag{2.5}$$

$$\nabla \times \vec{H} = j\omega\epsilon\vec{E} + \vec{J_c} \tag{2.6}$$

The material relationships are as follows:

$$\vec{B} = \mu\vec{H} \tag{2.7}$$

$$\vec{D} = \epsilon\vec{E} \tag{2.8}$$

$$\vec{J} = \sigma\vec{E} \tag{2.9}$$

where $\vec{E}$ and $\vec{H}$ represent electric and magnetic field intensities, $\vec{D}$ and $\vec{B}$ electric and magnetic flux densities, $\vec{J_c}$ is conduction current density, ω is the angular frequency and μ and ϵ represent premeabilty and permittivity, respectively. For the case of low frequency, where wavelength substantially exceeds the size of a domain, Maxwell's equations may be reduced to a quasi–static case. In this case we may write equation (2.5) as:

$$\nabla \times \vec{E} = 0 \tag{2.10}$$

and express $\vec{E}$ in terms of the electric potential:

$$\vec{E} = -\nabla V \tag{2.11}$$

Taking the divergence of equation (2.6) and applying equation (2.3) we get the continuity equation in a source-less medium which expresses the conservation of electric charge:

$$\nabla \vec{J} = 0 \tag{2.12}$$

Substituting $\vec{J}$ with the equation (2.9) and applying (2.11) we get Laplace's equation:

$$\nabla \cdot \sigma\nabla V = 0 \tag{2.13}$$

The power distribution can be calculated from the solution of (2.13) by assuming appropriate boundary conditions (BC) and applying equations (2.11) and (2.2).
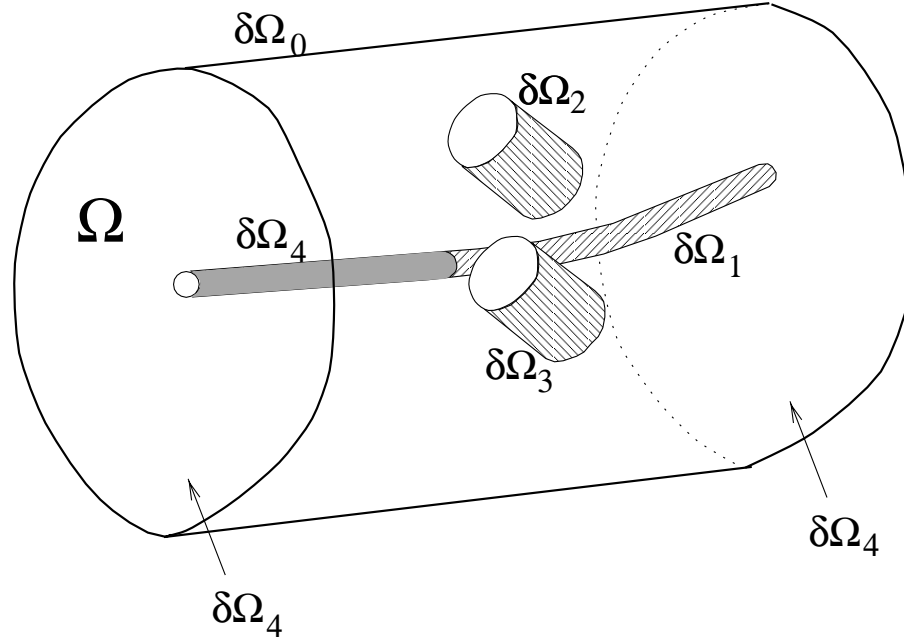
Figure 2.1: *The description of the domain. Boundary $\delta\Omega_0$ represent a thin metal foil around a patient's lower abdomen. Boundaries $\delta\Omega_1$ to $\delta\Omega_3$ represent applicator's electrodes where voltage is applied and $\delta\Omega_4$ represent Neumann boundary conditions*

2.1.1.2 Boundary conditions

The boundary value problem is shown in Figure 2.1. The 500 kHz voltage, applied to the applicator's electrodes, is represented as boundaries $\delta\Omega_1$, $\delta\Omega_2$ and $\delta\Omega_3$ in the figure. The external electrode, which is always grounded, is referred to as $\delta\Omega_0$. The electrodes represent the Dirichlet boundary conditions, while the insulated part of the tandem and the open ends of the domain are mapped as the Neumann BC ($\delta\Omega_4$). Having specified the boundary conditions we can then state our problem as:

$$\begin{cases} \nabla \cdot (\sigma \nabla V) = 0 & \text{in } \Omega \\ V = 0 & \text{on } \delta\Omega_0 \\ V = V_i & \text{on } \delta\Omega_i, \quad i = 1, 2, 3 \\ \frac{\partial V}{\partial n} = 0 & \text{on } \delta\Omega_4 \end{cases} \tag{2.14}$$

where n is a vector normal to the $\delta\Omega_4$ surface.

The applicator's construction (see Figs 1.3 and 2.1) implies three independent classes of solution. These classes correspond to three excitation modes – 001 (left[1] electrode is excited, while others are grounded), 010 (central electrode is excited, while others are grounded) and 100 (right electrode is excited, while others are grounded). The outer electrode is always grounded. Knowing the solution for the

---

[1]left and right refers to a patient's right and left sides

three basic modes it is possible to find $\vec{E}$ – field distribution for arbitrary excitation using a superposition of the three basic mode solutions $\vec{E}_i$:

$$\vec{E}_{tot} = \sum_i^3 A_i \vec{E}_i e^{-j\theta_i} \tag{2.15}$$

where A_i is the amplitude and θ_i is the phase–shift of the i–th applicator's electrode.

2.1.2   Modeling of temperature distribution

The modeling of temperature distribution is usually the second step in any hyperthermia treatment planning. Having specified the problem for the power density deposited in tissue, we proceed now with thermal formulations.

2.1.2.1   *Temperature formulations*

Thermal behavior of living tissue was formulated by Pennes in 1948 [45]. This formulation expresses the balance of thermal energy in time and space and is also known as a bio–heat transfer equation:

$$\rho_t c_t \frac{\partial T}{\partial t} = \nabla \cdot (k \nabla T) - c_b W (T - T_b) + P \tag{2.16}$$

where k is a thermal conductivity, ρ_t tissue mass density, c_b and c_t are blood and tissue specific heat, W is a volumetric perfusion rate in $[kg\ m^{-3}\ s^{-1}]$, T_b is blood temperature and P is the power density delivered to tissue by external means. In our case P is defined in terms of the absorbed, electric field power radiation as specified in equation (2.2).

The hyperthermia treatment lasts for about 1 hour, which is long enough to assume a steady state temperature distribution in further investigations. A simple analysis, whose results are shown in Figure 2.2 proves, that even after 10 minutes after the power switch off, temperature at the applicator surface gains almost a steady state level (for $k = 0.542$, which is typical for muscle tissue). Thus, in order to simplify the evaluation procedure, the time derivative in (2.16) is assumed to be zero in further investigations and the equation expressing the steady state of the temperature distribution becomes:

$$-\nabla \cdot (k \nabla T) + c_b W (T - T_b) = P. \tag{2.17}$$

In order to solve this equation for T we need:

- Power density, P, which may be found from (2.2),

- Tissue thermal conductivity k and a blood specific heat c_b (parameters known from literature [21]),

a)   b)
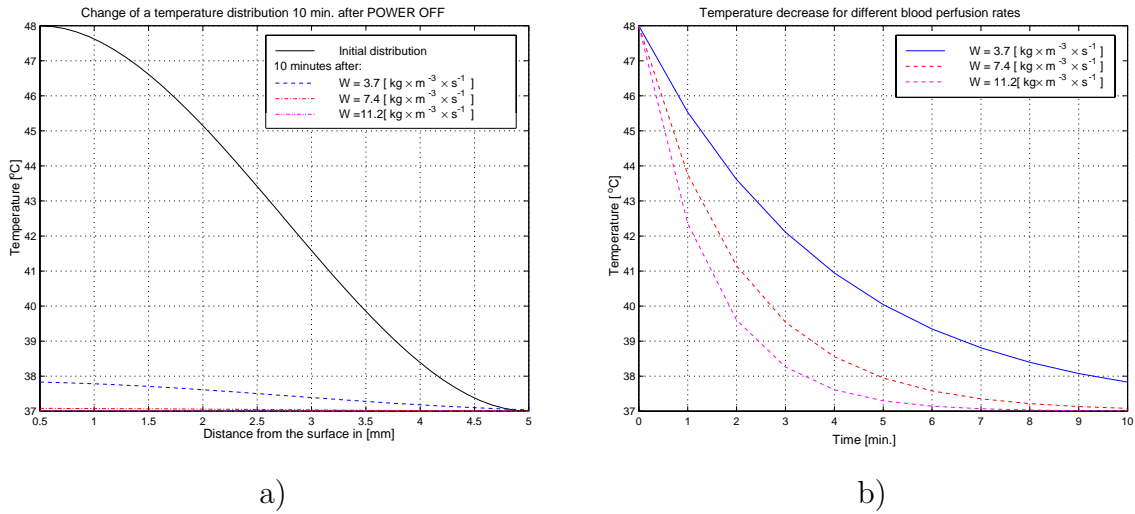
Figure 2.2: *Time required to obtain the steady state of a temperature distribution.*
a) Theoretical initial temperature distribution and its change 10 minutes after the
power switch off. b) The temperature decrease at the surface of the applicator in the
period of 10 minutes after the power was switched off. The plot is a result of an
analytical solution of equation 2.16, as derived in appendix A.

- Volumetric blood perfusion rate W (see section 2.1.2.2),

- Boundary conditions (see section 2.1.2.3).

2.1.2.2   Blood perfusion rate

A blood perfusion rate in muscle tissue is specified in the following limits [21]:

	$\left[\frac{kg}{m^3 \cdot s}\right]$	$\left[\frac{ml}{100g \cdot min}\right]$
Muscle	$0.37 - 3.7$	$2 - 20$
Active muscle	18.94	167
Uterus malignancies	$1.93 - 7.6$	$17 - 67$

One of those values has to be assumed for the simulation, as there is no an ac-
curate method of measuring the blood perfusion rate on–line during a treatment.
In simulations, presented in Chapter 5, the highest blood perfusion rate for uterus
malignancies has been assumed, as the worst–case situation. Decrease of a blood
perfusion rate enlarges the heated volume (this gives a better therapeutic issue),
but also rises the maximum temperature. Thus, such an approach can be justified
if the highest temperature point can be controlled during treatment.

A simple approach of approximation a blood perfusion rate, based on tempera-
ture measurements, has also been analyzed. This, however, required an additional
assumption that a temperature is measured in region of low gradients, so that the

component associated with thermal conductivity k in equation (2.16) is insignificant. Such an approach gives qualitative information about a blood perfusion rate, which can be found in a following manner. After a steady state temperature is obtained, the thermal equilibrium is described by (2.17). The moment the power is switched off, the equation transforms into transient state and, if the above assumption is justified, takes the form:

$$\rho_t c_t \frac{\partial T_w}{\partial t} = -c_b W T_w \tag{2.18}$$

where $T_w = T - T_b$. The solution of this equation can be sought in the form:

$$T_w = T_{w_0} \cdot e^{-xt} \tag{2.19}$$

where T_{w_0} is equal to temperature rise above T_b and is equal T_w for $t = 0$. The derivative takes the form:

$$\frac{\partial T_w}{\partial t} = -T_{w_0} x e^{-xt} \tag{2.20}$$

Substituting (2.20) and (2.19) into (2.18) one can find that:

$$x = \frac{c_b W}{c_t \rho_t} \tag{2.21}$$

and rewrite (2.19) as:

$$T_w = T_{w_0} \cdot e^{-\frac{c_b W}{c_t \rho_t} \cdot t} \tag{2.22}$$

Finally, rearranging the above equation, we get the solution for the volumetric blood perfusion rate:

$$W = \frac{c_t \rho_t}{c_b \cdot t} \ln \frac{T_{w_0}}{T_w} \tag{2.23}$$

Thus, switching the power off during treatment, when a steady state temperature has been obtained may serve as an estimation of a blood perfusion rate. An example of application of this method is shown in Figure 2.3a. Solid lines in the plot represent temperature measurements obtained during a clinical trial (as described in Figure 8.1). Based on this data t, T_{w_0} and T_w values have been found and W has been calculated from equation (2.23), which resulted in $W = 5.66 \left[\frac{kg}{m^3 s}\right]$ and $W = 4.06 \left[\frac{kg}{m^3 s}\right]$ respectively, which are reasonable values. Dashed lines are a result of substituting calculated W into (2.22). Note, that for the case when the temperature was measured at the tandem surface, the calculated curve does not fit the measured one. The main reason is probably a metal, the tandem is made off, which
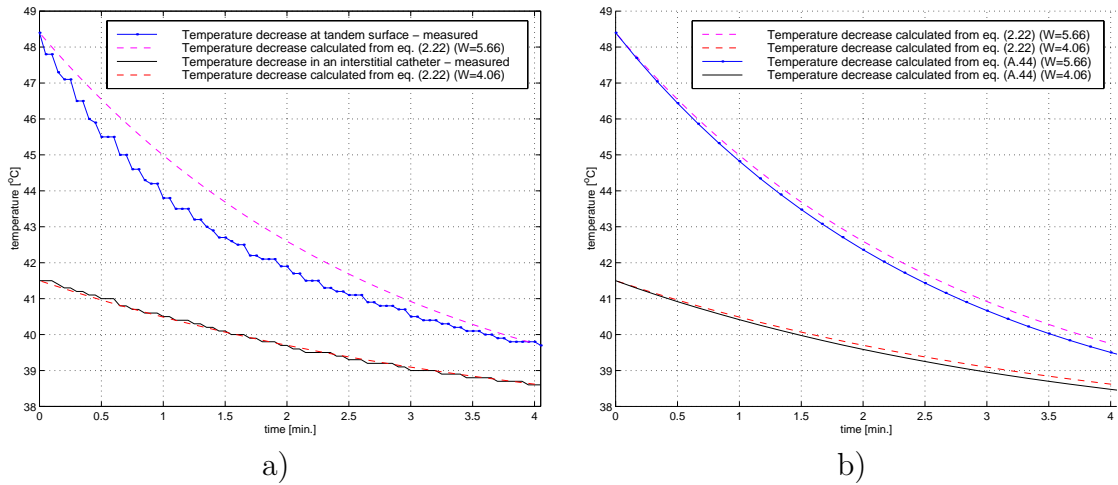
Figure 2.3: *a) An example of application of equation (2.23). Solid lines represent temperature decrease measured in a real treatment after the power was switched off (as shown in Figure 8.1). Based on this measurements a blood perfusion rate has been calculated for both curves from equation (2.23). Dashed lines represent a temperature decrease calculated from equation (2.22). More details in the text. b) Temperature distribution obtained from equation (A.44) with $T_M = 48°C$ and $r_1 = 6mm$ against the one obtained from (2.23). Those two approaches differ by expression $-\nabla \cdot (k\nabla T)$.*

transfers the heat away from tissue. Also the assumption of low gradients at the tandem surface may not be justified. Looking at the black curve, the result of the in–tissue temperature measurement (placed about 15mm away from the tandem) one can see a good agreement with the equation (2.22).

There is also a possibility to judge a blood perfusion rate by solving a transient bio-heat transfer equation, but an initial temperature distribution in the vicinity of the tandem (which is unknown *a'priori*) has to be assumed. Such an analysis (which also assumes that the tandem as an ideal cylindrical source) is performed in Appendix A. As a result, an equation for temperature distribution as a function of time and distance from the applicator is found for a specified initial temperature distribution. Figure 2.3b presents the comparison of this approach against the one described above. It might be seen, that the influence of the component associated with the thermal conductivity k ($k = 0.542$ for muscle tissue) is indeed insignificant for the presented case.

2.1.2.3   Boundary conditions

Boundary conditions are specified for the domain schematically shown in Figure 2.1. Assuming the constant basic body temperature the boundary $\delta\Omega_0$ is specified as the Dirichlet BC, where $T = 37°C$ on $\delta\Omega_0$. The remaining boundaries are assumed to

have the temperature of adjacent tissue and thus the boundary condition is set as the Neumann type.

2.2   Numerical method for solving boundary value problem

A solution of the defined problem is not possible using an analytical approach, because of its complicated three dimensional domain. It is thus necessary to select a numerical method for a solution of the problem. To perform this, one would first specify requirements for the method. The method should meet the following requirements:

- should be three dimensional,

- should have a possibility of definition of complicated boundaries,

- a possibility of definition an inhomogeneous medium in order to represent different internal organs,

- ideally, should be characterized by an optimal computational cost $\mathcal{O}(N)$, i.e. the solution time should be proportional to the number of unknowns,

- should be fast, in order to perform simulations after the applicator is placed in a patient and before treatment initialization.

Only a few methods exist, which can cope with complex shapes and inhomogeneous media. In order to select the one which would fit our problem in the best way, one has to start with the overview of these methods. Some of them have already been used in the electromagnetic and thermal modelings in human tissues.

In last decades in electromagnetics the finite difference time–domain method (FDTD) has gained much attention. The success of this method can be explained by simplicity of the algorithm and low computational cost. The computational effort grows linearly with the increasing number of unknowns. In general, the FDTD is described as a direct solution method of time–domain Maxwell's equations by implementation of a marching-in-time procedure, which stimulates the actual propagating electromagnetic waves by sampled data numerical analogs, propagating in computer data space [67].

For low–frequency applications FDTD is inadequate as the time step becomes very short compared to the period of the wave and thus the frequency domain version of Maxwell's equations is preferred. Both FDTD and finite difference formulations start from the full set of Maxwell's equations and yield the full–wave solution. This

is too time consuming. At low frequencies, applications a quasi–static approach is more appropriate, as it reduces the number of unknowns.

The quasi–static approach has been proposed by de Bree [10], who calculated SAR distribution from the electrical potential field. The method was applied to the calculation of the energy deposition in inhomogeneous tissue during HT treatment. In this approach the rectangular grid is used and the calculations are performed by a numerical solution of Poisson equation by an introduction of an iteration function an by marching in pseudo–time steps. Additional voltage and SAR correction is performed by analytical solution in the vicinity of electrodes. The method requires about 200 iterations for a grid of $60 \times 60 \times 60$ nodes in order to minimize the error in the potential to below 5%.

The methods described above use rectangular grids which do not conform well to complicated shapes. Unlike those ones, the finite element method is very powerful in application to complex geometries. The method divides the computational region into a number of finite elements, which in general, can be of different shape. This discretization, along with the boundary conditions and interpolation functions defined for each element, leads to a system of equations (to a sparse matrix problem), which is solved by an iterative scheme. The final solution is found at nodal points of the finite element mesh, but can be interpolated to an arbitrary point using the interpolation functions. In most 3D cases the method uses tetrahedral meshes, which easily conform to complicated shapes of a domain. At the beginning of this decade FEM has mainly been used for the simulation of temperature distribution by the solution of a bio-heat transfer equation (2.16) [7, 31]. Since recently some problems associated with vector parasites (spurious modes of the solution) in finite element solution of Maxwell equations have been solved [44], the method has also been applied for the simulation of the SAR distribution (full-wave simulation) in human body undergoing hyperthermia treatment [43, 8]. Nevertheless, some problems with convergence for large number of elements have been reported [43]. The convergence of the method has been significantly improved by an application of multigrid iteration schemes. This has been reported by Beck *et al.* [1] who use so called edge elements and adaptive refinement for domain discretization.

The multigrid method is much like the finite difference or finite elements methods, concerning the discretization procedure which results in a sparse matrix problem. Unlike those, however, the method operates on different grid resolutions during the iteration procedure. Moreover, the meshes are both refined and coarsened during the solution process. This modification was introduced as a result of the analysis of the convergence properties of iterative solvers.

In order to select the most optimal method for the problem solution, one can first consider advantages and disadvantages of different domain discretization, as specified in Table 2.1. A simple comparison of those two discretization can be found

Table 2.1: *Advantages and disadvantages of the regular rectangular and irregular triangular grids*

Regular rectangular (cubical) grid		Irregular triangular (tetrahedral) grid	
Advantages	Disadvantages	Advantages	Disadvantages
Fast generation	Stair–case approximation of a domain shape	Much better shape approximation	Grid generation, although automatic, requires additional time
Irrelevant memory usage for grid data	Requires large number of nodes for large domains when high resolution is needed	Much smaller number of nodes for large domains and high resolutions	Grid structure requires large memory resources

in Figure 2.4. It might be seen, that the regular gridding results in poor approxima-
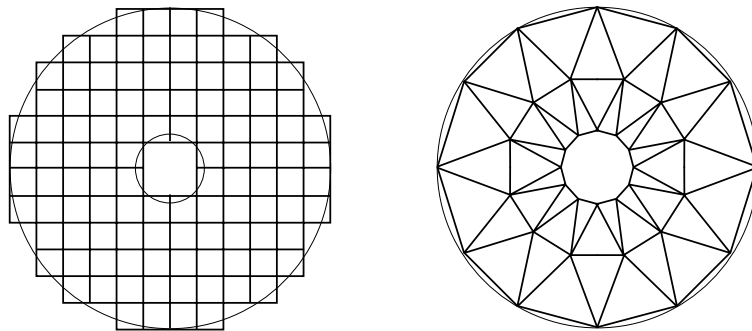
Figure 2.4: *Comparison of two different discretization schemes. Regular rectangular grid on the left and irregular triangular grid (structured grid) on the right for the same domain. Note the quality of the approximation of boundaries. Although the first grid contains 136 nodes and the second one only 36 of them, the grid with triangular elements much better fits to curved boundaries. The latter one, however, uses more memory for grid structure storage (each element is numbered and has associated nodes, which in turn have associated spatial coordinates).*

tion of curved boundaries even for relatively large number of nodes. Nonetheless, the memory storage for the irregular meshing is larger, as each element is numbered

and has associated nodes, which in turn have associated spatial coordinates. In a regular grid only node indices and a size of a cell are needed. The size of the linear algebra problem, however, is determined by the number of nodes and thus it is profitable to choose a discretization scheme which results in smaller number of nodes, even at the cost of some additional memory.

The use of quasi–static approximation suppresses the need for the full–wave analysis, such as finite difference or finite volume time–domain methods and enables one to operate on potential fields. Thus, for the problem at hand, the finite element approach can be successfully applied for the solution of both, the Laplace's and the bio-heat transfer equations. Also the finite element discretization with irregular tetrahedral grid may serve its purpose. Additional application of adaptive multigrid iteration scheme, as will be shown at the end of this chapter, can improve the effectiveness of the solution.

2.2.1   Standard finite element method

In this section a general description of the finite element method is given, based on the formulations presented in books [56, 28]. The finite element method (FEM) is a numerical approach for solving differential equations of different kind in the domain Ω with specified boundary conditions. In general, one can write this problem as:

$$\mathcal{L}\boldsymbol{\phi} = \boldsymbol{f} \tag{2.24}$$

where $\mathcal{L}$ represent the differential operator, $\boldsymbol{\phi}$ the searched quantity and f a function defining the source.

The FEM belongs to the family of variational methods in which the computational space is divided into subdomains, which are called finite elements. The dimensions of those elements are much smaller than the dimension of the whole domain, thus simple functions can be used to interpolate the solution within elements. Usually polynomials of the first or the second order are used and are called the expansion or basis functions. Elements, the most frequently used, include triangles in a 2D and tetrahedra in a 3D problems. Such elements can easily be fitted to complex geometries. The solution in the FEM is usually constructed in terms of the unknown function ϕ specified at nodes associated with the elements. For example, triangular elements contain 3 nodes located at vertices and tetrahedra contain 4 nodes located in each corner (the number of nodes in an element depends on the order of the interpolation function used, as it will be explained later in the text). Each node in an element has associated space coordinates and also a local and a global number. Local numbering indicates the position of the node within an element and the global number is related to the location of the node within the whole domain.
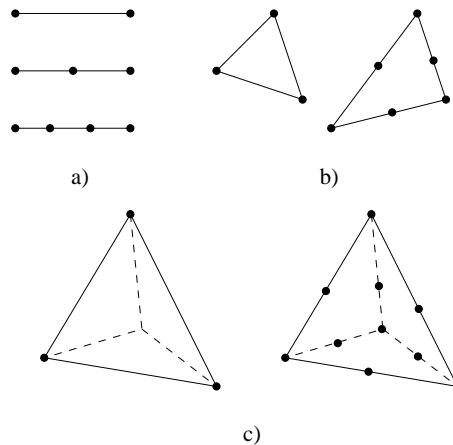
Figure 2.5: *Examples of finite elements for 1, 2 and 3 dimensions, which are respectively defined as lines (a), triangles (b) and tetrahedra (c). Number of nodes for each element depends on the order of an interpolation function used.*

The discretization procedure can be treated as a preprocessing to the finite element method and can be performed separately.

As mentioned before, the basis functions used to interpolate the solution within an element, in most cases, include polynomials of the first or the second order. The order of the basis functions influences the number of nodes within an element due to the number of coefficients associated with the function. In the simplest one dimensional case elements are defined as lines. Thus, one gets 2 nodes for the first order polynomial and 3 nodes for the 3rd order polynomial and consequently more for the higher orders. (Fig. 2.5a). Analogously, triangular elements associated with the quadratic interpolation functions contain 6 nodes (3 placed in vertices and 3 on triangle edges) and tetrahedra contain 10 nodes. The elements related to the first order polynomials are called linear elements, while the ones related to the quadratic interpolation functions are called the quadratic elements. As an example, let us specify the expansion functions for the linear and quadratic two–dimensional triangular elements. For the first case we get:

$$\phi^e(x, y) = a + bx + cy \qquad (2.25)$$

and, respectively, for the quadratic case:

$$\phi^e(x, y) = a + bx + cy + dx^2 + exy + fy^2 \qquad (2.26)$$

where ϕ^e is a function value at an arbitrary point of coordinates (x, y) within the element, superscript e denotes that the function is specified within an element and a, b, c, d, e and f are coefficients. In practice, instead of arbitrary coefficients, one

can use the the nodal values of the sought function ϕ. As an example let us specify the interpolation function (2.25) at three nodal values:

$$
\begin{bmatrix} \phi_1^e \\ \phi_2^e \\ \phi_3^e \end{bmatrix} = \begin{bmatrix} 1 & x_1 & y_1 \\ 1 & x_2 & y_2 \\ 1 & x_3 & y_3 \end{bmatrix} \begin{bmatrix} a \\ b \\ c \end{bmatrix}
\tag{2.27}
$$

Taking the inverse transformation of the matrix we can obtain the expressions for the coefficients:

$$
\begin{bmatrix} a \\ b \\ c \end{bmatrix} = \begin{bmatrix} 1 & x_1 & y_1 \\ 1 & x_2 & y_2 \\ 1 & x_3 & y_3 \end{bmatrix}^{-1} \begin{bmatrix} \phi_1^e \\ \phi_2^e \\ \phi_3^e \end{bmatrix}
\tag{2.28}
$$

which when substituted into the equation (2.25) results in:

$$
\phi^e = \sum_{i=3}^{3} N_i(x, y) \phi_i^e
\tag{2.29}
$$

In this expression, the interpolation function consists of three components N_i which are sometimes called shape functions; ϕ_i^e is a coefficient equal to the solution at the $i-th$ node. Analogously, for the quadratic elements we get:

$$
\phi^e = \sum_{i=1}^{6} N_i(x, y) \phi_i^e
\tag{2.30}
$$

From the above equations it is evident that although quadratic interpolation is more accurate, it results in much larger equation systems (twice as large for triangular gridding in 2D and 2.5 as large for tetrahedral gridding in 3D).

In practice, every element is normalized before calculations are performed. Thus, the shape functions are explicitly known for every element type. For example, the linear shape functions for a triangle in 2D, as in Figure 2.6, are specified as:

$$
\begin{aligned}
N_1(x, y) &= 1 - x - y \tag{2.31} \\
N_2(x, y) &= x \tag{2.32} \\
N_3(x, y) &= y \tag{2.33}
\end{aligned}
$$

From the equation (2.29) it can be inferred, that, as ϕ_i^e is defined at the i-th node, the shape function N_i^e for that node equals unity, while for the other nodes it becomes 0. The shape function, defined within a single element, becomes zero outside of it as well. Thus, the solution over the entire computational domain can easily be defined as:

$$
\phi = \sum_{e=1}^{M} \sum_{j=1}^{n} N_j^e \phi_j^e
\tag{2.34}
$$
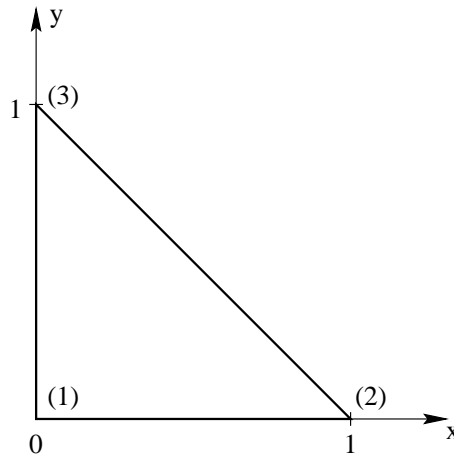
Figure 2.6: *View of the normalized triangle*

where M is the number of elements in the region and n is the number of nodes in the element. Alternatively, we can write equation (2.34) using global numbering of the nodes as:

$$\phi = \sum_{j=1}^{N} N_j^g \phi_j \qquad (2.35)$$

where N is the total number of nodes and a superscript g refers to the global numbering of the nodes. The shape functions, which are partially continuous over the entire domain, enable one to obtain the solution in an arbitrary point of the computational region, knowing only the values calculated at vertices. The quality of the solution depends on the size of the elements (smaller elements induce smaller errors) and on the order of the interpolating function.

Having discretized the domain, one can start with the definition of the system of equations. It is usually obtained by the application the variational Rayleigh–Ritz (RR) or Galerkin method to (2.24). Using the RR method, the solution is obtained by minimizing the functional:

$$W(\phi) = \frac{1}{2} \int_{\Omega} \phi \mathcal{L} \phi d\Omega - \int_{\Omega} f \phi d\Omega \qquad (2.36)$$

under the assumption, that the operator $\mathcal{L}$ is self–adjoint. The minimum of $W(\phi)$ implies that the partial derivatives of (2.36) with respect to ϕ_i equals zero. Using equation (2.35) it can be written in the following form:

$$\frac{\partial W}{\partial \phi_i} = \sum_{j=1}^{N} \phi_j \int_{\Omega} N_i^g \mathcal{L} N_j^g d\Omega - \int_{\Omega} f N_i^g d\Omega = 0 \quad i = 1, 2, 3, \ldots, N. \qquad (2.37)$$

Substituting

$$C_{ij} \;=\; \int_\Omega N_i^g \mathcal{L} N_j^g d\Omega \tag{2.38}$$

$$b_i \;=\; \int_\Omega f N_i^g d\Omega \tag{2.39}$$

into the equation (2.37), one can write the resulting set of equations in a matrix form as:

$$\boldsymbol{C}\boldsymbol{\phi} = \boldsymbol{b} \tag{2.40}$$

where $\boldsymbol{C}$ is the so–called global coefficient (or stiffness) matrix and represents coupling between the nodes i and j. Thus, as only some of the nodes are connected, the sparsity of the matrix $\boldsymbol{C}$ increases with the problem size. Additionally, if the nodes are numbered properly, the matrix is banded and its bandwidth depends on the maximum difference between the global numbers of two nodes in an element. Equation (2.40) can be solved, using any of the standard iterative approaches like conjugate gradient or Gauss-Seidler methods. Unfortunately these methods may suffer from poor convergence, especially for high resolution meshes. An alternative is to use multigrid methods, which effectively improve the convergence of the iterative solvers, as it will be seen in the next section.

2.2.2 Multigrid methods

In recent years multigrid techniques have emerged as an efficient tool for the solution of linear equation system resulting from discretization scheme such as finite element or finite difference methods [5, 77]. Their effectiveness can be even further improved by application of adaptive grid refinement of the computational domain [32]. These methods are especially valuable for high resolution meshes, i.e. when standard iterative schemes result in long solution times due to poor convergence. The approach incorporates standard iterative methods, however, in order to efficiently improve the convergence of the solution, it operates on different grid resolutions (by coarsening and refining the original mesh). To outline the method one can start with considerations concerning the error propagation and convergence of a typical iterative solver.

2.2.2.1 *Convergence of an iterative solver*

Iterative methods for solving linear system of equations are the methods, which start from an approximation of the true solution and then apply a computational cycles, which consequently improve the accuracy of the solution. The number of this cycles

depends on the required final precision. The first approximation of the solution is called an *initial guess* and the computational cycles are referred to as the *iteration* or *relaxation* procedure.

In general, the approximation of a solution after the first iteration in a basic iterative solver can be expressed as:

$$\boldsymbol{\varphi}^{(1)} = \boldsymbol{P}\boldsymbol{\varphi}^{(0)} + \boldsymbol{g} \tag{2.41}$$

where $\boldsymbol{\varphi}^{(0)}$ is an initial guess and $\boldsymbol{\varphi}^{(1)}$ is the first approximation of the solution. $\boldsymbol{P}$ represents an iteration matrix, which is constructed by some transformation of matrix $\boldsymbol{C}$; $\boldsymbol{g}$ depends on the solver type and the right side of equation (2.40). For the simplest Jacobi iteration scheme we get $\boldsymbol{P} = (\boldsymbol{I} - \boldsymbol{C})$ and $\boldsymbol{g} = \boldsymbol{b}$, where $\boldsymbol{I}$ is an identity matrix. The iteration matrix $\boldsymbol{P}$, does not change the exact solution, i.e.:

$$\boldsymbol{\phi} = \boldsymbol{P}\boldsymbol{\phi} + \boldsymbol{g} \tag{2.42}$$

where $\boldsymbol{\phi}$ denotes the exact solution. Subtracting (2.42) from (2.41) we get the error relation between the two subsequent iterations:

$$\boldsymbol{e}^{(1)} = \boldsymbol{P}\boldsymbol{e}^{(0)}. \tag{2.43}$$

Thus, the error after n iterations becomes:

$$\boldsymbol{e}^{(n)} = \boldsymbol{P}^n \boldsymbol{e}^{(0)}. \tag{2.44}$$

We can also express the equation (2.44) with the error of the initial guess $\boldsymbol{e}^{(0)}$ expanded into the set of eigenvectors of the iteration matrix:

$$\boldsymbol{e}^{(0)} = \sum_{k=1}^{N-1} c_k \boldsymbol{w_k}, \tag{2.45}$$

where c_k are the expansion coefficients and $\boldsymbol{w_k}$ are the eigenvectors of the iteration matrix with subscript k denoting the wavenumber of the Fourier mode of the error. Thus, since:

$$\boldsymbol{P}\boldsymbol{w_k} = \lambda_k(\boldsymbol{P})\boldsymbol{w_k} \tag{2.46}$$

we can write:

$$\boldsymbol{e}^{(n)} = \sum_{k=1}^{N-1} c_k \boldsymbol{P}^n \boldsymbol{w_k} = \sum_{k=1}^{N-1} c_k \lambda_k^n(\boldsymbol{P})\boldsymbol{w_k}, \tag{2.47}$$

where λ_k represents the k-th eigenvalue of $\boldsymbol{P}$. After n iterations the error associated with λ_k is reduced by a factor of λ_k^n (since in any numerically stable iteration method
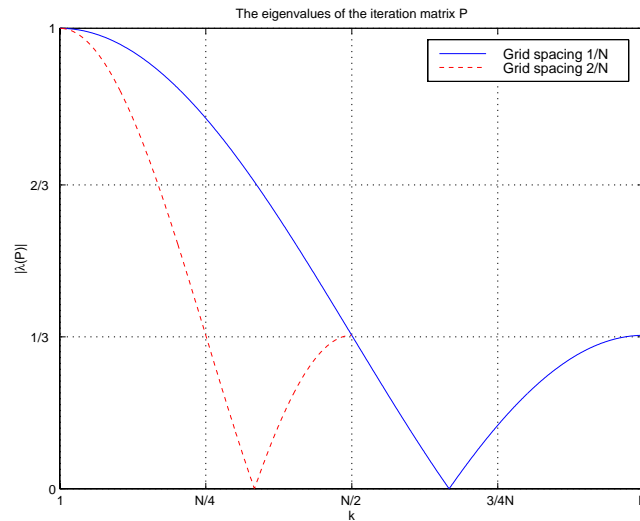
Figure 2.7: *The magnitudes of the eigenvalues of the iteration matrix* $\boldsymbol{P}$ *for the optimal value of weighting factor* ω *and for grid resolution* $1/N$ *and* $2/N$. *Note, that by increasing the grid spacing (reducing number of nodes) it is possible to decrease the magnitude of the eigenvalues associated with low* k.

the magnitudes of the eigenvalues of the iteration matrix P are less than unity). This implies that the error components associated with eigenvectors corresponding to low magnitude of λ_k converge much faster than those whose associated eigenvalues are close to unity. Therefore, the convergence factor for an iterative solver is specified as a spectral radius of the iteration matrix:

$$\rho(\boldsymbol{P}) = \max_k |\lambda_k(P)| \tag{2.48}$$

As an example, consider a weighted Jacobi iteration scheme, which is representative for all basic iterative methods, and apply to a model problem of one–dimensional finite–difference approximation of Laplace equation. Eigenvalues of the iteration matrix are specified as [5]:

$$\lambda_k(\boldsymbol{P}) = 1 - 2\omega \sin^2(\frac{k\pi}{2N}), \qquad 1 \leq k \leq N-1,\ 0 < \omega \leq 1 \tag{2.49}$$

where N denotes the number of nodes and ω is the weighting factor. The plot of the eigenvalues of the iteration matrix for optimal value of ω is presented in figure (2.7). It can readily be seen, that error components which are associated with low k (which can also be interpreted as the low oscillatory error modes) converge slowly due to the fact, that the magnitude of those eigenvalues approaches the unity. The oscillatory error components (those associated with high k), however, can efficiently be damped.

This fact is also sometimes called the *smoothing property*, as an application of such a solver smoothes the solution by eliminating high oscillatory error modes and leaving the smooth error components. The smooth error components are responsible for the poor convergence. Moreover, it can be seen from the equation (2.49) that improving the quality of the solution by grid refinement, can at most worsen the situation. Namely, if N increases (i.e. mesh becomes denser) for a fixed value of k, then λ_k approaches the unity. And the other way round, coarsening the grid can improve the convergence, as the low oscillatory modes become more oscillatory for decreasing N.

Having in mind the properties of the error in an iterative solver, we can now turn to multigrid method and see how the convergence problems can be overcome. Before that, however, let us specify the operators which enable one to move between grids of different number of nodes.

2.2.2.2   Inter–grid operators

Let Ω^h represent a one–dimensional grid with spacing $h = \frac{1}{N}$ and number of nodes N. The *prolongation* operator I_{2h}^h, which acts from Ω^{2h} to Ω^h and refines the grid (i.e. inserts new nodes) is specified as:

$$\boldsymbol{I}_{2h}^h \boldsymbol{\varphi}^{2h} = \boldsymbol{\varphi}^h \tag{2.50}$$

In the case of linear interpolation vector elements satisfy:

$$\begin{array}{rcl}
\varphi_{2j}^h &=& \varphi_j^{2h} \\
\varphi_{2j+1}^h &=& \frac{1}{2}(\varphi_j^{2h} + \varphi_{j+1}^{2h}) \qquad 0 \le j \le \dfrac{N}{2} - 1 \\
\varphi_N^h &=& \varphi_{N/2}^{2h}
\end{array} \tag{2.51}$$

Analogously, we can specify the *restriction* operator I_h^{2h}, which transfers the vectors from Ω^h to Ω^{2h}, coarsening the grid:

$$\boldsymbol{I}_h^{2h} \boldsymbol{\varphi}^h = \boldsymbol{\varphi}^{2h} \tag{2.52}$$

The *full weighting* restriction operator is defined by the vector relations as:

$$\begin{array}{rcl}
\varphi_0^{2h} &=& \varphi_0^h \\
\varphi_j^{2h} &=& \frac{1}{4}(\varphi_{2j-1}^h + 2\varphi_{2j}^h + \varphi_{2j+1}^h) \qquad 1 \le j \le \frac{N}{2} - 1 \\
\varphi_{N/2}^{2h} &=& \varphi_N^h
\end{array} \tag{2.53}$$

In the latter case the restriction operator is related with the prolongation operator as:

$$\boldsymbol{I}_{2h}^h = c(\boldsymbol{I}_h^{2h})^T, \qquad c \epsilon \Re \tag{2.54}$$

where c denotes a constant. The coarse version of the matrix $\boldsymbol{C}$ is specified as [77, 5]:

$$\boldsymbol{C}^{2h} = \boldsymbol{I}_h^{2h} \boldsymbol{C}^h \boldsymbol{I}_{2h}^h \tag{2.55}$$

2.2.2.3   Nested iteration

One of the methods to improve a convergence of an iterative solver is so–called nested iteration (1). In this method the iteration starts on a very coarse grid and then after a few iterations successively moves to the finer ones. The idea of the nested iteration is to obtain better initial guesses for the finer grids from the prolongated coarser grid solutions. The use of a coarse grid as a starting point for the iteration gives the following advantages:

- The smaller grid size (N in equation (2.49)) improves the convergence of smooth modes.

- Iteration on a coarse grid is relatively fast due to the smaller problem size.

- There is a good initial guess on a fine grid.

Nevertheless, the problem might still be unresolved if the smooth error components still exist on the fine grid causing the iteration to stall.

Algorithm 1   THE NESTED ITERATION

(p.1) Iterate on $\boldsymbol{C}^{ph}\boldsymbol{\phi}^{ph} = \boldsymbol{b}^{ph}$ on a very coarse grid Ω^{ph} with arbitrary initial guess $\boldsymbol{\varphi}^{ph}$.

(p-1.1) Iterate on $\boldsymbol{C}^{(p-1)h}\boldsymbol{\phi}^{(p-1)h} = \boldsymbol{b}^{(p-1)h}$ on $\Omega^{(p-1)h}$ with initial guess $\boldsymbol{\varphi}^{(p-1)h} = \boldsymbol{I}_{ph}^{(p-1)h}\boldsymbol{\varphi}^{ph}$.

$\vdots$

(2.1) Iterate on $\boldsymbol{C}^{2h}\boldsymbol{\phi}^{2h} = \boldsymbol{b}^{2h}$ on Ω^{2h} with initial guess $\boldsymbol{\varphi}^{2h} = \boldsymbol{I}_{3h}^{2h}\boldsymbol{\varphi}^{3h}$.

(1.1) Iterate on $\boldsymbol{C}^{h}\boldsymbol{\phi}^{h} = \boldsymbol{b}^{h}$ on Ω^{2h} with initial guess $\boldsymbol{\varphi}^{h} = \boldsymbol{I}_{2h}^{h}\boldsymbol{\varphi}^{2h}$.

2.2.2.4   Coarse grid correction

Another way to improve the convergence of iteration methods is to use the coarse grid correction scheme:

Algorithm 2   THE COARSE GRID CORRECTION

(1.1) Iterate n_1 times on $\boldsymbol{C}^h\boldsymbol{\phi}^h = \boldsymbol{b}^h$ on Ω^h with initial guess $\boldsymbol{\varphi}^h$.

(1.2) Compute residual $\boldsymbol{r}^{2h} = \boldsymbol{I}_h^{2h}(\boldsymbol{b}^h - \boldsymbol{C}^h\boldsymbol{\varphi}^h)$.

  (2.1) Solve $\boldsymbol{C}^{2h}\boldsymbol{e}^{2h} = \boldsymbol{r}^{2h}$ or iterate with initial guess $\boldsymbol{e}^{2h} = 0$ on
  Ω^{2h} to obtain an approximation to the error $\boldsymbol{e}^{2h}$.

(1.3) Correct fine grid approximation: $\boldsymbol{\varphi}^h \leftarrow \boldsymbol{\varphi}^h + \boldsymbol{I}_{2h}^h\boldsymbol{e}^{2h}$.

(1.4) Iterate n_2 times on $\boldsymbol{C}^h\boldsymbol{\phi}^h = \boldsymbol{b}^h$ on Ω^h with initial guess $\boldsymbol{\varphi}^h$.

In the first step the oscillatory components of the error are eliminated after selected number of iterations (usually n_1 equals 1, 2 or 3). Then, in the second step, the residual of the original equation is found and transferred to a coarser grid. The operation on residual equation is equivalent to the operation on the original problem, with the difference that one can start with the exact initial guess (which is equal zero), which may improve the convergence. On coarser mesh, the smooth error modes become more oscillatory. Thus the iteration is more effective. Of course, if the grid is coarse enough, the direct solution of residual equation is preferable. Then the computed error is transferred back to the fine grid in order to correct previously approximated solution. The last step smoothes the final solution.

2.2.2.5   The basic V–cycle

If we embed the coarse grid correction scheme within itself we can further improve the convergence. The algorithm for embedded coarse grid correction is called the basic multigrid V-cycle (Algorithm 3). The V-cycle is schematically drawn in Figure 2.8. The procedure starts on a fine grid and then subsequently moves to the coarser grids. It successfully removes the smooth error components with just a few iteration steps on each level, until the required precision is obtained. On the way back the solution is corrected on each level by its coarse grid approximation and serves as an initial guess for additional iterations. The memory requirement for the V-cycle is [5]:

$$S < \frac{2N}{1 - 2^{-d}} \tag{2.56}$$

for d–dimensional grid with N^d points and $N = 2^n$. It can be seen, that the memory usage does not increase significantly compared to the dense problem alone. This is especially true for three dimensional case, for which storage requirement slightly exceeds twice that of the dense grid problem.
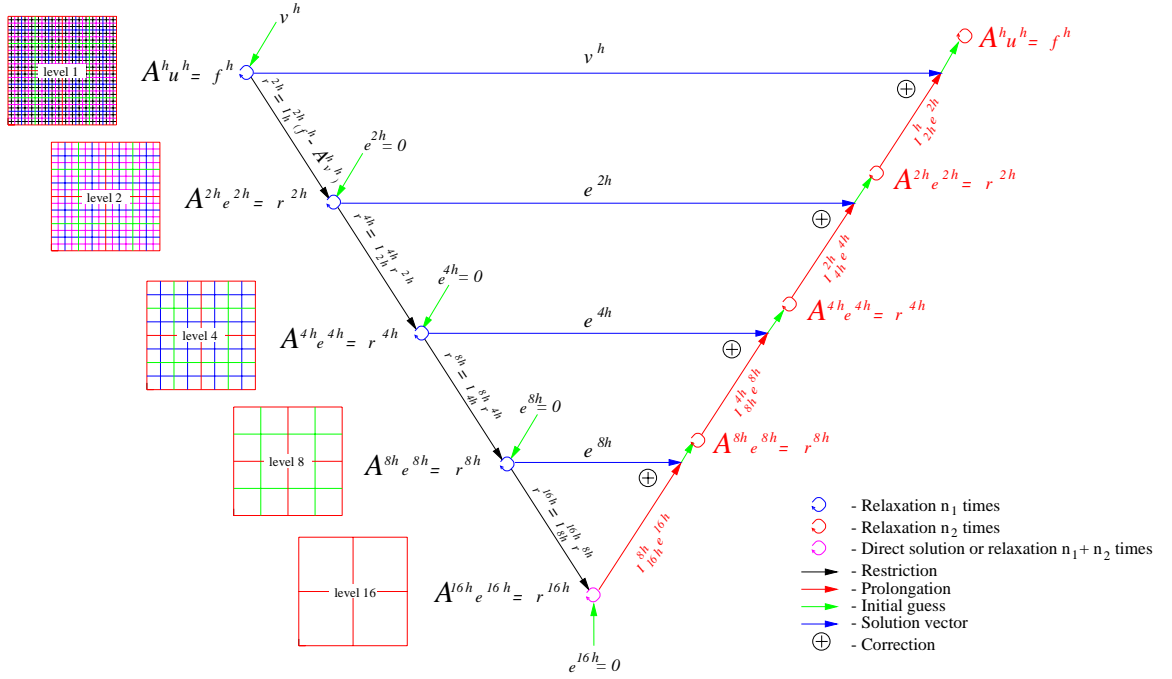
v^h

level 1

$A^h u^h = f^h$

$r^{2h} = I_h^{2h}(f^h - A^h u^h)$

v^h

$A^h u^h = f^h$

$e^{2h} = 0$

level 2

$A^{2h} e^{2h} = r^{2h}$

$r^{4h} = I_{2h}^{4h} r^{2h}$

e^{2h}

$A^{2h} e^{2h} = r^{2h}$

$I_{2h}^h e^{2h}$

$e^{4h} = 0$

level 4

$A^{4h} e^{4h} = r^{4h}$

$r^{8h} = I_{4h}^{8h} r^{4h}$

e^{4h}

$A^{4h} e^{4h} = r^{4h}$

$I_{4h}^{2h} e^{4h}$

$e^{8h} = 0$

level 8

$A^{8h} e^{8h} = r^{8h}$

$r^{16h} = I_{8h}^{16h} r^{8h}$

e^{8h}

$A^{8h} e^{8h} = r^{8h}$

$I_{8h}^{4h} e^{8h}$

level 16

$A^{16h} e^{16h} = r^{16h}$

$I_{16h}^{8h} e^{16h}$

$e^{16h} = 0$

◯ - Relaxation n_1 times
◯ - Relaxation n_2 times
◯ - Direct solution or relaxation $n_1 + n_2$ times
⟶ - Restriction
⟶ - Prolongation
⟶ - Initial guess
⟶ - Solution vector
⊕ - Correction

Figure 2.8: *Nested coarse grid correction, the so–called V–cycle*

Algorithm 3   THE V-CYCLE

(1.1) Iterate on $\boldsymbol{C}^h \boldsymbol{\phi}^h = \boldsymbol{b}^h$ n_1 times with initial guess $\boldsymbol{\varphi}^h$.

(1.2) Compute $\boldsymbol{r}^{2h} = \boldsymbol{I}_h^{2h}(\boldsymbol{b}^h - \boldsymbol{C}^h \boldsymbol{\varphi}^h)$.

    (2.1) Iterate on $\boldsymbol{C}^{2h} \boldsymbol{e}^{2h} = \boldsymbol{r}^{2h}$ n_1 times with initial guess $\boldsymbol{e}^{2h} = 0$.

    (2.2) Compute $\boldsymbol{r}^{4h} = \boldsymbol{I}_{2h}^{4h} \boldsymbol{r}^{2h}$.

        (4.1) Iterate on $\boldsymbol{C}^{4h} \boldsymbol{e}^{4h} = \boldsymbol{r}^{4h}$ n_1 times with initial guess $\boldsymbol{e}^{4h} = 0$.

        (4.2) Compute $\boldsymbol{r}^{8h} = \boldsymbol{I}_{4h}^{8h} \boldsymbol{r}^{4h}$.

            ⋮

           (p.1) Solve $\boldsymbol{C}^{ph} \boldsymbol{\phi}^{ph} = \boldsymbol{b}^{ph}$.

            ⋮

        (4.3) Correct $\boldsymbol{e}^{4h} \leftarrow \boldsymbol{e}^{4h} + \boldsymbol{I}_{8h}^{4h} \boldsymbol{e}^{8h}$.

        (4.4) Iterate on $\boldsymbol{C}^{4h} \boldsymbol{e}^{4h} = \boldsymbol{r}^{4h}$ n_2 times with initial guess $\boldsymbol{e}^{4h}$.

    (2.3) Correct $\boldsymbol{e}^{2h} \leftarrow \boldsymbol{e}^{2h} + \boldsymbol{I}_{4h}^{2h} \boldsymbol{e}^{4h}$.

    (2.4) Iterate on $\boldsymbol{C}^{2h} \boldsymbol{e}^{2h} = \boldsymbol{r}^{2h}$ n_2 times with initial guess $\boldsymbol{e}^{2h}$.

(1.3) Correct $\boldsymbol{\varphi}^h \leftarrow \boldsymbol{\varphi}^h + \boldsymbol{I}_{2h}^h \boldsymbol{e}^{2h}$.

(1.4) Iterate on $\boldsymbol{C}^h \boldsymbol{\phi}^h = \boldsymbol{b}^h$ n_2 times with initial guess $\boldsymbol{\varphi}^h$.

The computational cost in turn is of order $\mathcal{O}(N^d \log N)$, which is very close to optimal $\mathcal{O}(N^d)$ [5, 32]. The algorithm can also be easily programmed if called recursively. In this case the residual vector $\boldsymbol{r}$ is represented as another right-hand side vector $\boldsymbol{b}$ and $\boldsymbol{e}$ as another vector $\boldsymbol{v}$:

Algorithm 4   RECURRENT V-CYCLE

$$\boldsymbol{\varphi}^h \leftarrow MV^h(\boldsymbol{\varphi}^h, \boldsymbol{b}^h)$$

(1.1) Iterate n_1 times on $\boldsymbol{C}^h \boldsymbol{\phi}^h = \boldsymbol{b}^h$ with a given initial guess $\boldsymbol{\varphi}^h$.

(1.2) If Ω^h = coarsest grid then go to (1.4).
      Else:

    (2.1) $\boldsymbol{b}^{2h} \leftarrow \boldsymbol{I}_h^{2h}(\boldsymbol{b}^h - \boldsymbol{C}^h \boldsymbol{\varphi}^h)$

    (2.2) $\boldsymbol{\varphi}^{2h} \leftarrow 0$

    (2.3) $\boldsymbol{\varphi}^{2h} \leftarrow MV^{2h}(\boldsymbol{\varphi}^{2h}, \boldsymbol{b}^{2h})$.

(1.3) Correct $\boldsymbol{\varphi}^h \leftarrow \boldsymbol{\varphi}^h + \boldsymbol{I}_{2h}^h \boldsymbol{\varphi}^{2h}$.

(1.4) Iterate n_1 times on $\boldsymbol{C}^h \boldsymbol{\phi}^h = \boldsymbol{b}^h$ with initial guess $\boldsymbol{\varphi}^h$.

2.2.2.6   The Full Multigrid V–cycle

The full multigrid V-cycle is a method, which combines the algorithms of nested iteration and embedded coarse grid correction. While in the V-cycle alone an arbitrary initial guess was used as a starting point, here the initial guess is carefully prepared by several smaller V-cycles performed on different levels of the grid. The cycle is schematically presented in figure 2.9 and its algorithm can also be written recursively:

Algorithm 5   THE FULL MULTIGRID V-CYCLE (FMV)

$$\boldsymbol{\varphi}^h \leftarrow FMV^h(\boldsymbol{\varphi}^h, \boldsymbol{b}^h)$$

(1.1) If Ω^h = coarsest grid, then go to step (1.3).
      Else:

    (2.1) $\boldsymbol{b}^{2h} \leftarrow \boldsymbol{I}_h^{2h}(\boldsymbol{b}^h - \boldsymbol{C}^h \boldsymbol{\varphi}^h)$

    (2.2) $\boldsymbol{\varphi}^{2h} \leftarrow 0$

    (2.3) $\boldsymbol{\varphi}^{2h} \leftarrow FMV^{2h}(\boldsymbol{\varphi}^{2h}, \boldsymbol{f}^{2h})$.

(1.2) Correct $\boldsymbol{\varphi}^h \leftarrow \boldsymbol{\varphi}^h + \boldsymbol{I}_{2h}^h \boldsymbol{\varphi}^{2h}$.

(1.3) $\boldsymbol{\varphi}^h \leftarrow MV^h(\boldsymbol{\varphi}^h, \boldsymbol{f}^h)$ n_0 times.
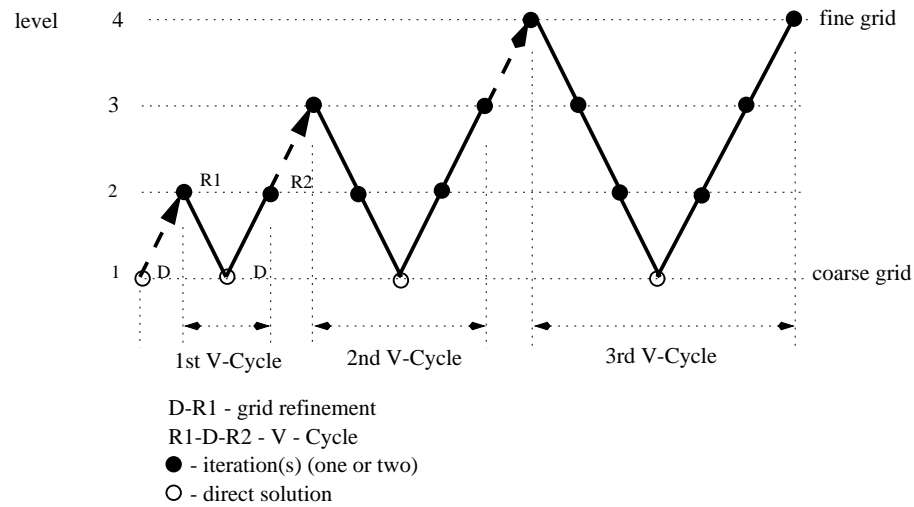

Figure 2.9: *Schematic representation of Full multigrid V-cycle.*

Although, one FMV cycle costs more than a single V-cycle (as it consists of a number of them) it is more effective and its computational cost is of the optimal order $\mathcal{O}(N^d)$, i.e. the number of operations is proportional to the number of unknowns.

2.2.3   Adaptive techniques

The considerations presented in previous section have shown that multigrid techniques can be employed in order to efficiently solve the system of linear equations resulting form the finite element discretization. Since this method operates on grids of different levels the adaptive techniques can easily be applied. They perform a local mesh adaptation according to the error estimator indicating where the domain refinement would be computationally most profitable. It may be especially effective for the FMV cycle, as the algorithm starts on a coarse grid, which can then be effectively refined using an adaptive technique. Such an approach reduces the memory requirements and shortens the solution time. This is explained by the fact that the adaptively refined grid has much fewer nodes for the same level of the solution error than the one refined uniformly. Nonetheless, the error estimation procedures can take a lot of time effort, as the local error estimation has to be calculated for each of the grid element. If a grid contains a large number of elements, the calculation of error estimation may significantly exceed the time required for the solution of system of equations (see Chapter 4).

2.3   Preconditioning

Another method of improving an efficiency of an iterative solver is a preconditioning of the original system of equations. Preconditioning is a way of transforming the original system of equation into another system that has the same solution, but can be solved faster using an iterative solver. In general, preconditioning decreases the condition number of a matrix, causing a system of equations to be better conditioned (the smaller a condition number, the better a system of equations is conditioned).

Such a transformation (preconditioning) of the linear system (2.40) can be written as:

$$M^{-1}C\phi = M^{-1}b \tag{2.57}$$

where M is a transformation matrix. If one would guess a matrix M so that is equal to a system matrix C, then such a preconditioning would result in a solution of the system within one step. Obviously this is not possible in general so a process of preconditioning is a process of approximation of the inverse of the original system matrix.

Preconditioning of the linear system (2.40) is often performed by a transformation matrix factorized as follows:

$$M = FG \tag{2.58}$$

in such a case (2.40) is transformed into

$$F^{-1}CG^{-1}G\phi = F^{-1}b \tag{2.59}$$

improving a condition number of $F^{-1}CG^{-1}$. If C is symmetric, a preconditioner should be chosen so that:

$$G = F^T \tag{2.60}$$

In simplest cases, a transformation matrix can be chosen as the diagonal of the original matrix C (Jacobi preconditioning) or may represent some more complicated mapping like incomplete LU factorization or even FFT transforms [55]. Looking at the equation (2.55) one can see, that multigrid algorithms are also a specific way of preconditioning called *multigrid* or *multilevel* preconditioning (in such a case all other preconditioning is distinguished as a *single–level* preconditioning).

Nonetheless, a selection of an optimal preconditioner for a specific system of equations in not an easy task. This can be concluded with the words of Y. Saad: *"Finding a good preconditioner to solve a given sparse linear system is often viewed as a combination of art and science. Theoretical results are rare and some methods work surprisingly well, often despite expectations (...)"* [55].

2.4   Notes on the chapter

In this chapter we have defined the boundary value problem and reviewed the numerical methods for its solution. We have concluded (2.2), that irregular grid can successfully be used for the specified problem and is preferred over the regular grid. Irregular grid can much better approximate the shape of the domain using more memory for grid storage but resulting in smaller linear algebra problem (due to smaller number of nodes).

Chapter 3

Treatment Planning

The main goal of treatment planning is to give guidelines for clinical personnel on settings or adjustment of parameters of a hyperthermia device required to obtain optimal temperature distribution (according to a tumor position) in a patient undergoing treatment. Another field of application of a treatment planning is to determine the physical behavior of the hyperthermia device in different anatomies and a posteriori evaluation of data acquired during treatment in order to learn from treatments and improve treatment strategy. Other specific features of a treatment planning for the problem at hand include the following factors:

- the procedure should rely as much as possible on brachytherapy – it implies no computer tomography and reading of the position of the applicator from the X-ray scans;

- it should use easy available (free) software to reduce the cost;

- since off–the–shelf packages can not be used, additional modules and algorithms have been devised and implemented;

The computer simulation of the absorbed power and of the temperature distribution within defined domain is necessary to optimize a hyperthermia treatment. Depending on the hyperthermia technology (see section 1.1.1.2), region it is applied to, and improvement of computer hardware, different approaches and various numerical techniques have been used and described in literature [75, 66, 26]. Generally, hyperthermia treatment planning consists of the following steps:

- **Segmentation.** In this step the geometry and boundary conditions of the computational domain are specified. For the case of regional hyperthermia, a large part of the patient body is modeled with the use of a computer tomography (CT). Then the CT slices are processed manually or semi-automatically in order to distinguish internal organs and assign appropriate values of electrical

permittivity and conductivity and generate a grid for the numerical calcula-
tions. This step is very time consuming and usually performed a day or two
before treatment is performed [65, 1]. For local hyperthermia, however, only
a small region is discretized and thus, does not require a considerable large
effort. For intracavitary or interstitial trials, the position of the applicators
can be obtained form two perpendicular radio–graphs and tissues might be
assumed to be homogeneous.

- **Grid generation** is of little endeavor for methods with regular grids. In
  the finite element based approaches, where grid is unstructured, the quality
  of the mesh influences not only the the solution error, but also the time and
  memory consumption used by the solver. Thus, this step is more crucial for
  the results and some sophisticated procedures are used [61, 1]. Essentially two
  steps are needed to generate a tetrahedral grid from already segmented data:
  a reconstruction of a surface model and then generation of tetrahedra in the
  volume surrounded by the defined surfaces.

- **Numerical evaluation.** The problem discretized in a previous step is as-
  sembled and a resulting set of equation is solved. In some approaches the
  solution includes only basic solution modes, from which any arbitrary solution
  is obtained by manipulation of magnitudes and phases and application of a su-
  perposition principle [8]. Then, having calculated a power distribution within
  a body, the bio–heat transfer equation (2.16) is solved [1].

- **Optimization** procedure which maximizes the temperature within the tumor
  region and minimizes in healthy tissues is also supplied in some treatment
  planning procedures [79, 1, 69]. These approaches use an objective function,
  which penalizes temperatures – in a tumor if below 43°C and in healthy tissues
  if above 42°C.

- **Visualization** is essential from the clinician point of view and should clearly
  show the areas of elevated temperature within the body in order to allow an
  appropriate selection of magnitudes and phases of a hyperthermia device. The
  presentation of the data in 3D region is not an easy task and some commercially
  available packages like AVS[1] or Iris Explorer can be used or some object-
  oriented class graphical libraries like Open Inventor [1] are incorporated into
  systems. Three dimensional data in those systems can be presented as 3D
  iso–surfaces or as two dimensional slices with color or contour plots.

---

[1]Advanced Visualization Systems Inc.

In this work, a number of software tools, creating the treatment planning system, have been implemented. The general structure of the system is described in a flow chart in the next section. A more detailed description of system components is given afterwards. The approach used in treatment planning for the SAR distribution has also been presented by the author in [82], [84] and [85].

3.1   The flow chart

Treatment planning system, developed in this work, consists of a number of software tools, procedures and data interfaces. Those are presented in the flow chart in figure 3.1. Framed numbers in the text refer to the numbers in upper left corner of the flow chart boxes.

After the modified Fletcher-Suit applicator has been inserted into a patient, two radio-graphs (anterior-posterior and lateral) are taken $\boxed{1}$ in order to obtain applicator's coordinates in the patient body (Fig. 3.2). The radio-graphs are scanned into a computer and then the user indicates with the mouse on the screen specific points of the electrodes, whose coordinates are then calculated $\boxed{2}$. Based on these coordinates a developed program (as described in Appendix B.2) generates the surface model $\boxed{3}$ of the Fletcher-Suit applicator (Fig. 3.3b). The surface model of the applicator is then used as an input for the tetrahedral grid generator `tetgen` $\boxed{4}$. Then the boundary conditions are specified for each boundary of the domain $\boxed{5}$. The adaptive, multigrid code KASKADE [2, 3] was used for the calculation of the three basic modes of the solution $\boxed{6}$. Adaptive mechanism gives different final meshes for each of 3 basic excitations, and thus if used, additional mesh interpolation[2] is needed in order to use the superposition principle (2.15). A grid interpolation procedure $\boxed{7}$ transforms the three basic solutions to a single grid (see Appendix B.1 for details). These solution are saved on a disk $\boxed{8}$ and can be summed up with prescribed amplitudes and phases $\boxed{9}$. Further calculations compute the power distribution (2.2) $\boxed{10}$. Based on this, the SAR pattern can be visualized $\boxed{11}$ or the KASKADE program can be used for further calculation of temperature distribution $\boxed{12}$ and its visualization $\boxed{13}$. Arrows with dashed lines represent the loop-back, which can be performed if one wants to optimize excitation parameters (i.e. perform the simulation for another excitation parameters).

---

[2]This term means, that the nodes of the new grid are assigned to fit to cells of a tetrahedral grid. Although, the word *conversion* could better describe this operation, the word *interpolation* is used, because the results which are assigned to the nodes of a one grid are also being interpolated to the another one.
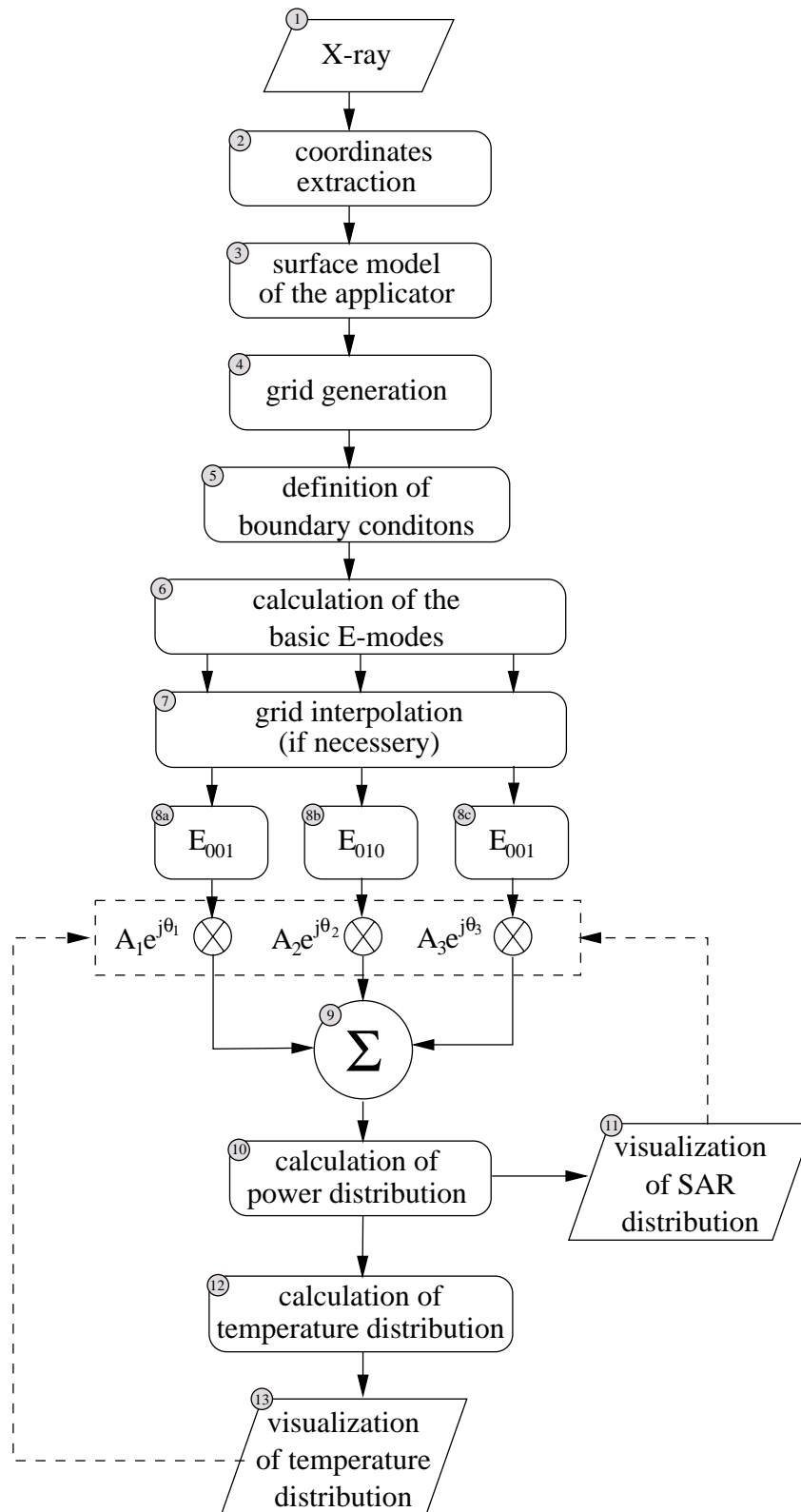
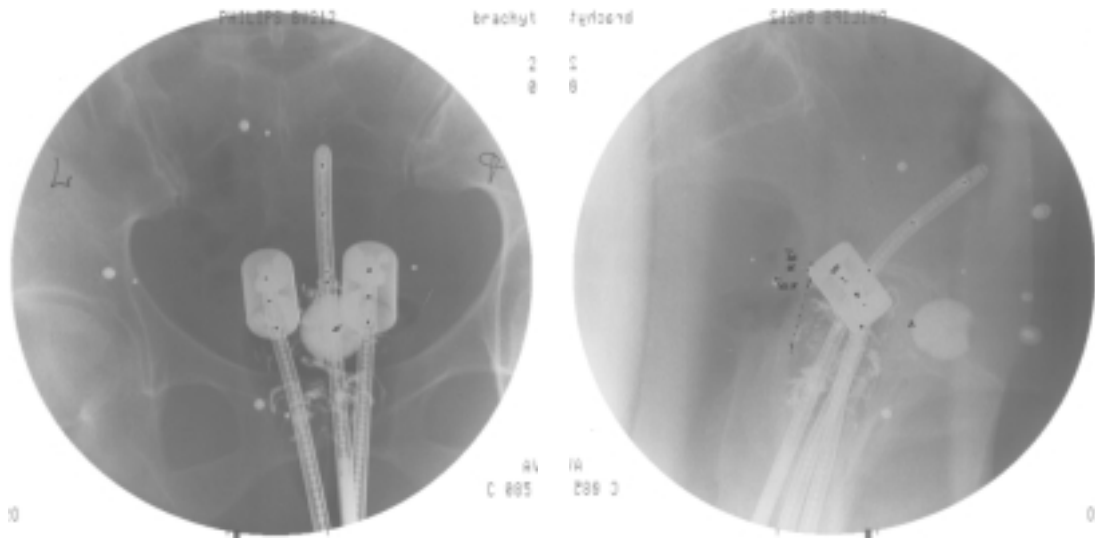Figure 3.1: *Flow chart of the treatment planning*

Figure 3.2: *Orthogonal radio-graphs (anterior-posterior and lateral) with the modified Fletcher-Suit applicator in the treatment position. The spherical arte-facte in picture left is due to catheter balloon in a bladder.*

3.2   Data input and grid generation

A simulation requires the physical data to be represented in a computer space. A standard method in many applications is to make computer tomography (CT) slices and to digitize them. This approach is very accurate and enables one to identify different internal tissues. However, the 3D segmentation is a very time consuming procedure and, as already mentioned, might preclude the simulation and treatment within the same day [3, 60]. Moreover, precise tissue modeling is not as important as in regional hyperthermia, where electromagnetic radiation covers a large region of the body. In our case, the heat source adheres directly the muscle tissue, where the highest values of power density are obtained. Although the recognition of internal tissues would much improve the precision of the solution, this would much complicate the procedure, as CT is not required for brachytherapy treatment. One also needs to remember that the hyperthermia treatment is to be performed before brachytherapy treatment can be initialized. Thus, the approach, which is common with the brachytherapy treatment planning has been used. Two perpendicular radio-graphs of a patients' lower abdomen are taken (Figure 3.2) and scanned into a computer [1]. Then, using the software for the brachytherapy treatment planning, the coordinates defining the position of the applicator within the body are extracted [2]. A number of different grid generators have been tested in order make the best
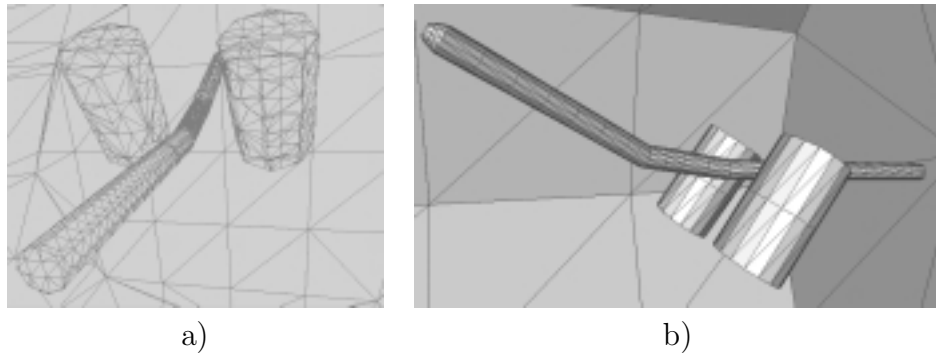
a)   b)

Figure 3.3: *a) The surface triangulation made by the* `qmg` *mesh generator b) The surface triangulation of the applicator for* `tetgen` *grid generator*

possible selection. Actually, only two of them `qmg`[3] and `tetgen`[4] were able to generate a mesh for our domain. The problem was to obtain a mesh as coarse as possible in order to have a smaller problem size and to effectively refine the mesh.

The `qmg` mesh generator [74] is a highly automatic public domain program, which generates a surface triangulation and a tetrahedral grid for the domain. Unfortunately this program resulted in a large number of elements and poor approximation of applicator's shape (note, that in Figure 3.3a the cylindrical shapes are approximated by right regular prisms with 10 sides and the tandem has no rounded ending). The number of nodes varied from 10,000 to 45,000 (accordingly 46,000 to 201,000 of tetrahedra) depending on applicator's position and its shape approximation. An example of the surface triangulation generated by the `qmg` program is presented in Figure 3.3a. It might be seen, that triangles are very irregularly spaced and many of them have large ratio of edges.

Another program, `tetgen`, requires the surface mesh as an input. Thus, the program, which generates the surface model of the applicator has been developed ⟦3⟧. The surface model consists of a number of triangles and thus the cylindrical shapes are approximated by right regular prisms (more details are given in Appendix B.2). The user can define the number of sides for each part of a domain. The more sides, the better is the approximation of the shape, but also a larger mesh and a longer time of the tetrahedral mesh generation. Proper triangle sizes and their aspect ratios (ratio of edges within each triangle) are also of importance in order to obtain a good quality of a grid. The quality of the surface triangulation influences the quality and size of the final 3D grid. Then an initial tetrahedral grid is generated ⟦4⟧ and then special procedures for mesh improvement are used [3]. In contrast to the previous

---

[3]http://www.cs.cornell.edu/home/vavasis/qmg1.1/meshgen.html
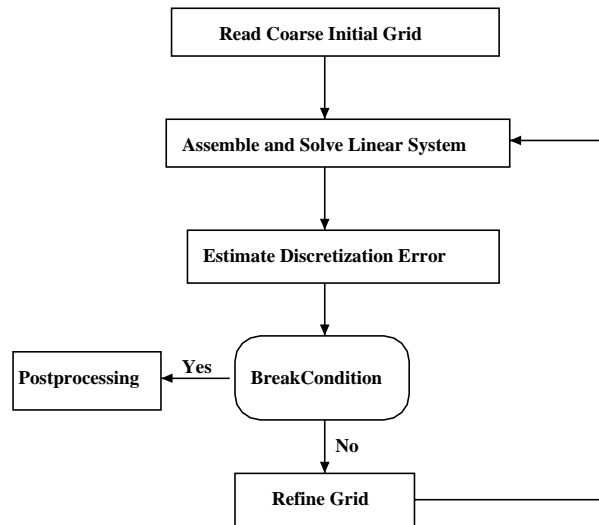[4]obtained from ZIB (Zentrum für Informationstechnik Berlin)

Figure 3.4: *Main iteration loop of the adaptive solution procedure in KASKADE. After [2].*

`qmg` program, it is possible to obtain the mesh for the same domain, which has only about 380 vertices and 1580 tetrahedra (against 45,000 vertices and 201,000 tetrahedra in `qmg` program). An example of the surface triangulation resulting from the tetrahedral grid is presented in Figure 3.3b.

3.3 Numerical solution

This section presents aspects of the computer implementation of the software used for the simulation of the SAR and temperature distribution.

The core of the simulation is the KASKADE program developed by ZIB [2, 3, 4]. This program has been modified in order to meet the requirements for hyperthermia treatment. The flow chart of the main iteration loop of the adaptive solution procedure in KASKADE is presented in Figure 3.4. In the first step, the program reads a coarse initial grid together with a definition of boundary conditions $\boxed{5}$. Then a linear system of equations is assembled and solved. Following this, a discretization error is estimated and checked if it is below or above a specified threshold. If not, the grid is refined and a new linear system is assembled and solved. If yes, the results are post-processed.

This program can solve elliptic partial differential equations of the form:

$$-\nabla k \nabla u + qu = f \tag{3.1}$$

with respect to u and with Dirichlet, Neumann or Cauchy boundary conditions. For

q and f equal to zero we get the Laplace equation equation (2.13) and as a solution, a voltage distribution, defined at vertices of a refined grid. In the simulation, however, we are interested in power and temperature distributions and thus additional modules for the calculations of those distributions have been implemented by the author.

The solution of a linear system in KASKADE can be performed in many different ways. Generally, the system may be solved using a direct or an iterative solver. It is profitable to use a direct solver if the number of nodes in the grid is relatively small (a KASKADE user can set the maximum number of nodes for a direct solver). The system matrix is sparse (compare section 2.2.1) and is solved in the program via LU-decomposition (Harwell-MA28 sparse matrix solver[5]). An alternative is to use iterative solvers which operate on a residual equation of the original system and use different kind of preconditioning in order to improve the convergence of the system (see Section 2.2). More specifically, it is possible to choose a single or multilevel preconditioner. The former one is a typical routine of Jacobi, SSOR or ILU preconditioning and are equivalent to the nested iteration scheme (section 2.2.2.3), while the latter offers additional choice between multigrid and multilevel type and are equivalent to the full multigrid V-cycle (section 2.2.2.6). Multilevel preconditioner computes the coarse grid matrices as specified in equation (2.55), in section 2.2.2.2. The multigrid preconditioner, however, simply stores the system matrix of selected refinement steps and use these ones for the relaxation operations. Multilevel and multigrid preconditioners are equivalent if a mesh is refined uniformly.

The error estimator provides estimates for the global and local discretization errors. The global error is used to stop the algorithm when the requested precision is reached. The local information gives the error on each element on the actual mesh. All those elements, whose error exceeds a specified limit are marked for refinement. The program also supports a uniform mesh refinement.

3.3.1   Calculations of power density

In FEM, an interpolation of the solution in an arbitrary point of an element is specified by a product of shape functions and nodal solution values (2.29). Thus, to obtain a gradient of a solution, one can multiply those nodal values by taking derivatives of shape functions:

$$\nabla\phi_e = \sum_i \nabla N_i(x,y)\phi_i^e \tag{3.2}$$

However, if the interpolation function over an element is of the first order (linear), the solution derivatives are then discontinuous on the element's boundaries and

---

[5]http://www.netlib.org/harwell, ftp://ftp.numerical.rl.ac.uk/pub/hsl/m.ps.gz
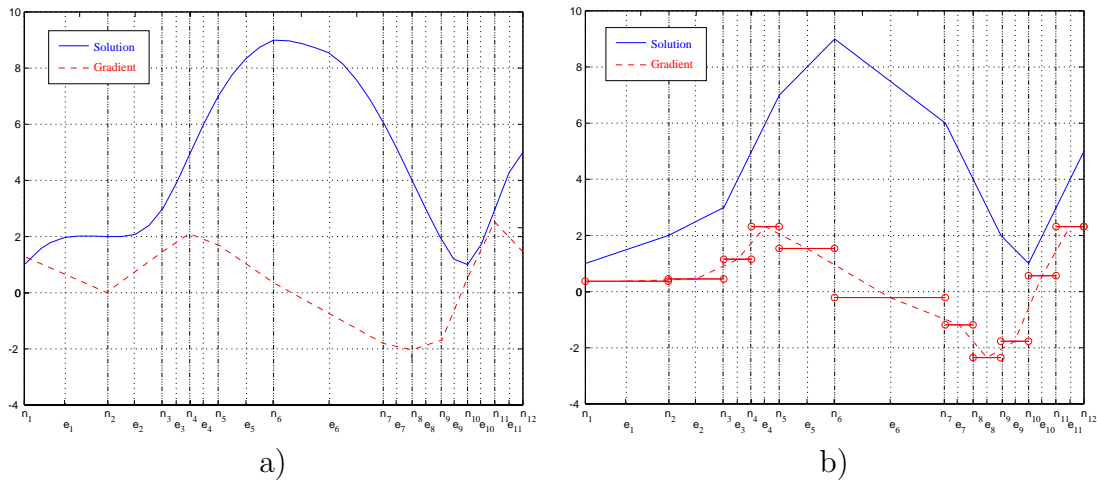
Figure 3.5: *One dimensional example of a solution and a gradient of the solution for quadratic (a) and linear (b) elements. The solution for linear elements is defined at nodes n_i. The solution for quadratic elements also contains nodes e_i. The gradient of the solution is defined at nodes e_i for linear elements and at nodes n_i for quadratic elements.*

constant within an element. If we use quadratic or higher order interpolation, then the continuity is preserved. Thus, the solution is to define a higher order polynomials for the interpolation functions in order to preserve the continuity for derivatives. An alternative is to use linear elements, but compute the gradient for the center point of each element, so as to avoid discontinuity on boundaries. A one dimensional example of such solutions is presented in Figure 3.5

The KASKADE system gives the possibility of selection between linear and quadratic interpolation functions, yet the latter one lacks the mechanism of adaptive refinement and multigrid preconditioning and uses nested iteration approach with uniform refinement scheme.

The comparison between the solutions with quadratic and linear interpolations have been performed by the author in order to select the one, which would be computationally more profitable. This comparison is discussed in detail in Chapter 4. It shows that, with quadratic elements, the results are always smoother, even the solution precision is at same level for both cases. The overall solution time for the quadratic elements was shorter. The memory usage, however, depended on the initial grid. If the initial grid was coarse (380 vertices), the quadratic elements with 2 uniform refinements required much less memory for the grid structure then linear elements with 7 adaptive refinement steps. For dense initial grid, however (19120 vertices), even one uniform refinement resulted in large number of nodes[6]

---

[6]Number of vertices in an element is always constant. Number of nodes, however, depends

and required a lot of memory for the system matrix.

All basic mode solutions for $\vec{E}$ are generated independently $\boxed{6}$ and, if an adaptive refinement is used, have different final grids. Thus, in order to apply the superposition principle (eq. 2.15) for the final distribution of electrical field, all the basic mode solutions have to be stored on the same grid. Therefore, a grid interpolation routine have been implemented $\boxed{7}$, as described in Appendix B.1. After the basic mode solutions are found and saved on a disk, a user specifies amplitudes and phases for each of the applicator's electrode and a final solution of power distribution is computed and saved in a file $\boxed{8}$,$\boxed{9}$.

An additional routine has been created in order to increase the number of possible solutions. This routine averages (or sums with different factors) two different patterns of $\vec{E}$ fields, which is equivalent to switching between two different excitations during treatment (see section 5.2 and Figure 5.2).

Once the final solution for $\vec{E}$ field is found, the SAR or power density patterns are easily computed $\boxed{10}$ using equations (2.1) or (2.2). Obtained results can be dumped into a matrix form or visualized in the AVS (Advanced Visual Systems Inc.) or `Amira` (ZIB product) visualization program using supported or implemented filters.

3.3.2   Calculation of temperature distribution

A steady state temperature distribution, which is described as an elliptic partial differential equation (2.17), can also be solved using KASKADE if the bio–heat transfer equation is written analogously to equation (3.1):

$$-\nabla \cdot (k\nabla T) + c_b W T = P + c_b W T_b \tag{3.3}$$

with $q = c_b W$ and $f = P + c_b W T_b$. Some modification in the program were required in order to use the previously calculated data of power density. A grid with P values defined at each vertex are read in at the program initialization. Then, during the assembling of system of equations, P values are interpolated on a grid resulting from the initial problem triangulation (the same initial grid is used for both formulations, only boundary conditions are modified. The final grid differs from the initial one, so grid conversion and solution interpolation is necessary).

The gradients of the solution are not the sought values in this simulation, thus the selection between quadratic and linear elements is not crucial. The quadratic elements, however, give smoother results in one wants to obtain the results on another

---

on the type of interpolation functions. For example, each tetrahedron has 4 vertices and 4 nodes if interpolation functions are linear and 10 nodes if interpolation functions are quadratic. See section 2.2.1 for details.

grid, which requires additional mesh interpolation. The adaptive grid refinements can also successfully be used in this simulation. (see section 4.1.2 for details).

3.4   Visualization

A number of possibilities exist to visualize obtained numerical results. The data structure in KASKADE program is stored as a tetrahedral grid with defined boundary triangles. The solution vector is associated with each vertex of a grid. The program has implemented a few filters to save data in different formats, among which are `ucd` format used in AVS[7] and `HyperMesh` format used in Amira[8]. Those programs can visualize tetrahedral grids and represent data on different grid cuts or as iso surfaces (different visualization methods have been used to present data in Chapter 5). Additionally, a module for grid conversions and data interpolation has been implemented, which enables data to be saved in a matrix form (3D regular grid or 2D slices) and then visualized in any other program handling such formats (for example Matlab has been used to present data in Figures 4.1 and 4.2).

3.5   Conclusions

A number of different software tools have been implemented or modified to needs of hyperthermia treatment of cervical malignancies. Six steps of the simulation can be distinguished:

1. Surface triangulation.

2. Grid generation.

3. Calculation of $\vec{E}$ – field distribution for 3 basic modes.

4. Determination of SAR for an arbitrary excitation.

5. Calculation of temperature distribution.

6. Visualization.

There is no automatic optimization currently implemented, yet the short evaluation time (see the next chapter) enables one to check a number of possible solution within minutes.

---

[7]Advanced Visual Systems Inc.
[8]http://amira.zib.de

Chapter 4

Numerical Tests

One of the goals of this work is to find the most effective approach (in terms of memory and time) of finding the SAR and temperature distributions. To this end a series of numerical tests have been carried out for different numerical solvers and grids. The results of these tests are given in this chapter. Some of them have also been reported in [83].

Most of numerical experiments have been performed for two grid generators `qmg` and `tetgen`, which have been mentioned in previous chapter. The comparison between those grid generators also shows the efficiency of the numerical methods for different densities of initial grids. The first section compares the evaluation times, memory requirements and error levels between quadratic and linear interpolation functions used in a solution process of SAR and temperature distributions. Section 4.2 shows how much time is being spent in each procedure of the simulation. In section 4.3 some comparisons concerning the usage of different preconditioners used in a solution process are given.

4.1 Quadratic vs. linear elements

Linear or quadratic interpolation functions can be used (see section 3.3) to interpolate the solution within an element of a finite element grid. The selection between those interpolation functions influences the number of nodes, and thus also the problem size which is to be solved. Another consequence in the matrix sparsity. In the KASKADE program, the use of quadratic elements precludes the usage of multigrid preconditioners and adaptive refinement. Therefore, the question appeared concerning the reason of usage the quadratic elements. This section analyses the numerical effectiveness of those two approaches, based on performed simulations. This comparison, however, should not be perceived as the comparison between the multigrid and single–level preconditioners. Such a comparison is presented in section 4.3.

Table 4.1: *Comparison of time and memory usage for quadratic and linear shape functions for the* qmg *grid generator. The memory usage for the solution matrix with the multigrid preconditioner consists of two components. The number of megabytes shown in parenthesis is associated with the additional memory required in multigrid scheme for the matrices from previous levels. Preconditioner type refers to a nomen-clature used in section 3.3 — a single–level preconditioning is equivalent to a nested iteration scheme and a multigrid preconditioning to a full multigrid V-cycle.*

Approximation type		quadratic	linear
Preconditioner type		single level	multigrid
Number of refinements		1 (uniform)	3 (adaptive)
Number of points		132755	126211
Number of nodes		989694	126211
Number of tetrahedra		692224	704221
Memory usage	grid	256 MB	264.7 MB
	solution matrix	171 MB	34.8(23) MB
	Total	**427 MB**	**299.5 MB**
Time	grid refinement	25.9 s.	119 s.
	update	33.2 s.	13.1 s.
	assembling	57.7 s.	28.7 s.
	(no of iterations) solution	(42) 107.5 s.	(30) 17.0 s.
	error estimation	1.7 s.	122 s.
	Total	**226.0 s.**	**299.8 s.**

4.1.1   Calculation of SAR distribution

The computation of SAR requires the computation of the gradients of the potential obtained from the solution of linear equations. As explained in point 3.3.1, two approaches are possible. The first approach used linear interpolation functions, with the gradient computed at the center of each element. The second approach used the quadratic elements.

The qmg mesh generator (see section 3.2) was the only one available at the beginning of this study. Thus, the comparison was performed for the grid generated by this program (view of the initial grid is shown in Figure 3.3a). The results are collected in Table 4.1 and in Figure 4.1. Number of refinements in Table 4.1 refers to the maximum possible refinement steps. This number is limited either by available
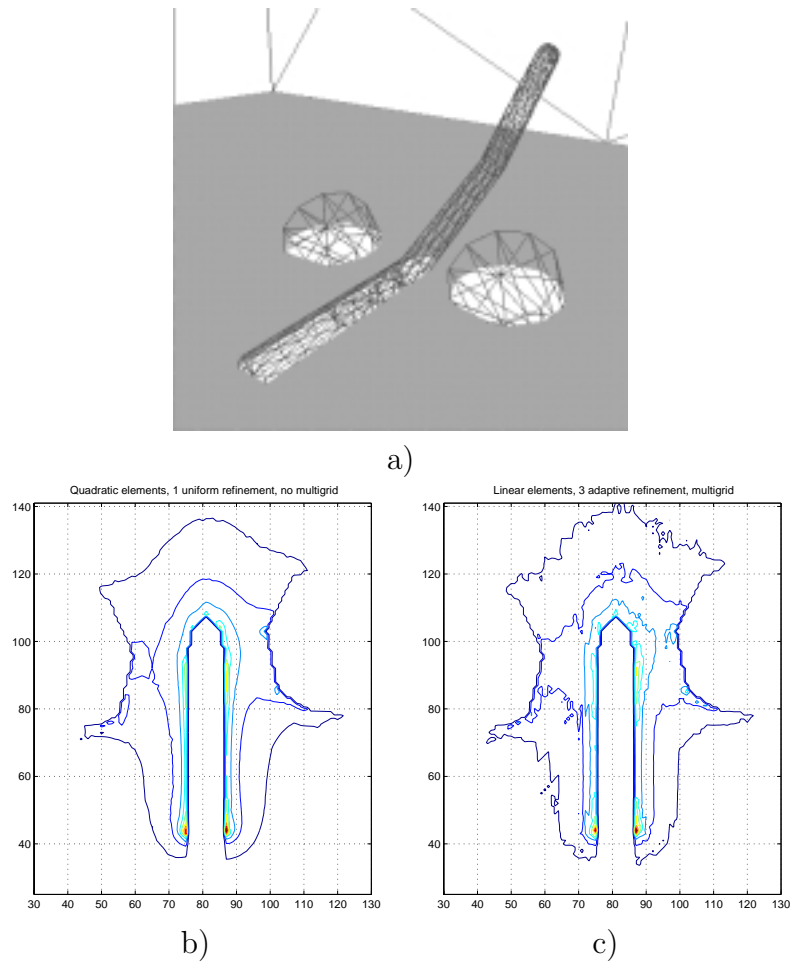
Figure 4.1: *gradient solution for different mesh refinement and quadratic and linear elements with initial grid oh 19120 nodes: a) The view of a cross–section selected for result presentation b) uniform refinement and quadratic elements c) adaptive refinement and linear elements*

memory or by tetrahedra, which even if marked for the refinement cannot be refined due to their small size or large ratio of edge lengths. Note, that only one uniform refinement was possible for quadratic elements. Adaptive mechanism, used with linear elements, allowed for 3 refinements. The memory consumption was about 40% larger for quadratic elements. Although the memory used for grid structure is comparable, the quadratic elements, due to a large number of nodes, use a lot of memory for a solution matrix. Also, the solution of the system of equations takes over 6 times longer for the quadratic elements. This is explained not only by the larger matrix size, but also by the fact that a single level preconditioner converges much slower than a multigrid preconditioner. Nonetheless, the adaptive mechanism of grid refinement is time expensive because it needs to estimate an error for each of

Table 4.2: *Comparison of time and memory usage for quadratic and linear shape functions for* `tetgen` *grid generator. The memory usage for the solution matrix with the multigrid preconditioner consist of two components. The number of megabytes shown in parenthesis is associated with the additional memory required for the storage of matrices from previous levels.*

Approximation type		quadratic	linear	linear
Preconditioner type		single level	multigrid	multigrid
Number of refinements		2 (uniform)	7 (adaptive)	3 (uniform)
Number of points		18664	71201	142060
Number of nodes		142060	71201	142060
Number of tetrahedra		101120	395389	808960
Memory usage	grid	19.6 MB	78.1 MB	152.6 MB
	solution matrix	24.8 MB	20.4(13.8) MB	29.2(15.8) MB
	Total	**44.4 MB**	**98.5 MB**	**181.8 MB**
Time	grid refinement	2.4 s.	32.9 s.	19.1 s.
	update	2.9 s.	3.9 s.	4.4 s.
	assembling	6.2 s.	11.7 s.	13.5 s.
	(iterations) solution	(71) 14.2 s.	(50) 9.2 s.	(38) 14.7 s.
	error estimation	0.1 s.	30.2 s.	0.5 s.
	Total	**25.8 s.**	**87.9 s.**	**52.2 s.**

the tetrahedron. Also, the adaptive refinement procedure requires more time than the uniform one. All those tests show, that linear elements with adaptive refinement and multigrid solution scheme requires about 30% more overall time, but about 40% less memory. Figure 4.1 presents contour plots of the $|E|$, (i.e. $|\nabla U|$) for both types of approximation for a selected case. The contours for quadratic approximation of the solution gradient are much smoother than for the linear elements, where gradients are constant within each element. The solution error, however, for both cases is at the same level.

The tests performed with `tetgen` grid generator, which generated much coarser and much better quality (i.e. better ratio of triangle edges) initial grid are gathered in Table 4.2 and in Figure 4.2. Note, that having a coarse initial grid (380 points), more refinements are possible. The memory requirements decreased significantly. In this case quadratic elements use almost 10 times less memory than with the `qmg` grid. The solution times have also significantly decreased - almost 9 times for
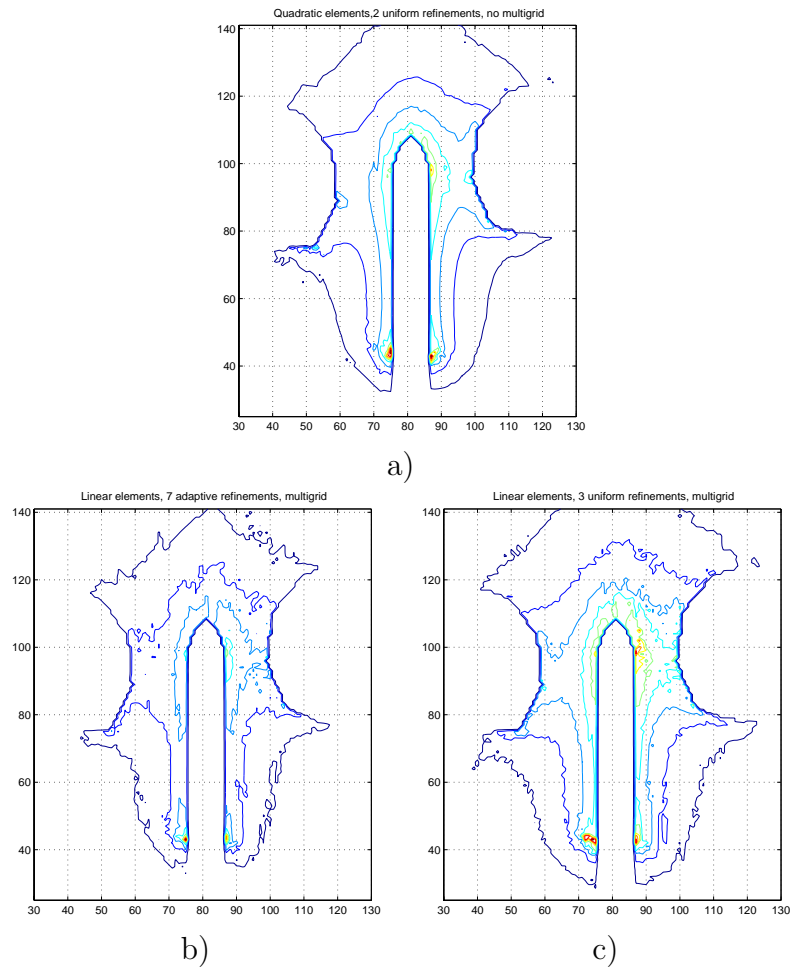
Figure 4.2: *Gradient solution for different mesh refinement and quadratic and linear elements for the cross–section as in Figure 4.1a a) uniform refinement and quadratic elements b) adaptive refinement and linear elements c) uniform refinement and linear elements.*

the quadratic and 3.5 times for linear elements. In this, case the solution time for multigrid scheme is also much shorter, but again an error estimation requires a lot of time effort.

The last column in Table 4.2 presents results for linear elements and uniform refinement with multigrid solution scheme. Three refinements with linear elements give the same number of nodes as for two refinements with quadratic elements. The grid structure, however, is much larger and thus much more memory and time is used for grid refinement and assembling. Although the solution time for the quadratic elements with single level preconditioner is very comparable to this case, the total number of iterations is reduced almost by a factor of 2 — this indicates much better convergence of the multigrid solver.

Table 4.3: *Comparison of time and memory usage for quadratic and linear shape functions for* `tetgen` *grid generator for the solution of a bio–heat transfer equation (3.3). The values of power density for both cases were interpolated from the lattice of 336336 elements obtained from the solution with quadratic elements. The interpolation procedure increases the time for the system assembling (compare with Table 4.2)*

Approximation type		quadratic	linear
Preconditioner type		single level	multigrid
Number of refinements		1 (uniform)	3 (adaptive)
Number of points		2562	1619
Number of nodes		18664	1619
Number of tetrahedra		12640	19776
Memory usage	grid	2.73 MB	4.2 MB
	solution matrix	3.16 MB	0.95 MB
	Total	**5.89 MB**	**5.15 MB**
Time	grid refinement	0.27 s.	0.83 s.
	update	0.37 s.	0.14 s.
	assembling	7.26 s.	4.85 s.
	solution	5.42 s.	0.37 s.
	error estimation	0.01 s.	14.47 s.
	Total	**13.33 s.**	**20.66 s.**

4.1.2   Calculation of temperature distribution

Temperature distribution is obtained by a solution of a bio-heat transfer equation for a steady state (3.3). As a result, the scalar field of a temperature distribution is returned. Table 4.3 compares the time and memory usage for quadratic and linear elements for 1 uniform and 3 adaptive refinements. The memory resources for both cases are very similar and the time is 30% shorter for the quadratic elements. Note, however, that the linear system solution time alone for the multigrid adaptive scheme takes about 7% of the solution time used with single level preconditioner. The rest of the time is used in error estimation, which is not performed in the second case.

Results obtained for both approaches — quadratic and linear elements — are shown in Figure 4.3. Cases a) and b) present solutions, which were interpolated on a
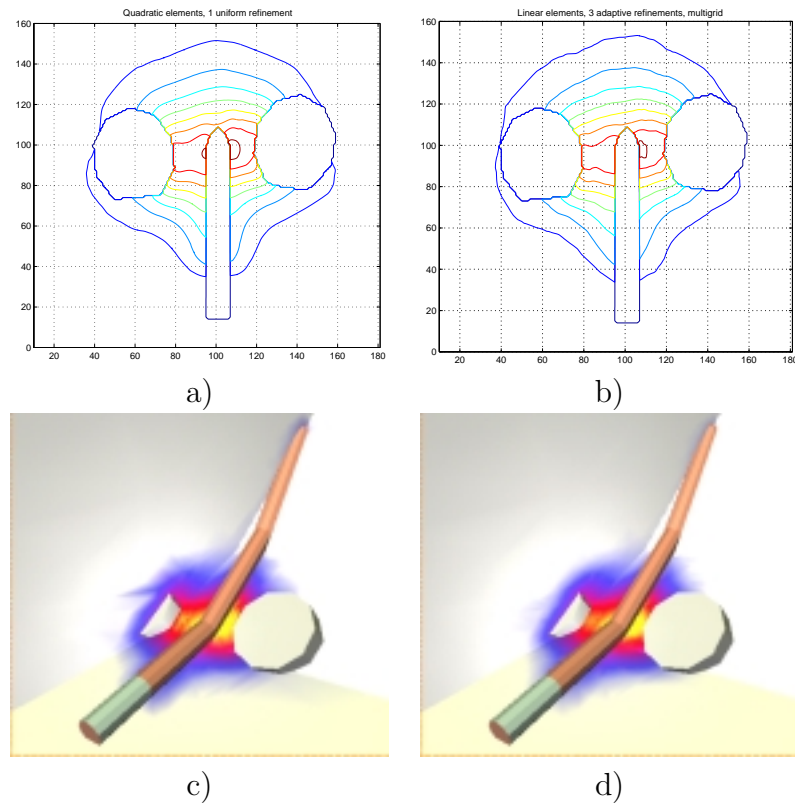
Figure 4.3: *An example of solution for quadratic and linear elements presented on different grids a) quadratic elements interpolated on a regular grid (cross–section) b) the same, but for the linear elements c) quadratic elements presented on original mesh in* `Amira` *program d) the same as previous, but for linear elements*

regular grid using interpolation functions (quadratic (a) and linear (b) respectively). Cases c) and d) present results, which were saved in a tetrahedral grid format and visualized in `Amira` visualization program. This format, however, defines only four nodes per tetrahedron. Thus, if quadratic elements were used in calculations (which are defined by 10 nodes per tetrahedron), significant information loss is encountered while saving data.

The conclusion is, that it is better to use linear elements with adaptive grid refinement if data are stored in a tetrahedral grid format. If solution is to be interpolated on a different grid, both approaches give comparable accuracy.

4.2   Evaluation times

Times required for modeling the SAR and temperature distribution for the `qmg` grid and 3 adaptive refinement steps and `tetgen` grid with two quadratic refinements are

Table 4.4: *The shortest overall solution time.* `qmg` *and* `tetgen` *grid generators.*
CPU: PII 350MHz. For the case of `tetgen` *grid generator, there is no need for*
mesh interpolation (as uniform grid refinements is used)

Grid generator		**qmg**	**tetgen**
Initial number of nodes		19120	380
Grid generation		**315 s.**	**72.15**
$\vec{E}$ – field distribution for a basic mode	Grid refinement	88.6 s.	2.51 s.
	Solution	12.2 s.	14.14 s.
	Error estimation	100.8 s.	0.06 s.
	Mesh interp. & gradient comput.	57.3 s.	11.12 s.
	Total	**314.7 s.**	**84.04**
Total (3 basic modes)		**944.1 s.**	**252.12 s.**
Field summation and calculation of SAR		0.2 s.	0.15 s.
Temperature distribution	Grid refinement	6.3 s.	0.27 s.
	Solution	5.2 s.	5.42 s.
	Error estimation	45.5 s.	0.01 s.
	Total	**70.6 s.**	**13.33 s.**
Total		**22:01 min.**	**4:26 min.**

presented in Table 4.4. The modeling was performed on a Pentium II processor with
a 350 MHz clock and 384 MB of RAM. Initial `qmg` grid was 19120 nodes and 86528
tetrahedra. The final grid resulted in 126211 points and 704221 tetrahedra. Initial
`tetgen` grid was 380 nodes and 1580 tetrahedra. The final grid resulted in 18664
points and 101120 tetrahedra. Then the `qmg` mesh was interpolated on a regular
grid with 336336 nodes. The `tetgen` grid was not interpolated on a regular grid as
a uniform grid refinement was used. The total modeling procedure for the `qmg` grid
takes 22 minutes. The most time is spent in grid generation, error estimation and
grid refinement. The second approach takes only 5 minutes and the most time is
spend in grid generation and solution.

4.3   Preconditioners

The results obtained using different preconditioners are presented in Table 4.5 and
in Figure 4.4. It can be inferred that, compared to the nested iteration scheme,

Table 4.5: *Comparison of total number of iterations, solution time and memory allocation for adaptive finite elements and multigrid schemes.*

Total problem size: 105445 (initial 3962)	Memory [MB]	Number of itera- tions	Total time [s]
Nested iteration – no preconditioning	222.6	772	74.45
Nested iteration – single level preconditioning	222.6	111	19.05
Full multigrid (multilevel preconditioning)	241.1	56	15.94

the full multigrid algorithm improves significantly the convergence for the problem at hand with similar number of iterations in each refinement step at the cost of some additional memory. Nevertheless, the solution time is only improved for the last refinement step for the largest problem size, as full multigrid preconditioning, although of optimal order, costs more than the single-level preconditioner. Top chart in Figure 4.4 presents number of iterations and bottom chart shows solution times per problem size (for selected refinement levels). Each refinement level uses the solution of its preceding level as an initial guess and is referred to as a nested iteration scheme. It can be seen, that the number of iterations increases significantly if no preconditioning is applied (except for the first level with arbitrary initial guess). The use of a single level preconditioning improves significantly the situation but still, the number of iterations increases with a problem size. The application of a full multigrid preconditioner results in the constant number or even decrease of the number of iterations, for the subsequent refinements. The solution time per one iteration is longer for multigrid algorithm, but one needs to keep in mind that, unlike in other methods, the number of iterations does not increase with each refinement step. This can be concluded, that it is more effective to use full multigrid approach for large number of refinement steps.

4.4   Conclusions

Numerical experiments performed gave an important conclusions on using the software tools described in Chapter 3:

- the size and the quality of the initial grid significantly affects the time and memory usage in the simulation. The coarser the grid and the better its quality, the less computer resources are used in a multigrid approach. The
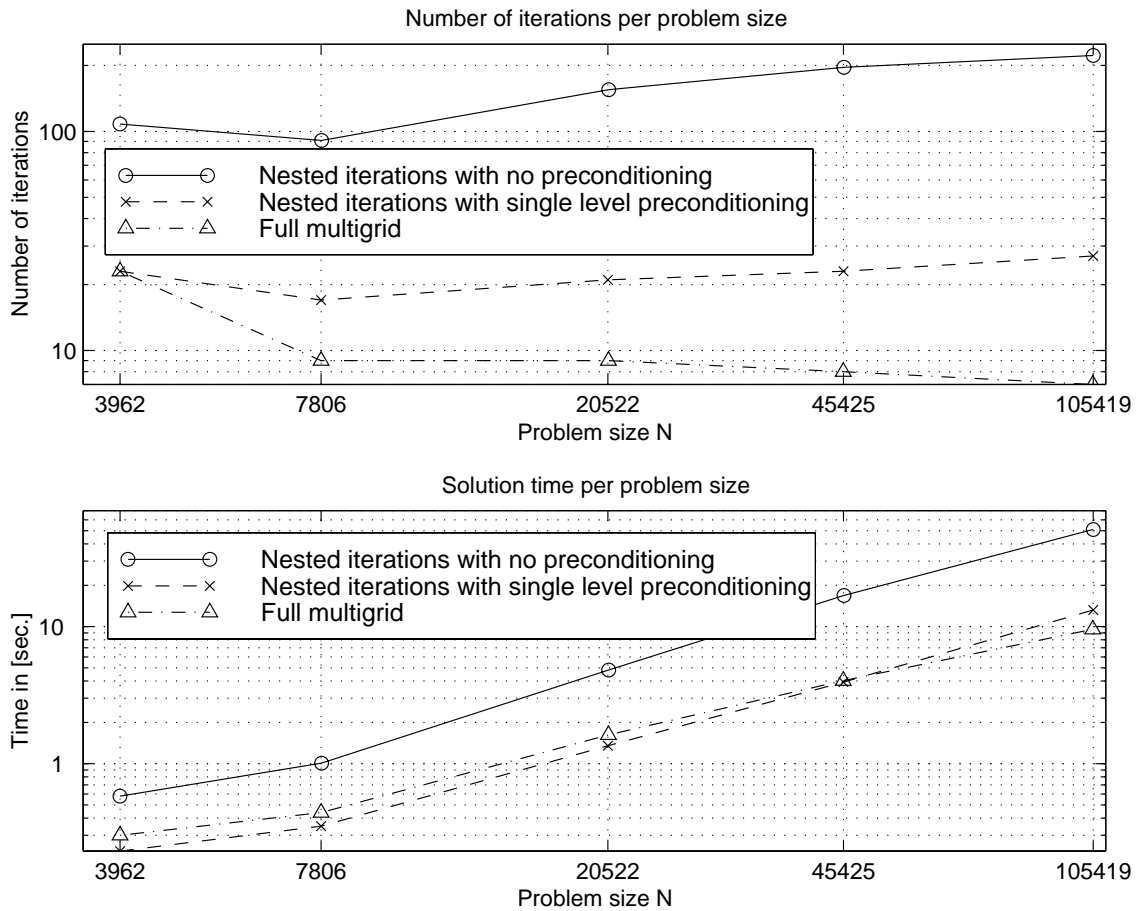
Figure 4.4: *Number of iterations (top) and solution times (bottom) per problem size (for selected refinement levels). Note the logarithmic scale*

grid resolution also influences the choice of the optimal multigrid algorithm.

- For the calculation of SAR, where gradients of the solution are sought, the use of the quadratic elements gives shorter evaluation time and more accurate results. If coarse initial grid is used, the quadratic elements also use less memory.

- For the calculation of temperature distribution, the use quadratic or linear interpolation functions seems to be very comparable concerning the usage of computer resources. It is better, however, to use quadratic elements if results are interpolated on a different final grid, as the usage of quadratic interpolation gives smoother results. If the 4–node tetrahedral grid is used, the adaptive refinement gives better interpretation of the solution.

- Adaptive grid refinement enables one to decrease the problem size and improve

the accuracy in regions of high field variations, but at the same time it is a time expensive procedure which requires additional error estimation.

- Full multigrid preconditioners present much better convergence of the solver then a single level preconditioner, but require more time per one iteration and thus it is better to use them only for large number of refinement steps

- The multigrid approach appeared to be very effective for the solution of the boundary value problem. The simplest nested iteration algorithm (as described on page 33) with additional preconditioning at each refinement step presented the shortest evaluation time for the problem at hand. The full multigrid V-cycle, although of optimal order, needed more time for the presented grid resolutions and a small number of refinement steps.

Chapter 5

Simulation results

The study, presented in previous chapters, enables one to perform simulations, which show how the temperature distribution depends on applicator excitation, volumetric blood perfusion rate and patient anatomy. A few simulations have been selected to present results, although those can be multiplied for various parameters and anatomies, using different methods of visualization. The simulations, if not spec-

Table 5.1: *Tissue parameters used in computations.*

Electric conductivity	σ	0.2455	$[S/m]$
Thermal conductivity	k	0.542	$[W/m/^oC]$
Blood density	ρ_b	1060	$[kg/m^3]$
Tissue density	ρ_t	1070	$[kg/m^3]$
Blood specific heat	c_b	3893	$[J/kg/K]$
Blood flow rate	W	7.6	$[kg/m^3/s]$
Blood temperature	T_b	37	$[^oC]$

ified otherwise, have been performed using the parameters as given in Table 5.1. The σ value has been calculated for the 500kHz frequency based on Debye dispersion model and equations presented in [34]. The rest of the parameters are according to [21]. The blood flow rate has been assumed as the highest value for the uterus malignancies (see page 19).

Section 5.1 presents the contours of SAR distributions and its corresponding temperature distributions (other examples of SAR distributions alone are presented in [85]). Section 5.2 describes temperature distributions, which are important form a clinical point of view. The influence of changes of the blood perfusion rate is presented in section 5.3 and simulations for different patient anatomies are shown in 5.4. Finally, a discussion (5.5) and conclusions close this chapter.

The figures in this Chapter have been created using the Amira visualization system developed at ZIB (http://amira.zib.de/).
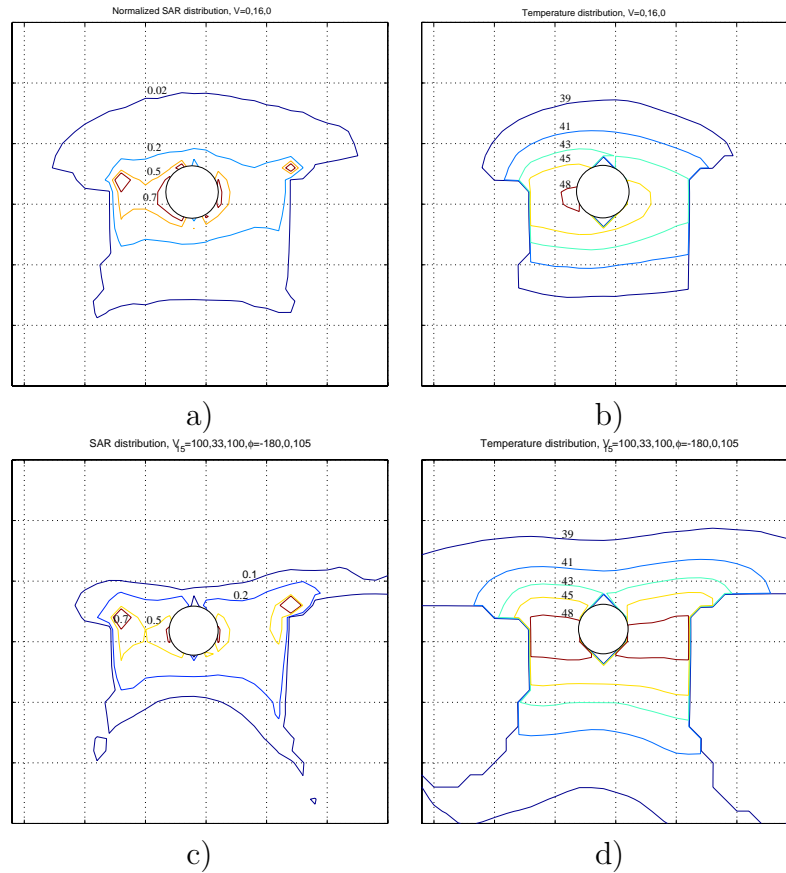
Figure 5.1: *SAR vs. temperature distribution. Cases a) and b) represent a simple excitation mode (010 - the tandem is excited, ovoids are grounded) with no phase–shifts. The power distribution is asymmetric due to the position of the ovoids. The use of a more advanced excitation ($V_{15} = 100, 33, 100$ $\phi = -180, 0, 105$) which is possible with the* HT-2 *system) enable one to set a power distribution to be more symmetric. The grid in the contour-plots is spaced by 1.5cm*

5.1   SAR and temperature distribution

Temperature pattern is obtained after the calculation of the power density (see the flow chart in Figure 3.1). Normalized SAR is equivalent to the normalized power density and represent the amount of power absorbed by tissues. The temperature distribution is associated with the power distribution by equation (2.17). The parameters, which can change temperature distribution independing on the power distribution are the blood perfusion rate and the tissue thermal conductivity (see Figures 5.5, 5.6 and 5.8).

Figure 5.1 relates the SAR distribution to temperature distribution for a selected cross–section of a domain for patient #2309 and reveals the effect of introduction

of phase–shifts on the final distributions. In Figure 5.1. The position of a tandem is marked with a circle. The ovoids are not shown, but their position is seen in Figure 5.1d, where isolines surround their shape. The cutting plane for this cross-section is selected as in Figure 5.7 (the view of this cross–section is mirrored). Note, that the 0.2 normalized SAR isoline in Figure 5.1a,c refers to the 43°C isotherm in Figure 5.1b,d. This reference can change with the variations of a blood perfusion rate. For the simulations, however, the worst–case situation has been assumed, thus even higher temperature can be obtained for this SAR level.

5.2   General patterns of temperature distribution

a)   +   b)   =   c)
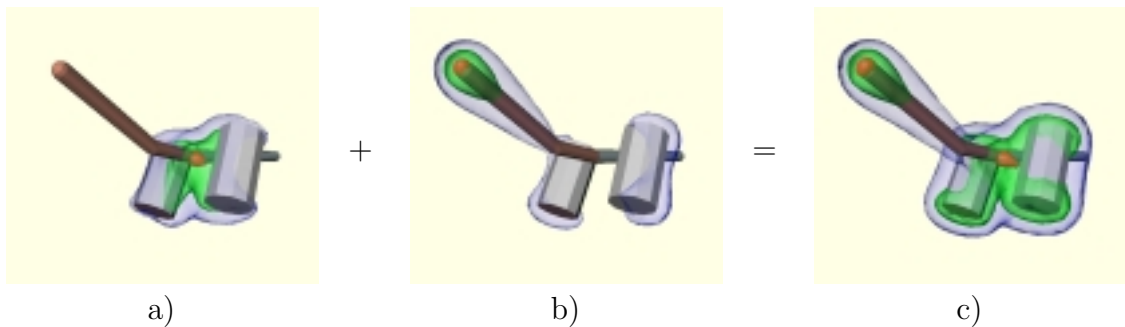
Figure 5.2: *The result of switching between two different modes. The iso surfaces of 40°C, 43°C and 47°C. a) $|V|_{15} = 100, 33, 100$ $\phi = -120, 0, 120$, b) $|V|_{23} = 100, 100, 100$ $\phi = 0, 0, 0$, c) The power of the modes a) and b) is averaged.*

Four general patterns of heat deposition are important from a clinical point of view [48]. Those depend on a tumor type and position. According to [48] the maximum power should be concentrated:

- Along the tandem for endometrial carcinomas

- Along the tandem and between ovoids, when a tumor covers also the uterine cervix

- In maximal possible volume, when tumor spreads in corpus uteri, cervix and a vaginal wall

- Asymmetrical cases of the previous case, when tumor is present in only one side of a vaginal wall

As a response to those requirements, simulation for such cases are present in Figure 5.3. These simulations have been performed for a patient #2005. The excitation of the applicator for each particular case is given in figure caption. The voltage is defined in the following way: a subscript defines the maximum voltage allowed and the numbers, separated by commas, represent an operation point (in percents) of three power amplifiers (one for each arm); ϕ represents phase–shifts for each arm. This nomenclature corresponds with a voltage control in a real system. The plots show the 42°C iso surface. Figure 5.3a shows the excitation which causes the highest temperature levels to be concentrated in distal part of the tandem. If additional phase–shift is applied, as in Figure 5.3b, the heat is additionally deposited between ovoids. Figure 5.3c represents the situation, when ovoids are not present and thus only the tandem was excited. Figure 5.3d is a result of switching between the two modes:

$$|V| \quad = \quad 100\%, 0\%, 100\%, \ \phi = -45°, 0°, 45° \tag{5.1}$$

$$|V| \quad = \quad 100\%, 88\%, 100\%, \ \phi = 0°, 0°, 0° \tag{5.2}$$

and gives the largest heated volume for this geometry. Changing the voltage amplitude in mode (5.2) to:

$$|V| = 100\%, 75\%, 68\% \tag{5.3}$$

or to:

$$|V| = 68\%, 75\%, 100\% \tag{5.4}$$

it is possible to obtain asymmetrical cases, which deposit more power at the left or right side of a patient. Those examples are presented in Figure 5.3e,f.

The switching between two different modes is a new approach, which enables one to obtain new distributions, which cannot be obtained with only a phase steering. This mechanism works in such a way, that excitation modes are interlaced with a fixed number of seconds, so that the applied power is averaged from two different distribution. Figure 5.2 present the result of switching between two different modes for a patient #2409. In this example the power in each mode is deposited in different regions, thus the maximum voltage should be increased in order to obtain therapeutic temperatures in a composite mode.

The presented simulation gives some directions to controlling the temperature patterns. Those patterns, however, change not only from patient to patient, but also change for the variations in the blood perfusion rate.
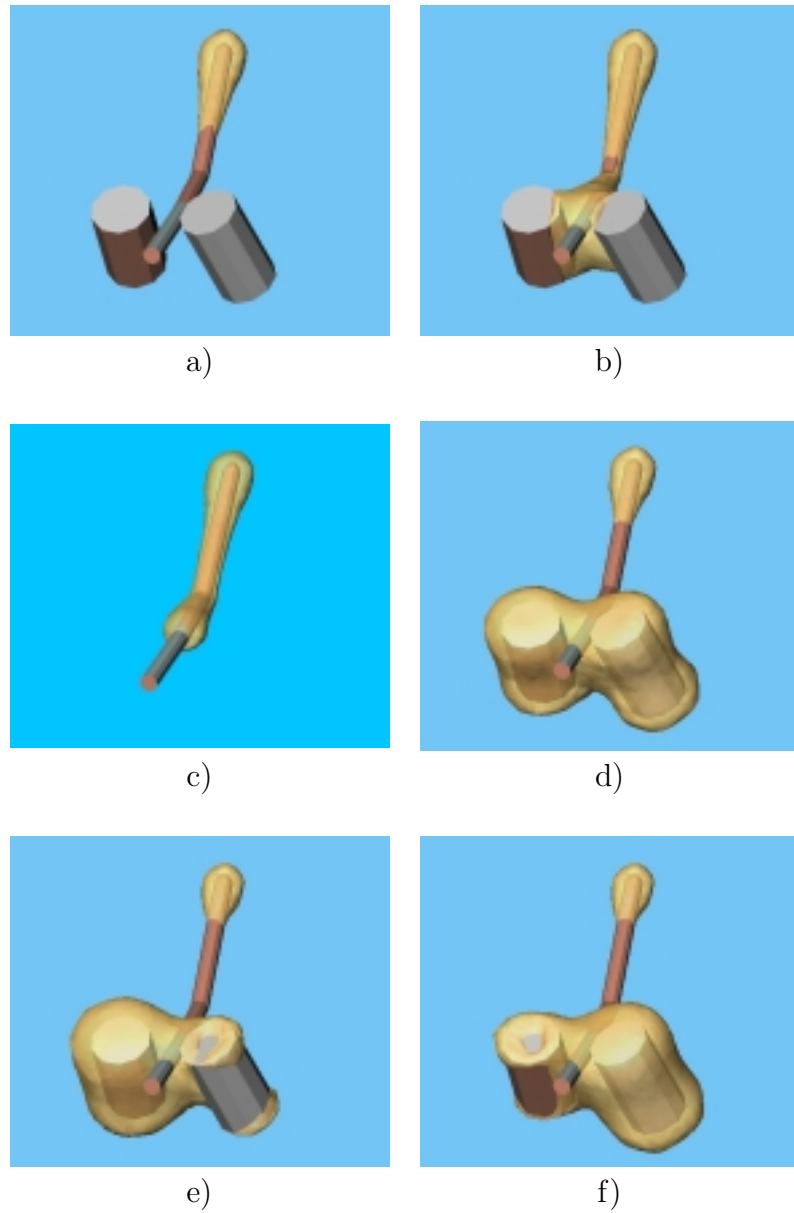
Figure 5.3: *An example of different focusing of heat by application different magnitudes and phases to the electrodes (cases a, b, c) and by application of switching between two different modes (cases d, e and f) The iso surface represent $42°C$.*
a) $|V|_{21} = 68\%, 100\%, 68\%$ $\phi = 0, 0, 0$ **b)** $|V|_{22} = 68\%, 100\%, 68\%$ $\phi = -45, 0, 45$ **c)** $|V| = 21[V]$ **d)** $|V|_{15} = 100\%, 0\%, 100\%$ $\phi = -45, 0, 45$ and $|V|_{26} = 100\%, 88\%, 100\%$ $\phi = 0, 0, 0$ **e)** $|V|_{15} = 100\%, 0\%, 100\%$ $\phi = -45, 0, 45$ and $|V|_{30} = 100\%, 75\%, 68\%$ $\phi = 0, 0, 0$ **f)** $|V|_{15} = 100\%, 0\%, 100\%$ $\phi = -45, 0, 45$ and $|V|_{30} = 68\%, 75\%, 100\%$ $\phi = 0, 0, 0$
The voltage was set at the level which would result a temperature distribution not exceeding $49°C$

a) $|V| = 8.6[V]$,   b) $|V| = 9.95[V]$,   c) $|V| = 10.85[V]$,
$W_a = 60\%W_b$ $W_b = 7.6[kg/m^3/s]$ $W_c = 140\%W_b$
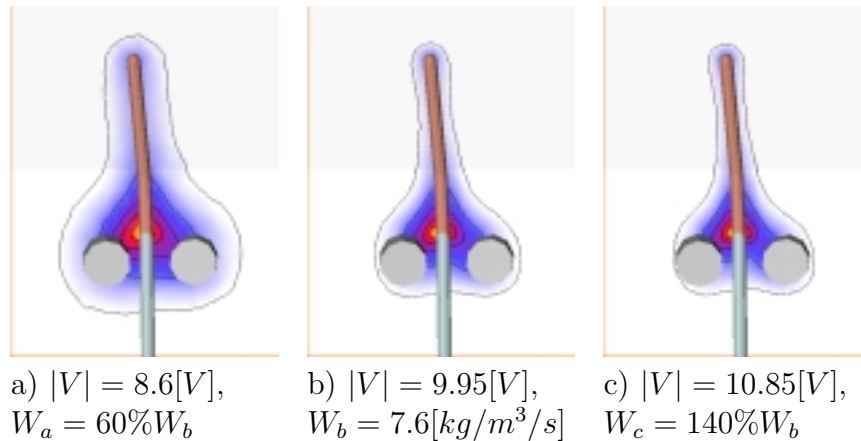
Figure 5.5: *Change of iso–terms due to a change of a volumetric blood perfusion rate. The phase shift was set to $\phi_A = -120$, $\phi_B = 0°$, and $\phi_C = 120°$. The voltage amplitude was the same for each electrode and set at the level to ensure the same maximal temperature ($T_{max} = 48.8°C$) for different perfusion. The iso lines represent 38° C 40° C 42° C 44° C and 46° C. The grid lines are spaced by 2cm.*

5.3   Simulations for different blood perfusion rates
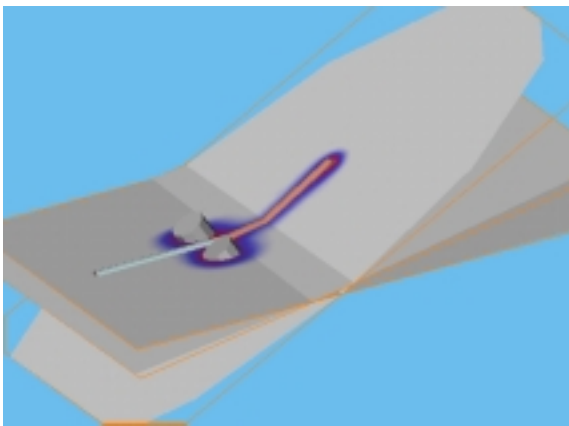
Figure 5.4: *Clipping planes for Figures 5.6 and 5.5*

Variations in blood flow can seriously change the temperature distribution. In order to illustrate this phenomenon Figure 5.6 presents iso lines and color maps for the clipping plane as seen in Figure 5.4 and for the excitation as in Figure 5.2c. The iso lines start at 38°C and are drawn every 2°C. The white color represent 38°C or less and the yellow 48°C or more. The pictures present the change of a temperature pattern if volumetric blood perfusion rate changes by ±20% and ±40%. The maximum temperature changes from 48.9°C down to 46.8°C for +40% and up to 54.1°C for −40%. Thus, care has to be taken during treatment and the maximum temperature spots have to be controlled and the maximum voltage amplitude adjusted to avoid too low or too high temperatures.

The results of the simulations where the voltage amplitude is adjusted to keep the maximum temperature at the same level is presented in Figure 5.5. As can
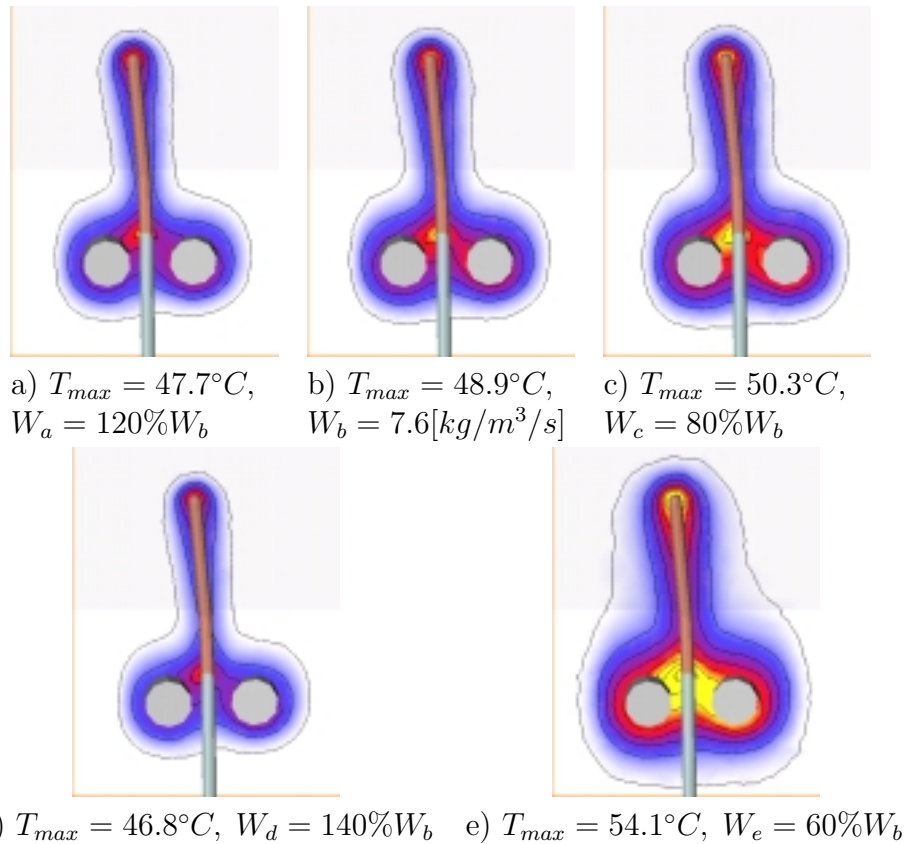
a) $T_{max} = 47.7°C$,   b) $T_{max} = 48.9°C$,   c) $T_{max} = 50.3°C$,
$W_a = 120\%W_b$ $W_b = 7.6[kg/m^3/s]$ $W_c = 80\%W_b$

d) $T_{max} = 46.8°C$, $W_d = 140\%W_b$ e) $T_{max} = 54.1°C$, $W_e = 60\%W_b$

Figure 5.6: *Temperature pattern along the tandem for the cutting planes as shown in Figure 5.4. The excitation as in Figure 5.2c. b) The volumetric blood perfusion rate increased by 20%. c) The base perfusion. d) Perfusion deceased by 20%. e) Perfusion increased by 40%. f) Perfusion deceased by 40%. The change of a maximum temperature is shown in captions.*

be expected, the heated volume shrinks if blood flow increases and spreads out if decreases. The 46°C and 48°C iso lines, however, are almost unchanged in the area of high temperature gradients. This happens because the component in the equation (2.17) associated with the thermal conductivity is still much larger than the one associated with the blood perfusion rate in this region.

5.4   Simulations for different patient anatomies

Form a therapeutic point of view it is important to understand how big differences may appear in temperature distribution for various patient anatomies. Figure 5.7 presents results for four different patient geometries with the same excitation mode and with the maximum voltage adjusted not to exceed 48°C. The pictures represent 42°C and 46°C iso surfaces and iso lines for a selected cross–section. Note, that the

shape and volume of the therapeutic temperature range vary significantly. The temperature for a selected points can change from 42°C to 48°C for the same excitation modes but different patients (compare the temperatures between tandem and right ovoid for patients #2309 and #2409). Those variations are caused by changes of:

- longitudinal position of ovoids against the tandem

- separation between ovoids

- distance between tandem and each of the ovoid

- angle between each of the ovoid and the tandem

It is evident, that the simulations should be performed for each patient separetly before the treatment starts.

a) patient #2005

b) patient #2309

c) patient #2409

d) patient #2907
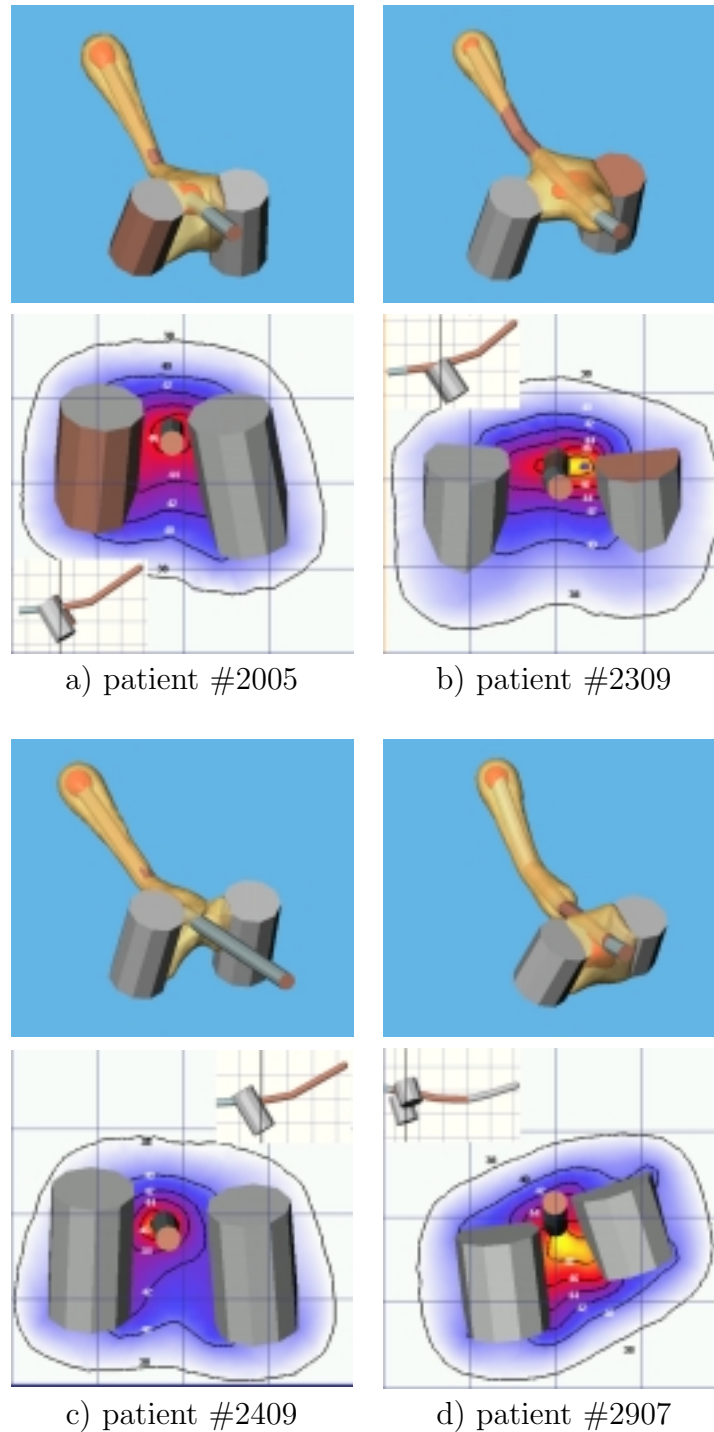
Figure 5.7: *Excitation* $|V| = 68\%, 100\%, 68\% \phi = -45, 0, 45$ *for different patient geometries. The maximal voltage amplitude was adjusted to obtain maximal temperature of about $48°C$. The iso surfaces represent $42°C$ (the outer, transparent surface) and the $46°C$ (the inner surface)*

a)   b)   c)
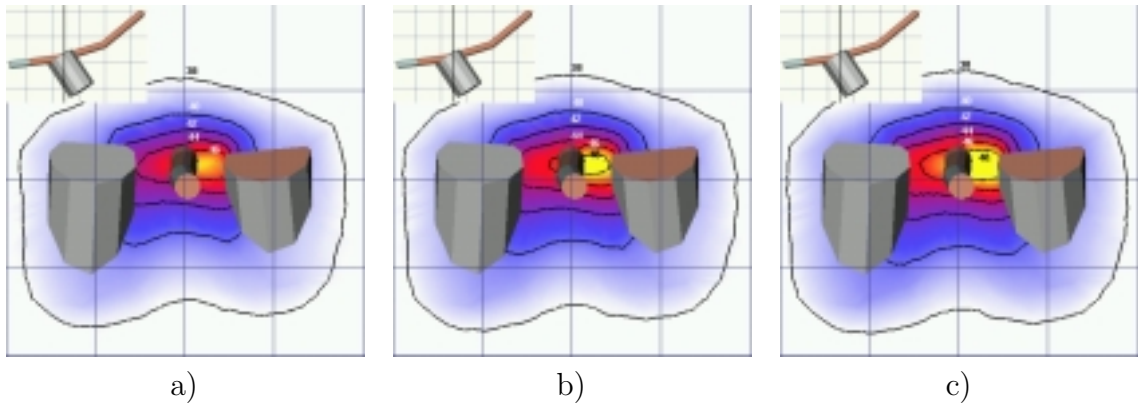
Figure 5.8: *Changes in temperature pattern due to a change in tissue conductivity:
a)* $\sigma = 0.221[S/m]$, *b)* $\sigma = 0.246[S/m]$, *c)* $\sigma = 0.270[S/m]$

5.5   Discussion

When analyzing the results, a number of possible errors have to be taken into account. One of the sources of error is associated with the fact that the computer model is assumed to be homogeneous, which does not happen in a real case. Inhomogeneities are mainly present at the ovoids, which touch a cervix from one side, vaginal wall from the second side and tampons, which prevent the applicator from moving inside vagina, from the third side. Also the tandem does not adhere to the uterus uniformly. Some bodily secretions may also be present in varying volume and may disturb the temperature pattern during treatment. Figure 5.8 presents the variations of temperature distribution with change of a conductivity of the medium by $\pm 10\%$. This example, although still for the homogeneous medium, shows how the iso lines can change if only a part of a domain has a different conductivity. The biggest changes are in the close vicinity of the applicator, where the position of the 46°C isotherm in case a) is equivalent to the 48°C isotherm in case c). However, one needs to keep in mind, that this is the region of the cervix, which is a homogeneous tissue and which, in most cases, well adjoins the applicator. Of course, larger differences in conductivity occur if air or blood are present in vicinity of the applicator. Those might be present in vagina and in a part of the uterus (see Figure 5.9). Because conductivities of blood and air ($\sigma_{blood} = 0.048[S/m]$, $\sigma_{air} = 0[S/m]$) at the frequency of 500kHz are much lower then muscle tissue conductivity ($\sigma_{muscle} = 0.2455[S/m]$), the temperatures are also lower in those regions. This improves the situation in vagina, where heating is not desired but worsens in a part of the uterus, where therapeutic temperature range may not be possible to obtain at all (see Figure 5.9).

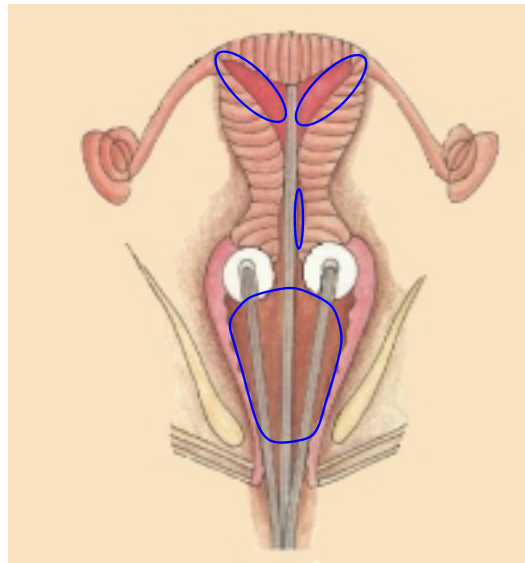The volumetric blood perfusion rate is also a problematic variable, whose changes

Figure 5.9: *The regions, where blood and air may occur are marked in blue. This picture is very simplified, as the variations in anatomy are very large. This is only a anterior–posterior drawing. In lateral cross–section the tandem adjoins the uterus in all its length.*

might be significant and difficult to predict. In simulation, the worst case value of the volumetric blood perfusion rate was taken, i.e. an upper limit of blood perfusion for cervical tumor [21] (see Table 5.1).

Another source of errors is the approximation of the applicator shape (the approximation of cylindrical shapes with right regular prisms). Simulations with different approximation of cylindrical shapes are presented in Figure 5.10. In case a) cylindrical shapes are approximated with right regular prisms with 10 walls and in case b) cylindrical shapes are approximated with right regular prisms with 14 walls (tandem) and 20 walls (ovoids). This approximation influences the grid density and a discretization error - case a) in a final grid has about 75% of the nodes of case b). It is seen that the greatest difference, reaching almost 1°C, is in a region of highest temperatures among tandem and ovoids. The total simulation time, however, increased from 4:55 min. (a) to 11:43 min. (b)

The position of the external metal foil belt may also cause some inaccuracies if not placed in a right position. Therefore, care has to be taken to place a belt in such a way, that it covers all the applicator length, i.e. that it reaches the hight of the bottom of the uterus an a patient abdomen. If, for example, the tandem tip is not surrounded by the belt, no power would be deposited in that area. Although, such a simulation has not been performed, clinical trials have confirmed such an
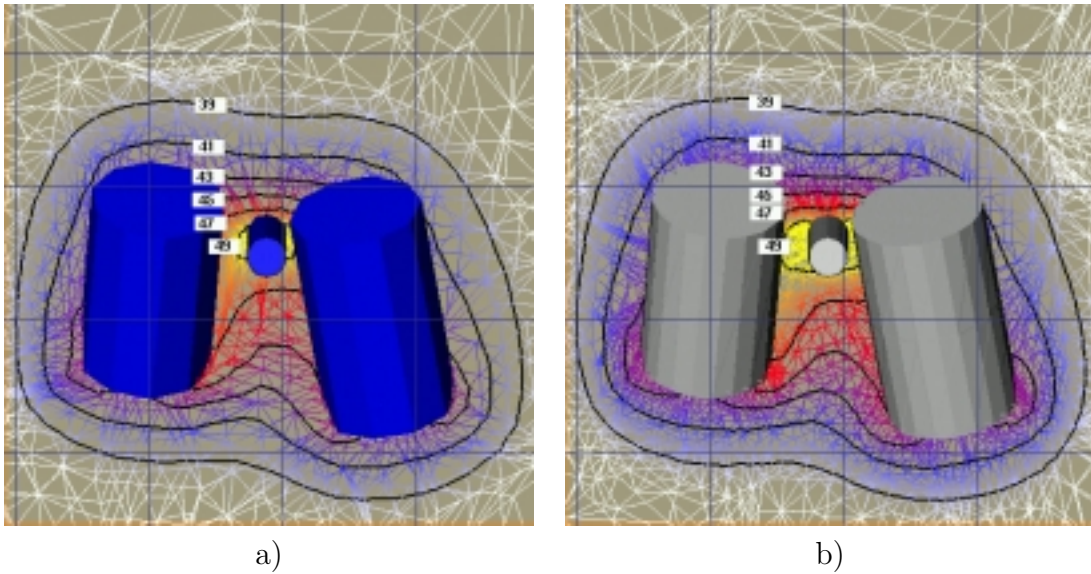
a)   b)

Figure 5.10: *An error associated with an approximation of the applicator's shape: a) cylindrical shapes are approximated with right regular prisms with 10 walls b) cylindrical shapes are approximated with right regular prisms with 14 walls (tandem) and 20 walls (ovoids).*

observation.

5.6   Conclusions

Simulation results presented in this chapter show the possibilities of excitation of the applicator and a resulting temperature distributions. Although the simulation is only an approximation of the solution obtained in a computer model, it gives an important directions on controlling the hyperthermia treatment:

- It is possible to use excitations described in section 5.2 as reference, but the applied maximum voltage has to be adjusted as not to exceed safe temperatures. The temperatures have to be measured during the treatment.

- The temperature measurement points should be determined from the simulation and the catheters with thermocouples should be placed accordingly to results obtained in the simulation.

- Some corrections of the amplitudes and phases can be introduced after the simulation is performed in order to obtain the most desirable temperature distribution.

- There is an error associated with inhomogeneities of the medium. The small changes are associated with inhomogeneities between cancer and healthy tissues - cancer tissue usually has lower blood perfusion rate, which maximizes the temperature within tumor. More significant changes may occur in regions where muscle tissue does not adhere the applicator. In those areas the temperature is lower than resulting from the simulation.

Unfortunately, during a real treatment, it is not possible to verify the obtained temperature patterns with good resolution and accuracy due to a lack of a good method of temperature mapping within human tissue. Only a qualitative check is possible by introducing catheters within a patient and performing a temperature mapping with a thermo-couple. Such results for the first clinical trials are presented in Chapter 8. Also the experiments with the use of solid and liquid phantoms have been performed in order to have a validation of the applied solution method. The results of those experiments are presented in Chapter 7.

Chapter 6

The hyperthermia systems

The very first experiments, whose purpose was to assess the possibility of using the Fletcher–Suit applicator in hyperthermia have been performed using a single channel system prototype *HT-1*, described in Section 6.1. Results of those experiments are presented in Section 8.1. After the simulation software has been developed the simulations have shown, that much better control of the temperature pattern can be obtained for a three channel system with the adjustment of phase-shift among channels and with the possibility of time-switching between two different modes (see Chapter 5). As a result the new hyperthermia system has been developed, which is described in Section 6.2.

The electronic circuits of both systems were designed and whole systems assembled by dr W. Szkudliński. The control software was developed by M. Szkudliński. The author took part in the overall system design, supervised the construction and carried out the pre–clinical tests.

6.1 The system prototype *HT-1*

The prototype of the 500 kHz LCF hyperthermia system which has been used in laboratory studies and in a phase I clinical trial is shown in Fig. 6.1. The system includes the transmitting part consisting of a generator, control attenuator and a power amplifier. The receiving part of the apparatus contains operation amplifiers and the system control part with AD card and a computer. The thin metal foil belt around a patient serves as an external electrode (which is grounded). The system is capable of measuring the power delivered to a patient, the patient's body impedance and the temperature. The power is controlled by means of the control attenuator. The system is also equipped with a set of alarms to warn the operator to switch the power off when the critical values of temperature, power or electrical current are exceeded. As only one control attenuator is included in transmitting part, only the
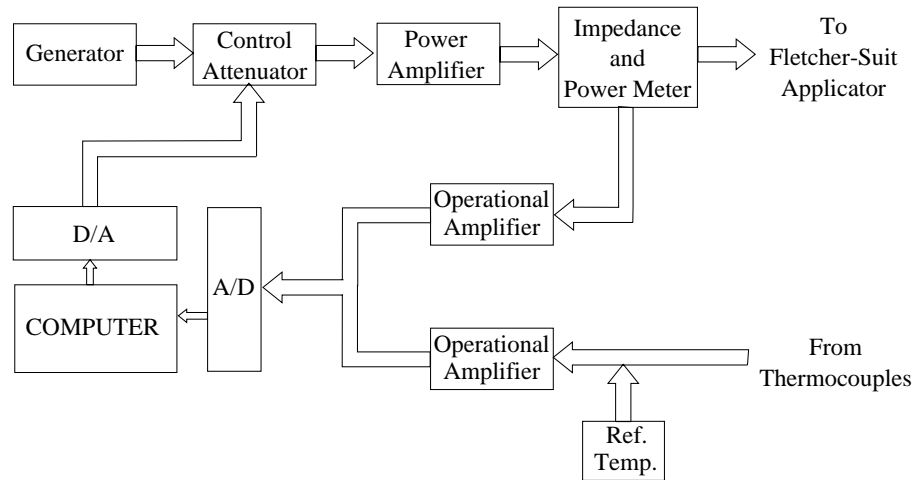
Figure 6.1: *Block diagram of the system prototype*

basic excitations are possible – each of the electrode can be independently excited or grounded (switched on or off), and the voltage amplitude has to be the same on all the electrodes, which are switched on (this corresponds to in–phase steering).

6.2   The new hyperthermia system *HT-2*

The new system was developed, based on the conclusions reached after first clinical trials and a series of numerical simulations. It consists of three coherent channels, whose phase–shift can be adjusted with a 22.5° step and the voltage can be independently controlled by means of three power amplifiers. The voltage amplitude is constantly measured at the output and kept at specified level independently on the load. In the current version of the system the phase measurements have not been supplied and thus the device has to be calibrated for each patient. This is because the phase–shift depends on a patient's body impedance. The software control enables switching between two different excitation modes (i.e. one excitation mode is set and then the system switches to another mode after a fixed number of seconds). The system of temperature measurement consists of three thermocouples attached to the reference junction kept in constant temperature of 55°C. The system measures temperature in the range of 30°C to 50°C with accuracy of 0.1°C. For temperature measurements the power is switched off for $20\mu s$ every second in order to eliminate possible interferences with the 500kHz signal (which is at a high power level). A care was taken to provide the security to a patient. The system has been supplied with the separating transformer, which separates the system from the mains and with a set of alarms, which warn the operator (or even switch off the system) if any
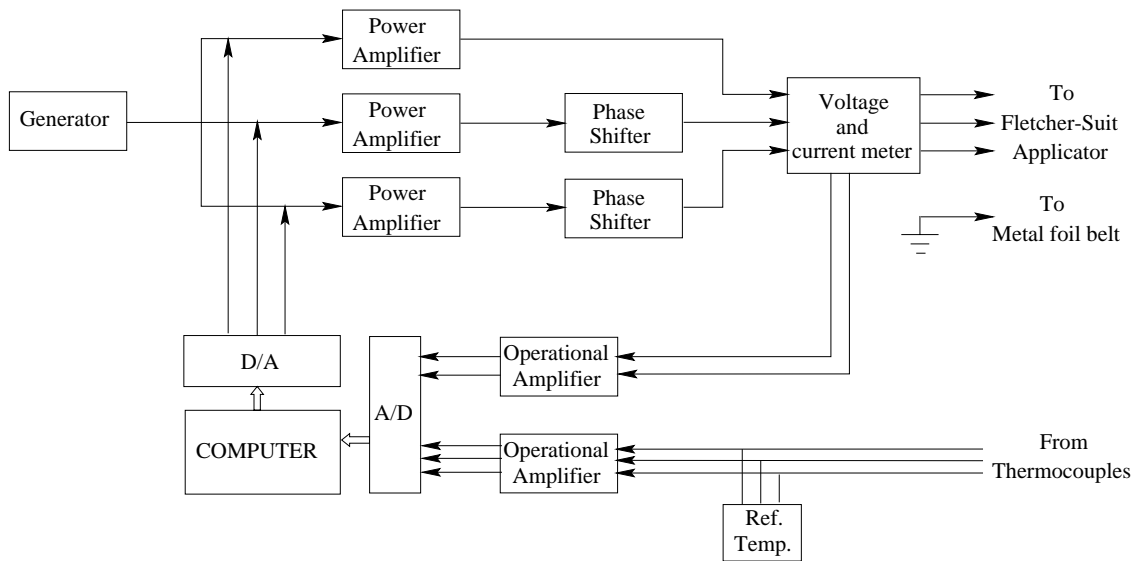
Figure 6.2: *The block diagram of the HT-2 hyperthermia system*

of the parameter exceeds its acceptable value. The block diagram of the system is presented in Figure 6.2. It consists of:

- ▶ 500kHz generator,
- ▶ 3 power amplifiers,
- ▶ 2 phase-shifters,
- ▶ system for measurement of output current and voltage amplitudes,
- ▶ system for temperature measurements,
- ▶ three thermocouples connected to a single reference junction,
- ▶ three output connectors for three applicator's arms,
- ▶ grounded output connector for metal foil belt,
- ▶ A/D – D/A card,
- ▶ PC computer,
- ▶ software.

The *HT-2* system is mounted on a cart. This enables one to move the system to the room, where the brachytherapy treatment is performed afterwards. After the system is detached from a patient, the brachytherapy can immediately be applied. The view of the system is presented in Figure 6.3. After the hyperthermia treatment has been completed, the system is detached from the patient. The FSA is

Figure 6.3: *View of the* HT-2 *hyperthermia system*

retained in patient's body and its arms are loaded with radioactive pellets essential in brachytherapy.

Chapter 7

Phantom experiments

Phantom experiments are a very important step in verification of the both, the device and the simulation. This chapter describes experiments performed with the *HT-2* device (as described in previous chapter) on liquid and solid phantoms and compares obtained results with the computer simulation. In a liquid phantom a probe measures the voltage distribution, while in a solid phantom a thermo-vision camera takes a picture of temperature distribution which, depending on a technique used, may represent a power or a steady state temperature distribution.

7.1 Voltage distribution in liquid phantom

This experiment was performed in order to verify the *HT-2* device and to see how the excitation of the electrodes affects the voltage distribution. Three brass bars were used instead of the applicator in this experiment. This enabled setting larger distances among electrodes and to checking the voltage distribution among them. Larger distances also decreased the error associated with the field distortion due to a presence of a measurement probe.

The setup. The system has been verified in a 0.9%NaCl water solution in a setup as presented in Figure 7.1. The brass bars were fixed at the vertices of the equilateral triangle of the edge of 8cm. The diameter of the bars was 6mm. The outer electrode ($\phi = 29$)cm was made of the same material as the bars so as order to prevent undesired electro-chemical processes in the solution. The construction of a voltage probe was a result of considerations and experiments, which were focused on minimization of the influence of the probe on the voltage distribution. The first experiments displayed, that some capacitances occur if a regular coaxial cable is used. A voltage probe was constructed in the way that any possible capacitances that could appear between the coaxial cable and the solution were minimized. To
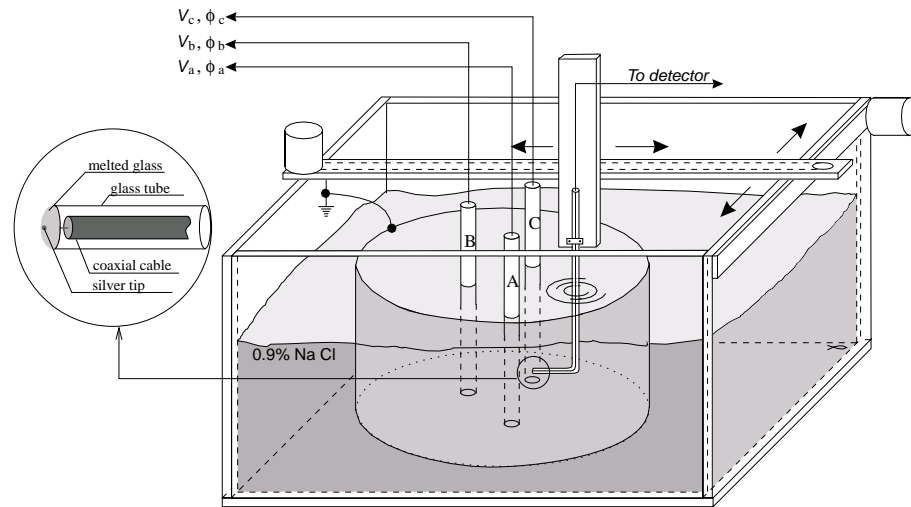
Figure 7.1: *The measurement setup used for the measurements of the voltage distribution*

this end the coaxial cable was inserted into a bent glass tube. The bend was necessary in order to prevent the possible capacitances between the electrodes and the probe. The glass tube was melted at the end in order to prevent possible water penetration. The actual measurement probe extending out of the tube was the end of a silver wire attached to the coaxial cable.

The measurements. The electrodes were attached to the channels of the *HT-2* system. The signal from the probe was detected in an oscilloscope, where the root mean square voltage V_{rms} was read. Each reading was a result of 64 averaged samples. The probe motion was controlled by a stepping motor with a step resolution of 0.5mm in each direction. Four configurations have been tested:

1. Electrode **B** was excited and the electrodes **A** and **C** were grounded, no phase shift was applied. The probe was moving along the symmetry axis away from the electrode **B** at a distance of 7cm (compare Fig 7.2b).

2. All the electrodes were excited with the same voltage, no phase shift was applied, the probe movement as in previous configuration.

3. All the electrodes were excited with the same voltage. The phase shift $\phi = -112.5°$ was applied to the electrode **A** and the phase shift $\phi = 112.5°$ was applied to the electrode **C**. The electrode **B** had $\phi = 0°$. The probe movement as in configuration 1.
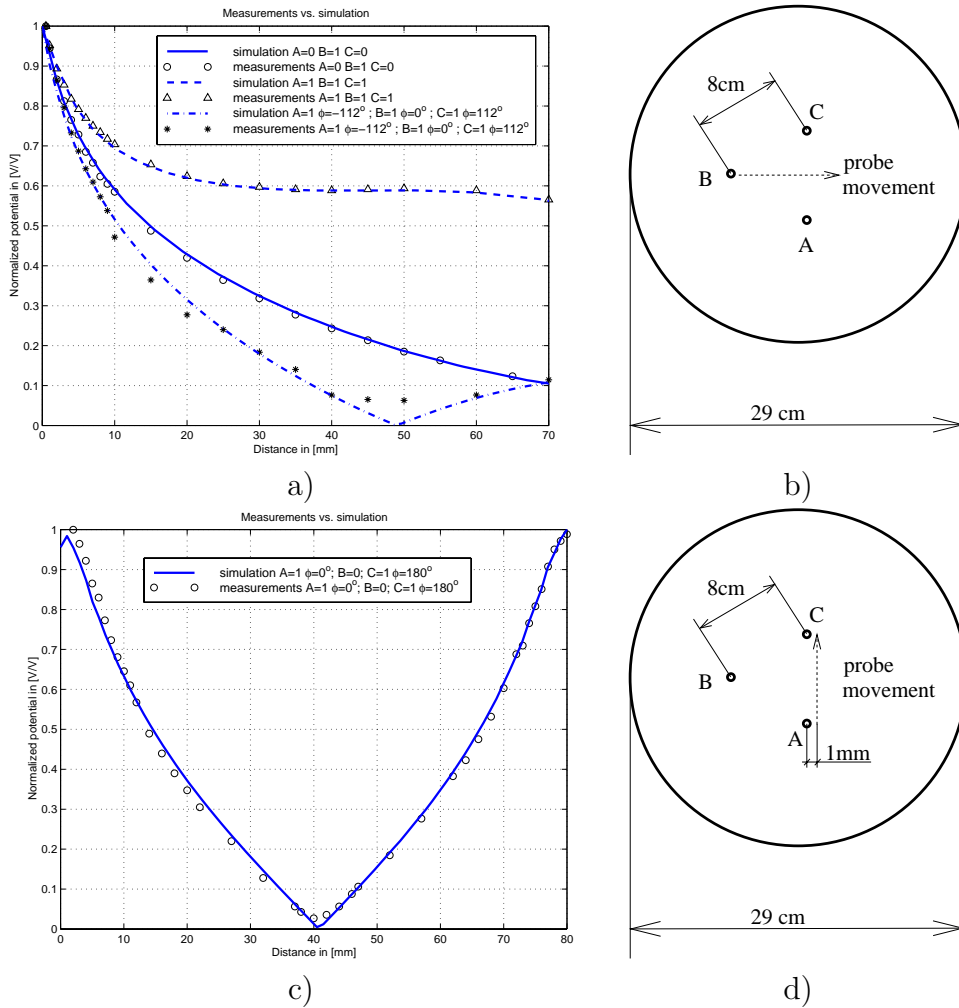
Figure 7.2: *Verification of the hyperthermia system device.*

4. Electrodes **A** and **C** were excited with opposite phase shifts and the electrode
   B was grounded. The probe was moving parallel to the line segment $\overline{AC}$ 1mm
   from the surface of the electrodes (compare Fig 7.2d).

Measurement verification   The simulation has been performed using 2D finite–
elements and using preconditioned conjugate gradient solver. Appropriate boundary
conditions have been applied on boundaries. The mesh is presented in Figure 7.3.
The lines in the figure represent the cutting planes taken for the chart in Figures 7.2a
and 7.2b.

The results.   Four configurations of the electrode excitations have been tested
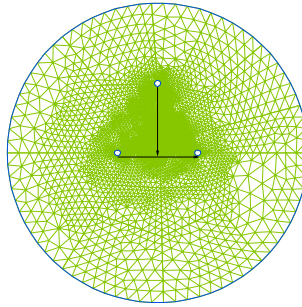and Figure 7.2 presents the results, verification with the computer simulation and

Figure 7.3: *View of the mesh used for the simulation. The black lines represent the cutting planes for the charts.*

the schematics of the probe movement (Fig.7.2b,d). In Figure 7.2a,b, the lines represent the results obtained in computer simulation, while the marks represent the measurements. For the cases where no phase–shift was applied (circles and triangles in Fig. 7.2a), the agreement between simulation and measurement is excellent. The phase–shift of 112° and 180° (stars in Fig. 7.2a and circles in Fig. 7.2c) showed the minimum to be shallower then in the simulation. This may indicate, that the actual phase–shift was different that the one set in the device.

7.2   Temperature and SAR distribution measurements with a thermo-vision camera

A thermo–vision camera was used for experiments with the solid phantoms. Two approaches were applied. The first, called *T-rise* method was used for the determination of the SAR pattern. The second approach was used to determine a steady state temperature distributions. In order to explain this one needs to refer to the bio–heat transfer equation (2.16). In a solid phantom there is no perfusion and thus, before the power is delivered (when $P = 0$), the temperature field fulfills Laplace's equation according to fixed boundary conditions:

$$\nabla \cdot (k \nabla T) = 0 \tag{7.1}$$

The moment when the power is switched on, the component associated with the temperature change appears in order to balance delivered power:

$$\rho c \frac{\partial T}{\partial t} = P \tag{7.2}$$

The temperature change results in a gradient change due to the presence of thermal conductivity and thus the next component appears:

$$\rho c \frac{\partial T}{\partial t} = \nabla \cdot (k \nabla T) + P \tag{7.3}$$

After a long enough time period we again get a steady state and the left side of the equation (7.3) disappears forming the Poisson equation:

$$-\nabla \cdot (k \nabla T) = P \tag{7.4}$$

From the above equations, the method of measurement of the power and temperature distributions with a thermo-vision camera can be found.

SAR distribution   Equation (7.2) states, that the power distribution is proportional to the change of the phantom temperature immediately after the power is switched on. Thus, the measurement precision depends on the time spent between the moment the power is switched on and the moment the picture is taken, as well as on the thermal conductivity of the medium. The smaller the thermal conductivity and the shorter the time between the power switch on and picture capture, the smaller is the error. Nonetheless, the heating time should be long enough in order to obtain the temperature exceeding the sensitivity threshold of the camera. The following measurement procedure has been assumed:

1. Capture the temperature distribution of the phantom in a steady state before the power is switched on

2. Switch on the power at the highest possible level for a time period enabling the temperature change above the sensitivity threshold of the camera.

3. Switch the power off, prepare the phantom to make a picture with a thermo–vision camera (move out the electrodes, move out a part of the phantom – see Figure 7.4 and capture the resulting temperature distribution.

4. Subtract the temperature distribution obtained in step 1 from the one obtained in step 3 and normalize. The resulting distribution is proportional to the normalized power.

Temperature distribution   The steady state temperature distribution can be measured, when the heating time enables the thermal conductivity to fully balance delivered power as in equation (7.4). Thus, the following measurement procedure has been assumed:

1. Switch the power on a very low level for a very long time period

2. Switch the power off and immediately capture a temperature distribution

7.2.1   Phantom fabrication and measurement setup

In the experiment the power from the *HT-2* device is delivered to a solid state phantom, causing the temperature to rise. The true temperature distribution is obtained inside the phantom, which should be cut and put together in such a way as to enable the access inside of the phantom after the heating. The temperature distribution is captured immediately after removing a part of the phantom. The phantom conductivity should enable one to load the device with the similar impedance to the one which can be obtained in living tissue. The exact value of the conductivity is not important in a homogeneous medium, as it can be normalized. The phantom should also remain solid when the temperature is raised to 60°C

One material, commonly used for this kind of experiments is gelatine, which can easily be formed and cut according to the needs. After forming and cutting, the gelatine is tanned in order to move the melting point above 60°C. Tanning was performed in a di-Sodium tetraborate and formaldehyde solution for 48 hours. The final recipe, based on [49], was obtained after a number of experiments with different ratios of water and gelatine and with different time period of bath in a tanning liquid. The recipe is presented in Table 7.1 and the procedure is as follows:

1. Add gelatine to hot, salted water and stir until solved

2. Pour the solution into a prepared dish and wait until the solution thickens

3. Grease the electrodes, put into the thickened solution and fix the position

4. Wait until the gelatine becomes solid

5. Carefully remove the electrodes (greased metal electrodes remove smoothly)

6. Put the dish into hot water and remove the phantom from the dish

7. Put the gelatine into prepared tanning liquid. The tanning time should depend on the phantom volume. The larger the phantom, the longer is the tanning time.

8. Put the phantom into water for a few minutes to rinse it from the tanning liquid

Phantom obtained according to the above procedure is hard, fragile and slippery. It may break apart if dropped (similar to tempered glass), thus care has to be taken when inserting and removing the electrodes or manipulating the phantom. Measured conductivity $\sigma = 0.556[S/m]$.

Table 7.1: *Recipe for the phantom preparation*

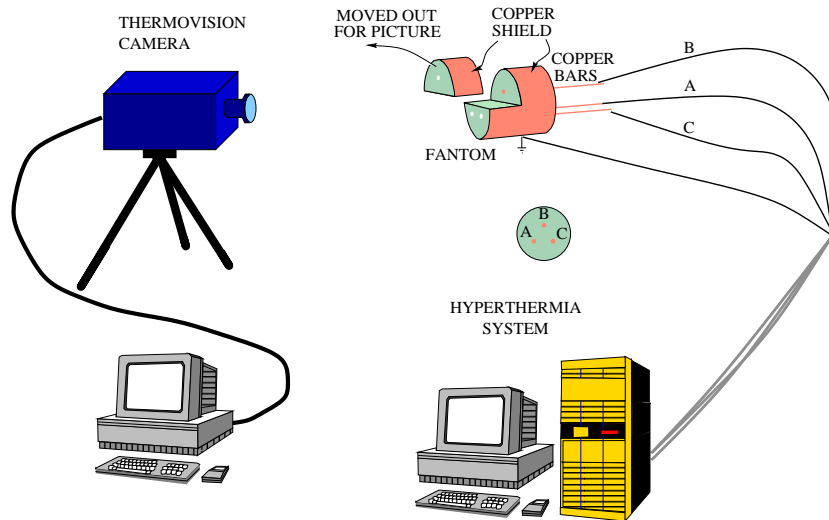| Phantom	
gelatine	200 g
water	1000 g
salt	1.0 g
Tanning	
di-Sodium tetraborate ($Na_2B_4O_7 \cdot 10H_2O$)	20 g
formaldehyde pure ($HCHO$)	5 g
water	ad. 1000 g
bath for 48 hours	

Figure 7.4: *Measurement with a thermo-vision camera*

The measurement setup is presented in Figure 7.4. Three metal bars have been used as electrodes instead of the applicator in order to simplify the cutting of the phantom. The applicator shape would not allow one to remove the electrodes for the picture capture.

7.2.2   Measurement and simulation

In this section the results of the measurements of the SAR and temperature distribution patterns are presented. The measurement results are compared with the patterns obtained in computer simulations.

7.2.2.1   SAR patterns

Figure 7.5 presents a comparison between normalized SAR isolines obtained in simulation and normalized ΔT isolines obtained from a thermo-vision camera. Normalized distributions of ΔT and SAR should agree if the equation (7.2) is fulfilled, i.e. if the time between the power switch on and measurement is so short, that the thermal conductivity does not change the equation (7.2) into (7.3). Four measurements are presented in Figure 7.5a-d. The upper picture refers to the measurements and the lower to simulations. Heating periods were set to different values in order find out the minimum time required to obtain satisfactory temperature resolution. The time between the power switch off and picture capture resulted from all the arrangements necessary for this operation (uncovering the phantom and removing the bars – see Figure 7.4). The power was set to the maximum power level with the voltage magnitude $|V| = 60[V]$.

The contour plots in Figure 7.5 present a general agreement between the simulation and experiment and show the effect of focusing the power in different regions, depending on the phase–shift.

However, the experiment results revealed, that even the shortest heating time with the time required for picture capture (Figure 7.5a, 35 s. in total) was long enough for the thermal conductivity of the copper bars and a heat transfer coefficient of the gelatine to move the maximum (0.95 isoline) away from the electrodes and to spread out the rest of the isolines. There is also another possible reason of disagreement between the measurements and the simulated normalized SAR distribution. Very high gradients, which occur at the surface of the electrodes destroy the initial power distribution.

7.2.2.2   Temperature patterns

The measurement system was set up as presented in Figure 7.4. The system has been supplied for 2 hours at 2–watt power level with voltage amplitudes and phases as specified in the figure caption. The picture of the temperature distribution has been taken within 25 seconds after the power was switched off. The resulting temperature distribution is presented in Figure 7.6a, which can be compared with the simulation results presented in Figure 7.6b,c.

Simulation parameters are given in the figure caption. The boundary at all the electrodes were set as Dirichlet BC with the temperature resulting from the measurement. Comparison of pictures 7.6a and 7.6b shows, that the area of the maximum temperature is larger in the simulation. The explanation comes from the picture 7.6c, where phase difference among electrodes were decreased in the simulation. This arrangement resulted in an excellent agreement between the simulation and
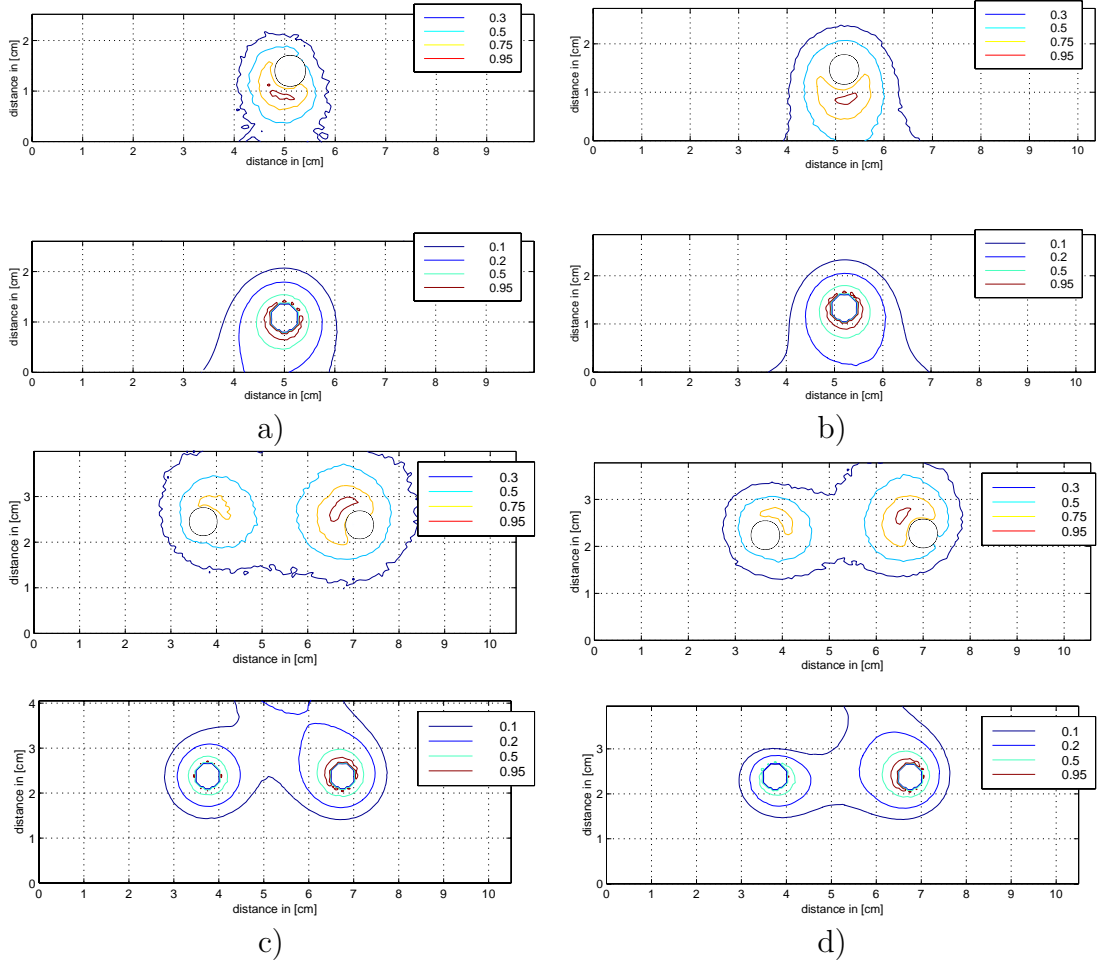
Figure 7.5: *Measurement of SAR distribution with a thermo-vision camera. The upper row presents measurements and the lower simulations. Subscripts* a, b *and* c *refer to the copper bars described in Figure 7.4. a) Heating time 20 s. Picture captured after 15 s.* $V_a = V_b = V_c = 60[V], \phi_a = 90°, \phi_b = -90°, \phi_c = 0°$; b) Heating time 40 s. Picture captured after 15 s. $V_a = V_b = V_c = 60[V], \phi_a = 0°, \phi_b = -90°, \phi_c = 90°$; c) Heating time 60 s., Picture captured after 13 s. $V_a = V_b = V_c = 60[V], \phi_a = 0°, \phi_b = 112°, \phi_c = -112°$, d) Heating time 60 s., Picture captured after 11 s. $V_a = V_b = V_c = 60[V], \phi_a = 90°, \phi_b = 90°, \phi_c = -90°$*

measurement. This might be concluded that the phase–shift among electrodes, although properly set in the device, resulted in different phase–shift among electrodes. The reason is, that the device has not been supplied with the phase measurement system (in order to reduce the costs), which would adjust phase-shifts according to the patient's body impedance. In the current system, however, the problem can be solved by a system calibration (by measurements of a patient's body impedance) and a phase-correction using a procedure described in Appendix C.
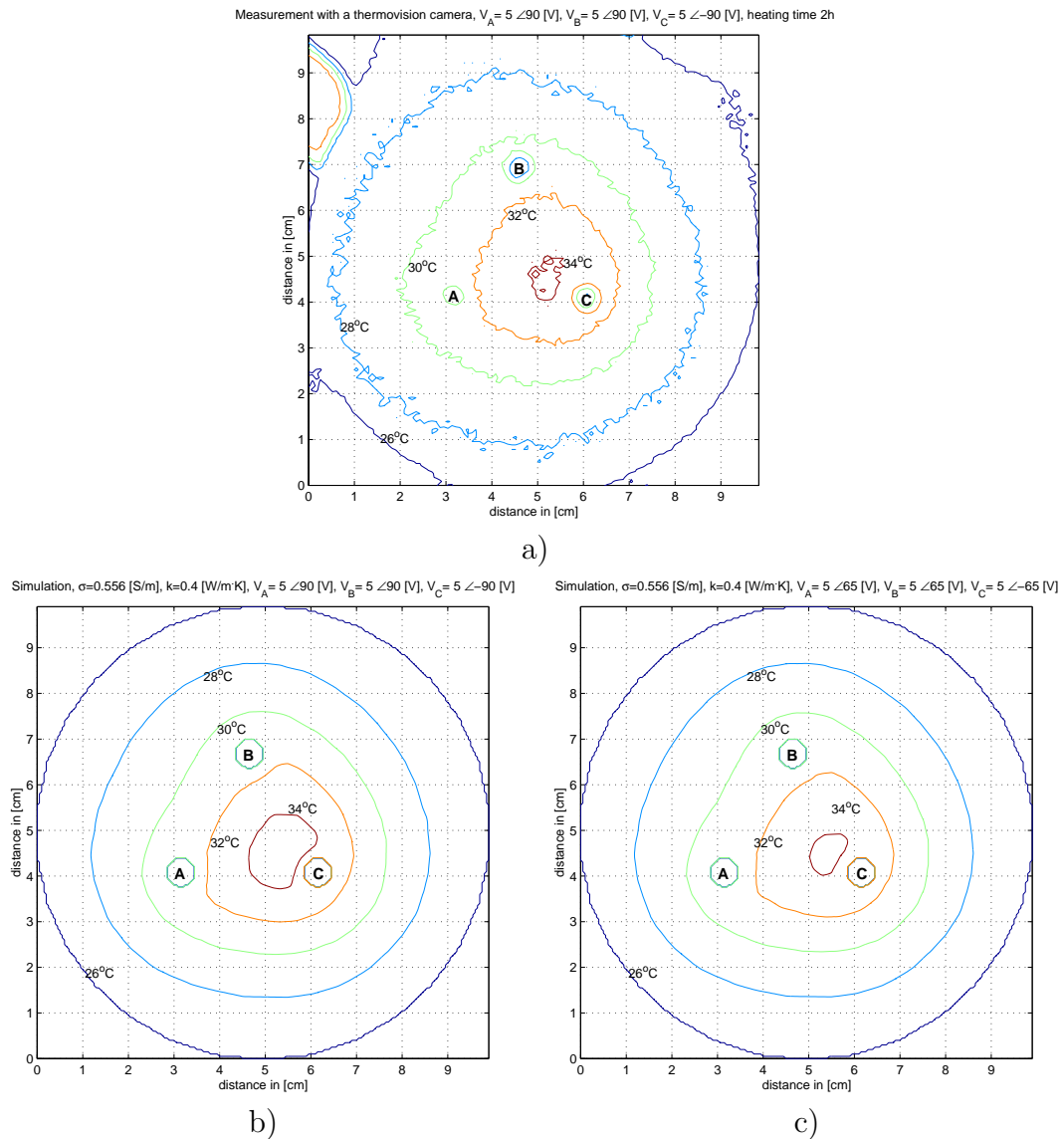
Figure 7.6: *a) Measurement of a steady state temperature distribution with a thermovision camera. Subscripts* A, B *and* C *refer to the copper bars described in Figure 7.4. The electrodes were supplied with the following voltage:* $V_A = 5e^{j90°}[V]$, $V_B = 5e^{j90°}[V]$, $V_C = 5e^{-j90}[V]$ *for two hours. Picture was captured 25 s. after the power switch off. Distortions in the upper left corner and at the top of the picture are due to the fingers which were kept on the phantom, when the picture was taken b) Simulation of the temperature distribution with the KASKADE system with the same voltage as in measurement and with* $\sigma = 0.556[S/m]$ *and* $k = 0.45[W/m \cdot K]$ *c) Simulation with the corrected phases. Parameters as in previous case except for the phases, which were set as* $V_A = 5e^{j65}[V]$, $V_B = 5e^{j65}[V]$, $V_C = 5e^{-j65}[V]$

7.3   Conclusions

The performed experiments have verified the both, the *HT-2* system and the simulation software. Measurements in a liquid phantom have verified the voltage distribution. The verification of the SAR pattern based on T-rise method have practically failed, because of too high thermal conductivity of the phantom. However, a qualitative agreement has been obtained. The picture of the temperature distribution agreed very well with the distribution obtained from the simulation, but has shown that the phase–shift requires additional calibration for every change of the load (i.e. for each patient) and that the next version of the system should be equipped with the on–line phase measurement and phase correction system. Also, during the experiments, the security of the *HT-2* device has been verified and all the alarm signals have been checked before further evaluation to the clinical trials.

Chapter 8

Clinical Tests

Some preliminary clinical trials with the system prototype *HT-1* and then with the new hyperthermia system *HT-2*, (both described in Chapter 6) have been performed in the Center of Oncology, Warsaw. The treatments with the system prototype have given an important directions on the construction of the next device. During these trials the interstitial temperature measurements have shown that it is possible to obtain therapeutic temperatures using this method. Results of those measurements are presented in Section 8.1 and are compared with computer simulations. The trials with the *HT-2* device are described in Section 8.2. Unfortunately, the treatments with the new device did not give as much information concerning temperature distribution as treatments performed with the previous device. The reason for this is that the interstitial placement of catheters requires the patient's agreement and this was not obtained in the latter case. Thus the temperatures were measured inside the tandem and ovoid tubes.

Statistical data, which would confirm the medical effectiveness of the approach require additional few years, but this goes beyond the scope of this work.

8.1 Treatment performed with the *HT-1* system prototype

Before each treatment thermo-probe catheters (with markers inside) were placed intracavitary and/or interstitially (depending on patient's agreement) and a set of radio–graphs (A–P, and Lateral) was prepared in order to obtain exact Fletcher applicator and catheter positions. During treatments thermo–couples were placed in a catheter in such position that the highest temperature along catheter was measured. Temperature mapping along catheters was performed once or twice during treatment. The excitation, which resulted in a largest heated volume was chosen: the voltage was applied to the central arm, while applicator ovoids and a metal foil
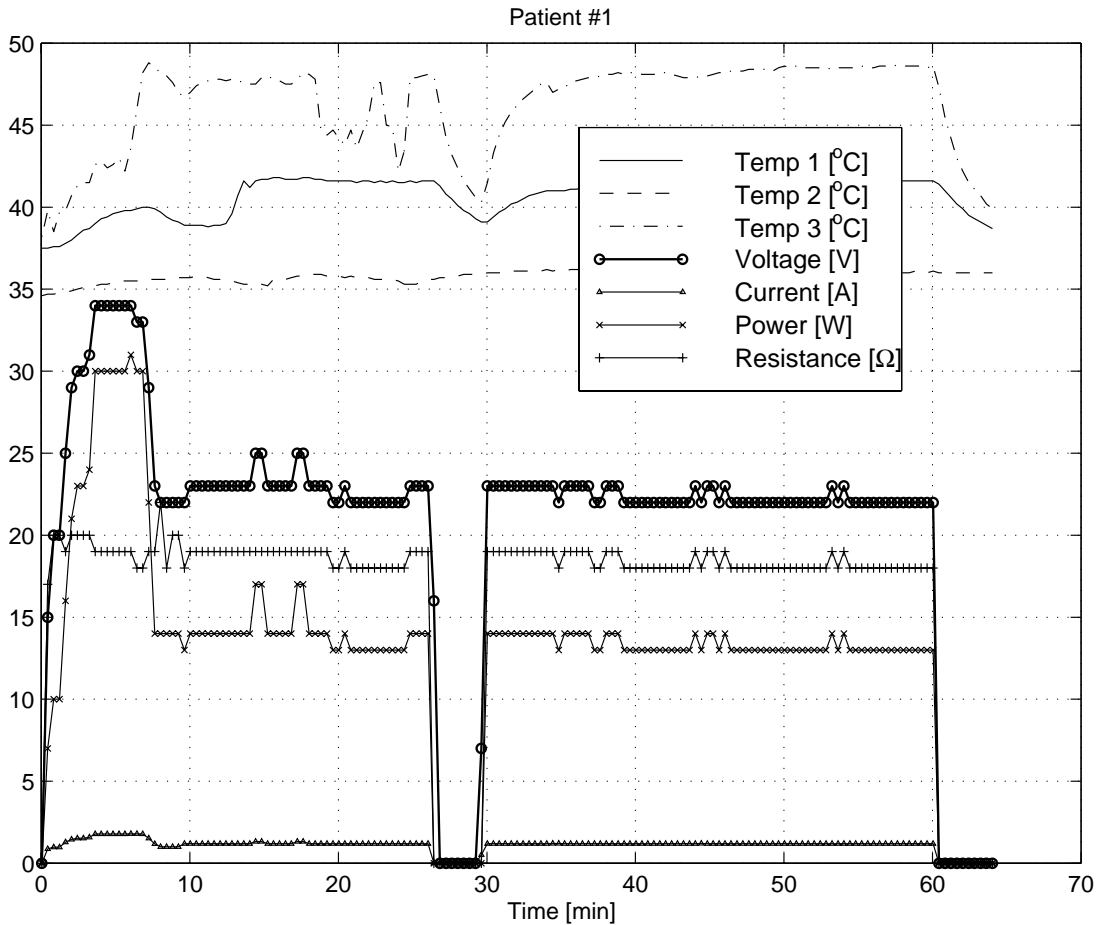
Figure 8.1: *A chart of a clinical trial for a patient #2409. Thermo-probes were placed as follows:* Temp 3 *on the tandem surface at the point of the maximum temperature, which was found to be at the height of the colpostats (the probe was mapped along the tandem in order to find the peak);* Temp 1 *15 mm to the top–left of a patient from* Temp 3*;* Temp 2 *was placed in vagina, where heating was suppressed by the presence of insulating paint. Temperature variations of* Temp 3 *between 15 min. and 25 min. are due to the movement of the thermo-probe along the tandem.*

around a patient were grounded (in the system prototype there was only one output channel, thus no phase–shift nor different amplitudes were possible). The plot of the parameters obtained during treatment is presented in Fig. 8.1

The intention was to obtain temperature measurements in one catheter attached to the tandem and in two catheters placed interstitially and/or intracavitary. Each treatment description includes a figure, which contains position of central arm axis, ovoids' axes, thermo-probe catheters, position of a cervix and temperature measurement points.

Patient #2209   Temperatures along the tandem were measured inside the tandem tube (a catheter detached during placement), thus the results are loaded with an error associated with the thermal properties of a metal and with the fact, that the tube diameter was larger from the thermo–probe size. This could allow thermo–probe displacements during measurement. The second catheter was successfully positioned 5 to 15 mm away from the tandem (Figure 8.2). The first two temperature points in the second catheter are outside the cervix (in vagina) and probably were not in contact with tissue (the catheter could adhere tampons). This explains a low temperature at those points. The highest temperature range was obtained between the central and side arm axes.

Patient #2309   Temperatures along the central arm axis were measured in a catheter attached to the tandem. Second catheter was placed interstitially at the patient's right, almost parallel to the tandem, 5 mm away in average (Figure 8.3). The highest temperatures were measured between the central and the side arms. The temperature in the interstitial catheter rapidly decrease, when out of cervix. The temperature at the central arm does not decrease when out of cervix due to a thermal properties of a metal.

Patient #2409   Temperatures along the central arm axis were measured in a catheter attached to the central arm (unfortunately the last section of 40mm at the end of the catheter was unaccessible by a thermo-probe). A second catheter was placed interstitially in tissue at the patient's right. The distance between an interstitial thermo-probe and the central arm varies between 20mm at the end and 15mm at the beginning. The temperature decreases at this distance in average by about $5°C$. Unlike in the previous cases, a high temperature level between the central and the side arms was not obtained. This may be explained by the specific position of the ovoids which were shifted back so far that the isolation on the central arm suppressed the electrical field in this area (See the position of ovoids and the isolation on the central arm in Figure 8.4 and compare to Figures 8.2 and 8.3). The retrospective computer simulations was performed for this case. The results, for two different blood perfusion rates are presented in Figure 8.5. It might be seem, that for $W = 1[kg/m^3/s]$, the agreement between the simulation and measurement is quite good.
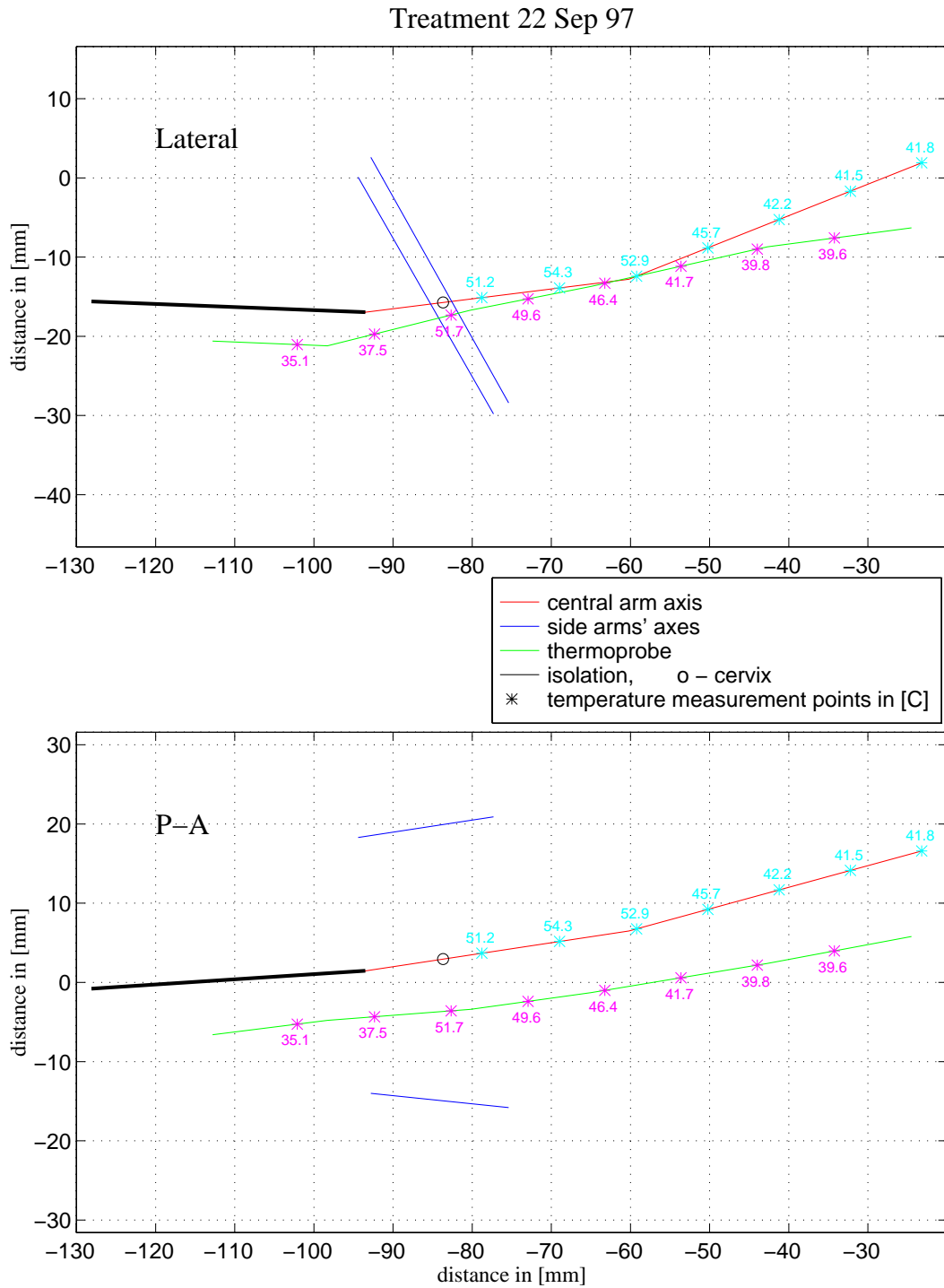
Figure 8.2: *Treatment of patient #2209. The temperatures at the tandem axis were measured inside the central arm. The catheter temperatures were measured in a catheter intracavitary inserted along the central arm. Positions obtained from radio graphs.*
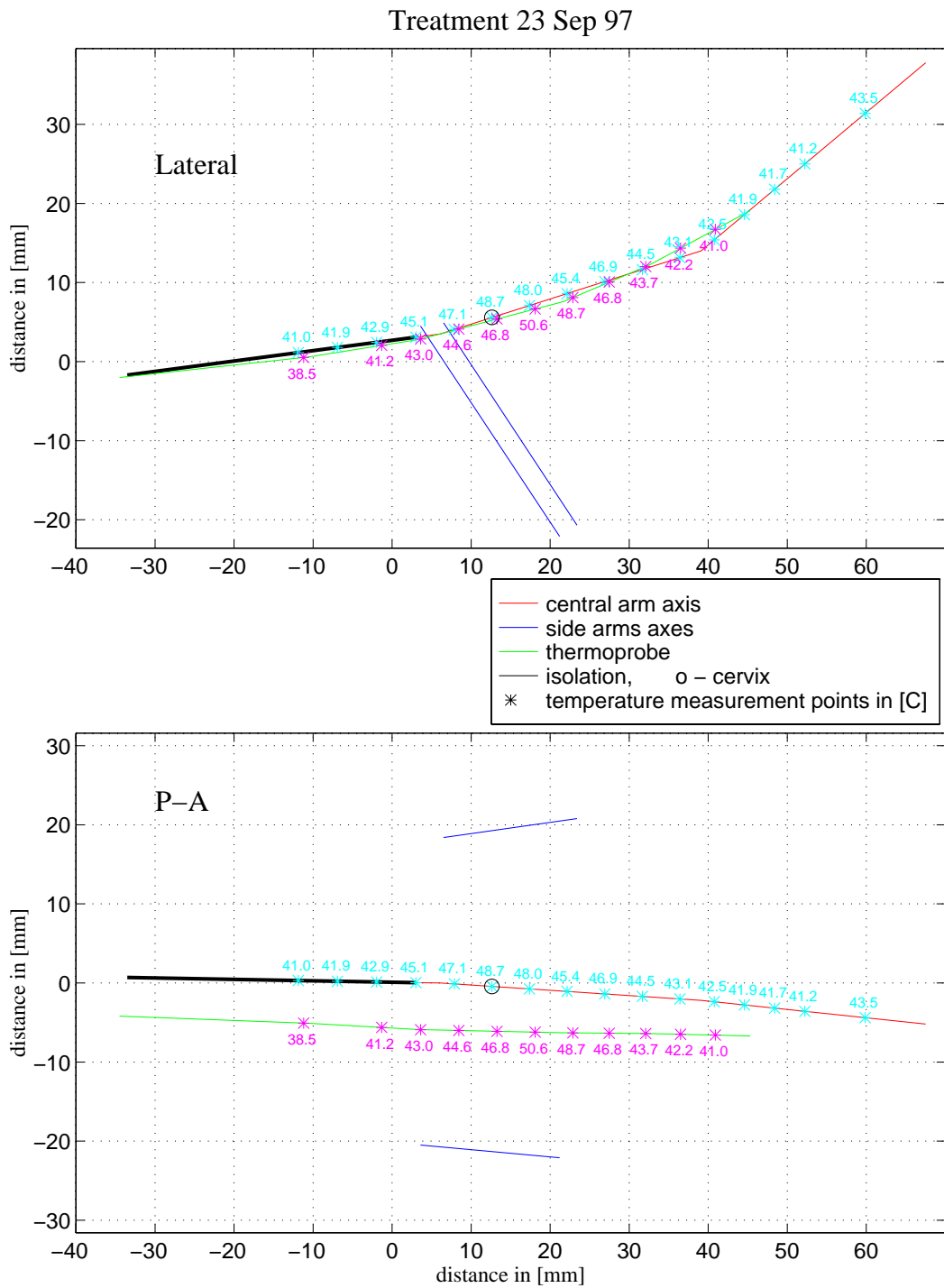
Figure 8.3: *Treatment of patient #2309. The temperatures at the central arm axis were measured in a catheter attached to the tandem. The temperatures in a second catheter were measured interstitially. Positions obtained from radio–graphs.*
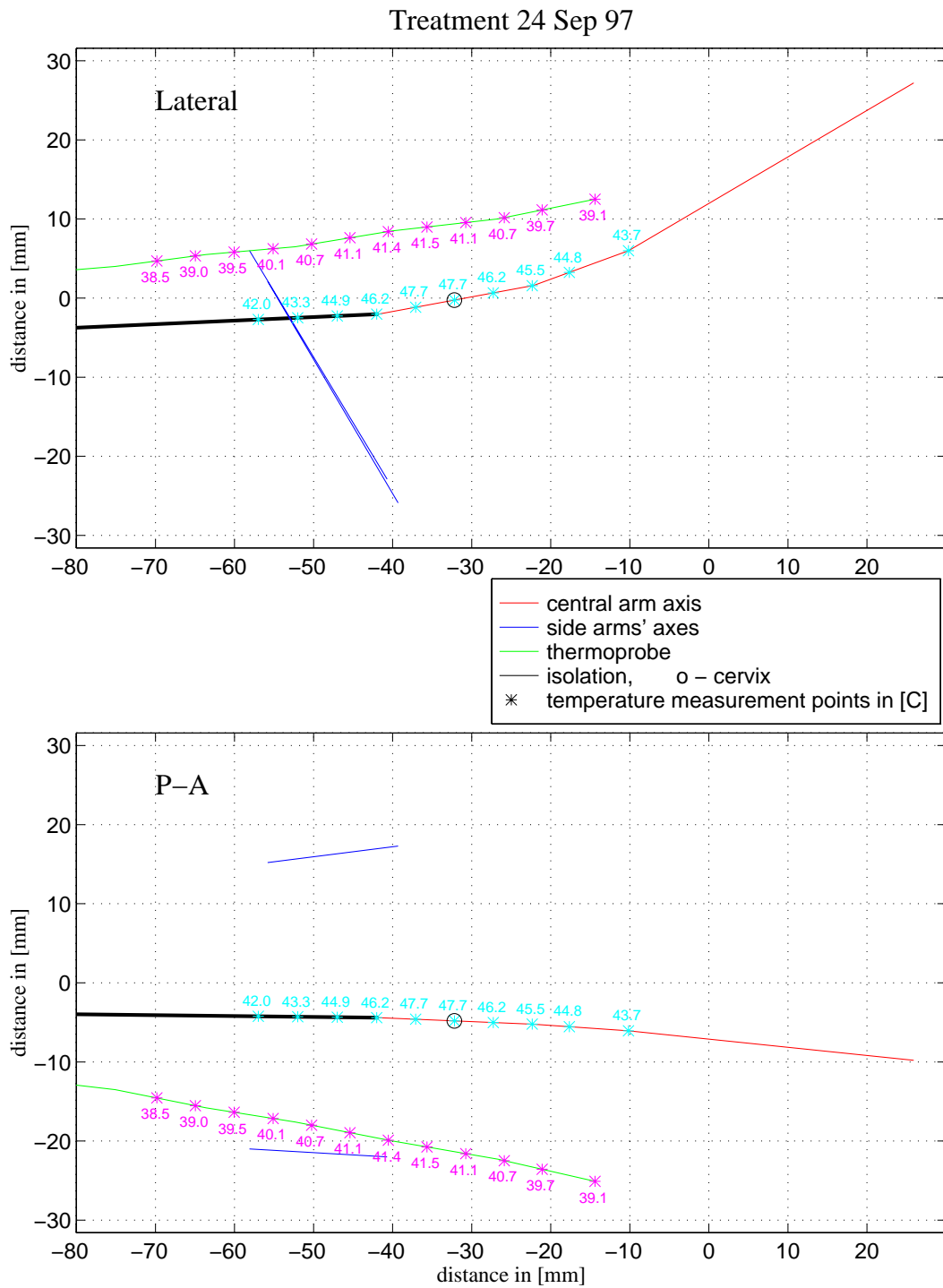
Figure 8.4: *Treatment of patient #2409. The temperatures at the central arm axis were measured in a catheter attached to the central arm. The catheter temperatures were measured interstitially in a catheter inserted in cervix. Positions obtained from radio graphs.*
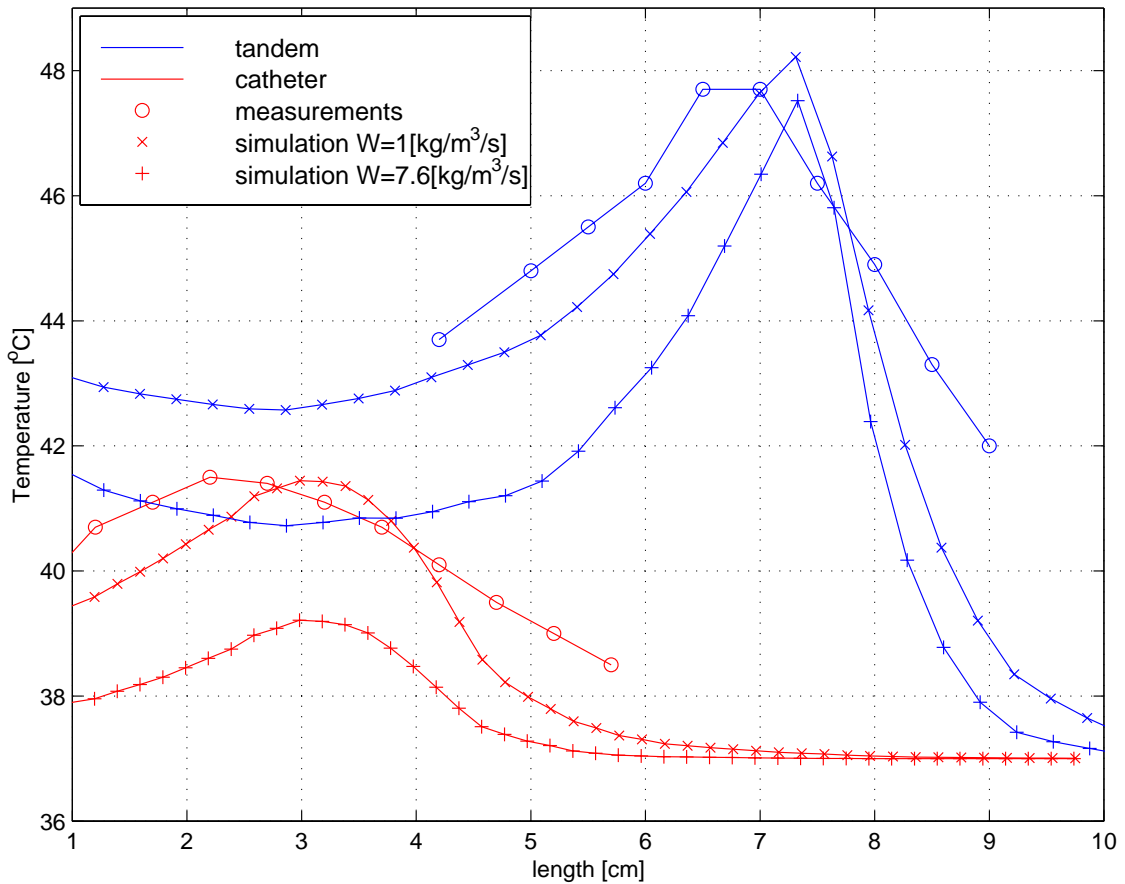
Figure 8.5: *The retrospective simulation for treatment of patient #2409 for two different blood perfusion rates $W = 1[kg/m^3/s]$ and $W = 7.6[kg/m^3/s]$. For the lower perfusion the agreement is quite good. The accuracy of a position of temperature points is about $0.5cm$.*

8.2   Treatment performed with the new hyperthermia system

A set of treatments have been performed using the *HT-2* system. Unfortunately, none of the patients agreed for the interstitial placement of catheters. This precluded temperature measurements in direct contact with tissue. Thus, the thermo couples have been placed inside tandem and ovoid tubes. Such a placement is associated with additional error as described in previous section, but control the temperature not to exceed a specified limit. Example of temperatures and the applied voltage obtained during one of performed treatments of a patient #2907 is presented in Figure 8.6.
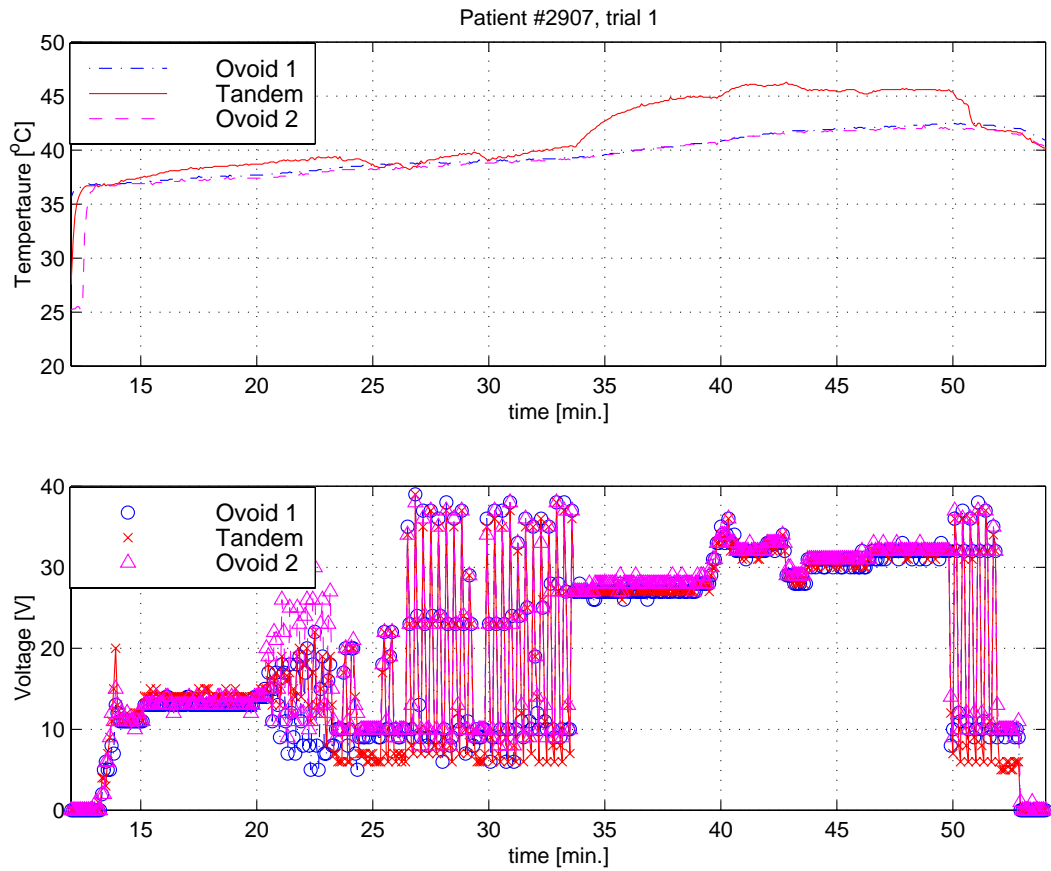
Figure 8.6: *Plot of temperature and voltage of a clinical trial for patient #2907. Temperatures were measured at the end of tandem and ovoids. The voltage applied between 20 and 34 minute and then between 50 and 53 minute was switched every 10 s. in order to obtained a switched mode (as described in Chapter 5)*

.

8.3   Conclusions

The clinical experiments performed with the system prototype (*HT-1*) have shown the potential of using the Fletcher–Suit applicator in hyperthermia. Obtained temperature distributions have shown, that it is possible to obtain a therapeutic temperatures in cervix and along the tandem. Retrospective computer simulations agreed with the measurements, which have validated the approach used in the simulation.

Chapter 9

Summary and conclusions

The presented work showed the comprehensive approach to the treatment of cervical malignancies using a low–frequency hyperthermia system (LFHS) in parallel with brachytherapy. The main difficulty from the engineering point of view was no freedom in selecting the shape of the electrodes. From medical and ethical reasons (the placing of the applicator for the brachytherapy treatment is done under local anesthesia and is traumatic for a patient. Using another applicator for the hyperthermia treatment would increase the patient's trauma), the FSA had to be used as electrodes of the LFHS.

At the beginning of this work, there was an idea to use the modified Fletcher Suit Applicator as electrodes of the low–frequency hyperthermia system. The electrically modified applicator was already prepared for the tests by the Nucletron company for the request of prof. Z. Petrovich from the University of Southern California. The tests, however, required a device, which would excite the applicator's arms. As a first approach, the simple system was designed[1], which could excite the applicator in a simple manner (details are described in Section 6.1). The *HT–1* device was used for the first clinical trials, after some qualitative experiments with the gelatine phantom[2]. These experiments showed, that the arms supporting the applicator's ovoids and this part of a tandem, which is placed in a vagina, should additionally be covered with an insulating paint in order to prevent heating in undesired regions. The results of the first clinical trials were encouraging as the temperature mapping performed during the treatments showed, that the therapeutic temperature range in tissue[3] can be obtained up to about 10–15mm away from the tandem surface

---

[1]The *HT–1* system was designed by dr W. Szkudliński according to the author's direction

[2]The results of those experiments were not presented in this work because of their qualitative character. In the experiment the applicator has been inserted into a gelatine phantom and excited. Then regions, where gelatine was melting were observed

[3]This measurements, presented in Figure 8.4 could be performed thanks to the patient's permission for the interstitial placement of a temperature probe

(Section 8.1). The clinical treatments were very significant, as they gave guidelines for the further work associated with the implementation of the low–frequency hyperthermia system.

One of the conclusions drawn from the initial tests with the *HT–1* system was that the simple system could offer only heating in the whole region surrounding electrodes. As the location of the tumor changes from patient to patient, it becomes obvious that a new system was needed which would offer the selective heating and treatment planning. Such a system, of course, should still use the Fletcher applicator, which can only be utilized as direct contact electrodes at low frequency (the use of the applicator at microwave or RF frequencies is precluded by its predefined shape).

In order to develop the system, the heating was described as a coupled electro–thermal problem. Due to the fact that the wavelength of the operating frequency significantly exceeds the size of a domain, the electric part of the problem could be treated under assumption of the quasi–static character of the field. As a result, the treatment planning involves the solution of the Laplace's equation rather than the full set of Maxwell's equations. The number of unknowns is thus reduced threefold. It has to be noted, that despite this reduction the problem remains computationally difficult.

First of all it is three dimensional. Secondly, the domain has a very complicated shape. Thirdly, different tissues have different electrical parameters. Given these factors there are but a few numerical techniques which can handle the problem. The author's choice was the finite element method (FEM). It has to be noted that while there is a number of commercial FEM packages, virtually all of them represent a traditional approach where the domain is discretized with sufficiently fine irregular or regular grid. This approach is completely inadequate for the purpose of treatment planning because a fine grid requires a long time for its generation and a system of equations becomes very large. This usually leads to a slow convergence and a long computational time of the finite element methods (compare Section 2.2), while it is very important that the simulation is performed very fast, within minutes. The reason is that the treatment planning has to be performed after the placement of the applicator (in order to read the applicator's position within a patient's body) and before treatment initialization (in order to set appropriate excitation of electrodes). The shorter the simulation time the less the patient suffers.

Based on this considerations, the author's proposed the application of one of the state–of–the–art FEM methods based on the multigrid scheme [82, 83]. The multigrid method, virtually unused in electromagnetics, is an efficient tool for the solution of linear equations resulting from a discretization scheme such as FEM. The

approach incorporates standard iterative methods, however, in order to efficiently improve the convergence of the solution it operates on different grid resolutions by coarsening and refining the original mesh. Section 2.2.2 presents four multigrid algorithms, starting from the simplest one, nested iteration, and ending with the most sophisticated one, full multigrid V–cycle. The latter one is characterized by an optimal numerical cost $\mathcal{O}(N)$, i.e. the number of operations is proportional to the number of unknowns. The effectiveness of the multigrid algorithms, applied to the problem at hand, has been tested (Chapter 4) in order to select the one, which would solve the problem in the shortest time. These numerical experiments revealed that, although the full multigrid V-cycle is of optimal numerical complexity and represent the best convergence, it uses more time per one iteration step than the nested iteration scheme. This is because the full multigrid V–cycle needs to perform more grid transfers within one cycle that the nested iteration. It was found that it is profitable to use the full multigrid V-cycle only in those cases, where the number of refinements is sufficiently large and the nested iteration algorithm otherwise. This can also be interpreted, that the efficiency of the multigrid approach strongly depends on the initial grid. Its generation is one of the problems of utmost importance in all FEM calculations. For multigrids, in order to perform a large number of refinements, the initial grid should be as coarse as possible. Additionally, for the treatment planning purposes, the grid generation should be performed very fast, as it has to be generated for each treatment from scratch (electrodes move, distance may be different each time). The data for grid generator is provided by a pair of radio-graphs, that are taken after the FSA is placed in the vagina. It is also theoretically possible to perform MRI and CT for each patient to obtain more detailed data, this, however, is not currently used in medical practice.

The multigrid algorithms, which perform on–line grid refinements can naturally use the adaptive grid refinement strategies, which locally refine the grid according to the error estimator, which indicates where the domain refinement would be computationally most profitable. This mechanism can greatly decrease the memory usage, as the mesh is refined only in regions of high field variations. Nonetheless, the error estimation procedures are very time expensive routines and not always gainful to be performed (see Chapter 4).

Selected numerical algorithms are used in the treatment planning software as described in Chapter 3 and in [85, 84]. The software was developed from own and public domain programs. The latter ones required additional modifications, and improvements and all computer system needed its own data interfaces. The calculated results can be interpolated into a regular grid and saved in a matrix form, or, can be saved in a one of the specified unstructured grid formats.

The software was used for the simulations in order to specify the requirements for the new *HT–2* hyperthermia device. The simulations showed (Chapter 5), that the application of the phase–shifts between electrodes can effectively focus the heat in different regions, depending on the position of a tumor (Figure 5.3). An additional feature introduced by the author – switching between two different excitation modes – additionally increased the possibility of shaping the required temperature pattern (Figure 5.2).

The new *HT–2* hyperthermia system was designed according to the guidelines, resulting for the performed simulations (Section 6.2). The system was tested using liquid and solid (gelatine) phantoms. The measurements in a 0.9%NaCl water solution verified the voltage distributions obtained in the experiment and in the simulation (Section 7.1). The verifications with the gelatine phantoms were performed with a thermo–vision camera. Two measurement methods were used. The first one, which verifies the SAR pattern based on a T-rise method did not give very accurate results because of the too high thermal conductivity of the phantom, nonetheless, it showed the qualitative agreement with the simulation. Using the second method, a thermo–vision camera captured a steady–state temperature distribution of the phantom. The results presented a very good agreement with the simulation and displayed that the *HT–2* device require additional calibration procedure, which was implemented, as presented in Appendix C.

The developed system is not an ideal one, but has enabled the hyperthermia treatments to be initiated. Relating to the features of an ideal low–frequency hyperthermia system, presented in section 1.2, the working system presents the possibility of focusing the power in a specified volume. This has been shown not only in simulations (Figures 5.1, 5.3) but also in experiments (Figures 7.5, 7.6). The author has also undertaken an effort to find a method of approximation of a blood perfusion rate during a treatment (section 2.1.2.2). Unfortunately, temperature measurements during treatments presented the biggest problem, unresolved at present time.

The first claim of this work has been proven, as the FSA can efficiently be used with the *HT-2* system for heating malignant cells located in different parts of the uterus. Initiated clinical trials have shown that therapeutic temperatures are obtained, however, temperature measurements in a whole heated area were not possible, as it would be too traumatic for patients.

The patient's trauma has been of utmost importance in all presented work and thus a focus was set to perform the simulations in the shortest possible time, while a patient awaits a brachytherapy treatment. The selected numerical and visualization techniques – the nested iteration algorithm with a high quality coarse initial grid – presented very high numerical effectiveness and enabled the simulation to be

performed within five minutes. This proves the second claim of the thesis.

Appendix A

Analytical solution of a bio–heat transfer equation in cylindrical coordinates for a specified initial steady state temperature distribution

This analysis has been performed in order to judge how fast a steady state temperature distribution is obtained for an assumed initial temperature distribution and a specified blood perfusion rate (Figure 2.2). Another application of this analysis is the approximation of a blood perfusion rate based on the measured temperature decrease after the power switch off (Figure 2.3)

The temperature distribution after a steady state has been obtained is governed by (2.17). The thermal equilibrium is sustained by a power delivered by a device.

Figure A.1: *Initial temperature distribution $T_0(r)$.*

When the power is switched off, the right hand side of (2.17) disappears and we get a transient state, which can be written as:

$$\rho_t c_t \frac{\partial T}{\partial t} = \nabla \cdot (k \nabla T) - c_b W (T_b - T) \tag{A.1}$$

where T_b is a cooling blood temperature and T is a temperature of a heated region. In order to solve to above equation, we assume the geometry of a domain as in figure A.1 with a diameter of a source $2r_0$, maximal radius r_l and a steady state temperature at
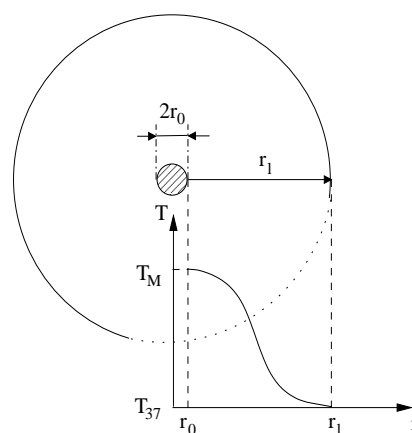
the surface of the source T_M. Assumed initial steady state temperature distribution is presented in figure A.1, for which $\frac{\partial T(r_0)}{\partial r} = 0$ and $\frac{\partial T(r_l)}{\partial r} = 0$.

Temperature increase is equal to:

$$T_w = T - T_b \tag{A.2}$$

and thus:

$$T = T_w + T_b \tag{A.3}$$

$$\nabla^2(T_w + T_b) = \nabla^2 T_w \tag{A.4}$$

$$\frac{\partial(T_w + T_b)}{\partial t} = \frac{\partial T_w}{\partial t} \tag{A.5}$$

Let us write:

$$w = c_b W \tag{A.6}$$

$$W_n = \frac{w}{c_t \rho_t} \tag{A.7}$$

$$k_n = \frac{k}{c_t \rho_t} \tag{A.8}$$

Then, after dividing (A.1) by $c_t \rho_t$ and using (A.7) to (A.8) we get:

$$\frac{\partial T_w}{\partial t} = k_n \nabla^2 T_w - W_n T_w \tag{A.9}$$

We search for the solution of a steady and transient states:

$$T_w(r, t) = T'_w(r)_{t=\infty} + T''_w(r, t) \tag{A.10}$$

The solution problem is one dimensional (due to the symmetry in ϕ and $\frac{dT_w}{dz} = 0$) and thus in cylindrical coordinate system we get:

$$\nabla^2 T_w = \frac{1}{r} \left[\frac{\partial}{\partial r} \left(r \frac{\partial T_w}{\partial r} \right) \right] \tag{A.11}$$

Substituting (A.10) and (A.11) into (A.9) we get:

$$\frac{\partial T''_w}{\partial t} = \frac{k_n}{r} \cdot \frac{\partial}{\partial r} \left(r \frac{\partial T'_w}{\partial r} \right) + \frac{k_n}{r} \cdot \frac{\partial}{\partial r} \left(r \frac{\partial T''_w}{\partial r} \right) - W_n T'_w - W_n T''_w \tag{A.12}$$

and receive the equation for a steady state:

$$\frac{k_n}{r} \cdot \frac{\partial}{\partial r} \left(r \frac{\partial T'_w}{\partial r} \right) - W_n T'_w = 0, \; T_w = 0 \text{ for } w \neq 0 \tag{A.13}$$

and respectively for a transient state:

$$\frac{\partial T_w''}{\partial t} = \frac{k_n}{r} \cdot \frac{\partial}{\partial r}\left(r\frac{\partial T_w''}{\partial r}\right) - W_n T_w'' \tag{A.14}$$

We search the solution of the equation (A.14) in the following form:

$$T_w''(r,t) = R(r) \cdot \tau(t) \tag{A.15}$$

and thus we rewrite:

$$R\frac{\partial \tau}{\partial t} = \tau \cdot \frac{k_n}{r} \cdot \frac{\partial}{\partial r}\left(r\frac{\partial R}{\partial r}\right) - W_n R\tau \tag{A.16}$$

and dividing by $R\tau k_n$ we get:

$$\frac{1}{k_n \tau} \cdot \frac{\partial \tau}{\partial t} = \frac{1}{rR} \cdot \frac{\partial}{\partial r}\left(r\frac{\partial R}{\partial r}\right) - \frac{W_n}{k_n} \tag{A.17}$$

Assuming that:

$$-\mu_1^2 = \frac{1}{k_n \tau} \cdot \frac{\partial \tau}{\partial t} \tag{A.18}$$
$$-\mu_2^2 = \frac{1}{rR} \cdot \frac{\partial}{\partial r}\left(r\frac{\partial R}{\partial r}\right)$$

we can write two differential equations with respect to time and space:

$$\frac{\partial \tau}{\partial t} = -\mu_1^2 k_n \tau \tag{A.19}$$

$$\frac{\partial}{\partial r}\left(r\frac{\partial R}{\partial r}\right) + \mu_2^2 rR = 0 \tag{A.20}$$

and a dispersion equation:

$$\mu_1^2 = \mu_2^2 + \frac{w}{k} \tag{A.21}$$

Equation (A.19) has a solution of the form:

$$\tau = A'e^{-k_n\mu_1^2 t} \tag{A.22}$$

and equation (A.20) can easily be write in the form of a Bessel equation:

$$\frac{\partial^2 R}{\partial r^2} + \frac{1}{r} \cdot \frac{\partial R}{\partial r} + \mu_2^2 R = 0 \tag{A.23}$$
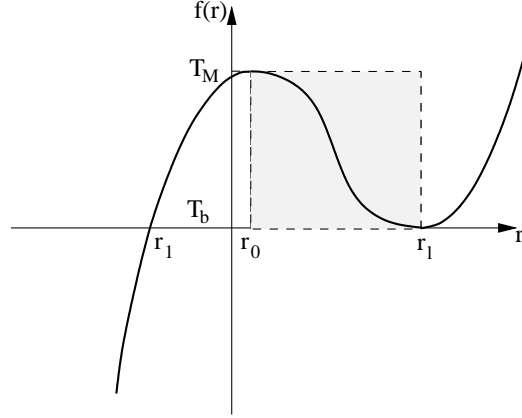
Figure A.2: *Cubic interpolation function approximating the initial condition in a range $< r_0, r_l >$.*

which has a general solution of the form:

$$R = B'J_0(\mu_2 r) + C'Y_0(\mu_2 r) \tag{A.24}$$

The total solution we can write as a product of (A.22) and (A.24):

$$T''_w(r, t) = e^{-k_n\left(\mu^2 + \frac{w}{k}\right)t}\left[AJ_0(\mu r) + BY_0(\mu r)\right] \tag{A.25}$$

where $A = A'B'$, $B = A'C'$ and $\mu = \mu_2$. Because there exists an infinite number of triples A_n, B_n and μ_n, which fulfill equation (A.25), we can write the general solution in the form:

$$T''_w(r, t) = \sum_{n=0}^{\infty} e^{-k_n\left(\mu^2 + \frac{w}{k}\right)t}\left[A_nJ_0(\mu_n r) + B_nY_0(\mu_n r)\right] \tag{A.26}$$

which has to fulfill the initial condition for $t = 0$:

$$T''_w(r, 0) = T''_{W0} = \sum_{n=0}^{\infty}\left[A_nJ_0(\mu_n r) + B_nY_0(\mu_n r)\right] \tag{A.27}$$

Let us interpolate the initial temperature distribution (as seen in Figure A.1) with the 3-rd order polynomial (Figure A.2), which can be represented as a series of $J_0()$ functions. We get:

$$T''_w(r, 0) = ar^3 + br^2 + cr + d = \sum_{n=0}^{\infty} A_nJ_0(\mu_n r) \tag{A.28}$$

and thus we assume $B_n = 0$ and values A_n and μ_n are to be determined. According to Figure A.2 we can write:

$$f(r) = ar^3 + br^2 + cr + d = a(r - r_1)(r - r_l)^2$$

Values r_1 and a can be found from the following conditions:

$$\begin{cases} f(r_0) & = & T_M \\ f'(r_0) & = & 3ar_0^2 + 2br_0 + c = 0 \end{cases} \tag{A.29}$$

After some arrangements we get:

$$r_1 = \frac{3r_0 - r_l}{2} \tag{A.30}$$

$$a = \frac{T_M}{(r_0 - r_1)(r_0 - r_l)^2} = \frac{2T_M}{(r_l - r_0)^3}$$

$$y = a\left[r^3 - \frac{3}{2}(r_l + r_0)r^2 + 3r_lr_0r - \left(\frac{3}{2}r_0 - \frac{1}{2}r_l\right)r_l^2\right]$$

and thus:

$$b = -\frac{3}{2}a(r_l - r_0) \tag{A.31}$$

$$c = 3ar_lr_0 \tag{A.32}$$

$$d = -ar_l^2\left(\frac{3}{2}r_0 - \frac{1}{2}r_l\right) \tag{A.33}$$

In order to determine A_n and μ_n coefficients, the following relation has been used:

$$f(r) = \frac{1}{2}A_0 + \sum_{n=1}^{\infty} A_n J_0(nr), \text{ for } 0 < r < \pi \tag{A.34}$$

where

$$A_0 = 2f(0) + \int_0^\pi \int_0^{\pi/2} u \cdot f'(u\sin(\phi))_u \cdot d\phi \cdot du \tag{A.35}$$

$$A_n = \int_0^\pi \int_0^{\pi/2} u \cdot f'(u\sin(\phi))_u \cdot d\phi \cdot \cos(nu) \cdot du \tag{A.36}$$

First, let us determine the inner integral

$$I = \int_0^{\pi/2} u \cdot f'(u \cdot \sin(\phi)) \cdot d\phi$$

which for $f(r) = ar^3 + br^2 + cr + d$ (a, b, c and d are specified by (A.31) to (A.33)) gives:

$$I = 2a'u^3 + \frac{\pi}{2}b'u^2 + cu \tag{A.37}$$

where

$$a' = 0.75a, \text{ and } b' = 0.8105683b. \tag{A.38}$$

Further:

$$A_0 = 2d + \pi^4 \left(\frac{a'}{2} + \frac{b'}{6} \right) + \frac{\pi^2}{2} c \qquad (A.39)$$

$$A_n = \frac{1}{n^2} \left\{ (-1)^n \left[6a'\pi^2 - \frac{12a'}{n^2} + \pi^2 b' + c \right] + \frac{12a'}{n^2} - c \right\} \qquad (A.40)$$

The final solution, we can thus write in the form:

$$T_w''(r,t) = \frac{1}{2} A_0 e^{-k_n \cdot \frac{w}{k} t} + \sum_{n=1}^{\infty} e^{-k_n \left(n^2 + \frac{w}{k} \right) t} \cdot A_n J_0(nr) \qquad (A.41)$$

or:

$$T_w''(r,t) = \frac{1}{2} A_0 e^{W_n t} + \sum_{n=1}^{\infty} e^{-W_n t} \cdot e^{-k_n \cdot n^2 \cdot t} A_n J_0(nr) \qquad (A.42)$$

$$T_w''(r,t) = e^{W_n t} \left[\frac{1}{2} A_0 + \sum_{n=1}^{\infty} e^{-k_n \cdot n^2 \cdot t} A_n J_0(nr) \right] \qquad (A.43)$$

The variable r in equation (A.43) can vary in the range of $(0, \pi)$. The practical range of variable r is (r_0, r_l) and is hundreds times less (e.g. $r_0 = 0.005, r_l = 0.05$). It is thus necessary to take into account a large number n of series functions. In order to improve the convergence of (A.43), the new variable $r' \in (r_0, r_l)$ is introduced:

$$r' = r \frac{r_l}{\pi} \longrightarrow r = \frac{\pi r'}{r_l}$$

and now equation (A.43) takes the form:

$$T_w''(r',t) = e^{W_n t} \left[\frac{1}{2} A_0' + \sum_{n=1}^{\infty} e^{-k_n \left(\frac{n\pi}{r_l} \right)^2 \cdot t} A_n' J_0(n \frac{\pi}{r_l} r') \right] \qquad (A.44)$$

where:

$$A_0' = 2d + \pi^4 \left(\frac{a_r}{2} + \frac{b_r}{2} \right) + \frac{\pi^2}{2} c_r \qquad (A.45)$$

$$A_n' = \frac{1}{n^2} \left\{ (-1)^n \left[6a_r \pi^2 - \frac{12a_r}{n^2} + \pi^2 b_r + c \right] + \frac{12a_r}{n^2} - c \right\} \qquad (A.46)$$

$$a_r = a' \frac{r_l^3}{\pi^3}, \; b_r = b' \frac{r_l^2}{\pi}, \; \text{and} \; c_r = c \frac{r_l}{\pi}$$

where a' and b' are given by (A.38) and a, b, c, d are given by (A.31)÷(A.33).

Appendix B

Selected algorithms

B.1 Mesh conversions

Mesh conversion is necessary if one wants to make any operation on results, which are stored in different grid formats. In this work, in order to use a superposition principle and sum up electric field intensities saved in different grids such a conversion was necessary. One of the important aspects of this interpolation comes from the fact, that in the finite element methods the interpolation functions are defined for each element separately. Thus, if one want to interpolate a value at a specified point in a domain, an element, that includes this point has to be found first.

Suppose a list of tetrahedra (defined by four vertices) and a list of nodes not associated with tetrahedra. The task is to attribute each node to a tetrahedron, which contains this node within inside.

The first step of the algorithm finds an intersection of domains defined by maximal and minimal extents of nodes' and tetrahedra's coordinates. All points and tetrahedra, which are outside this intersection are ignored afterwards.

The intersection represents a cube. This cube is then split by a number (equal to a `SPLIT_NUMBER`, e.g. 8) of smaller ones and then each of the smaller one is split again as many times as defined by a `SPLIT_DEPTH` parameter. Thus the 1. level contains 1 cube, the second level `SPLIT_NUMBER` cubes and the following levels `SPLIT_NUMBER`^{LEVEL} cubes.

Then each of the tetrahedron is inserted into a one or more element(s) of the structure of cubes in the following way: starting from the deepest level, a number of cells, a tetrahedron fits into, is found. The procedure stops if a number of cells of a specified level is below `INSERT_CONSTANT` parameter (recommended values between $3 \ldots 8$). Thus the size of associated cells is of the order of a tetrahedron.

Then a cell at the deepest level is found for each node. This node is then fitted into one of the tetrahedron associated to this cell. If no tetrahedron was associated

Table B.1: *Description of* `AspectUpperBound` *and* `TriangleSize` *parameters used for surface generation and size of resulting tetrahedral grid and its generation time. Cases a), b) and c) refers to Figure B.2.*

		a)	b)	c)
AspectUpperBound		5.0	5.0	1.0
Triangle Size	`BODY`	4.0	3.0	4.0
	`TANDEM`	0.3	0.15	0.3
	`OVOID1`	1.0	0.4	1.0
	`OVOID2`	1.0	0.4	1.0
Resulting grid size	nodes	473	1853	4278
	tetrahedra	2139	9264	22871
Resulting grid generation time [s]		36.25	203.06	239.68

to this cube, the procedure moves to a cube at a higher level in order search a tetrahedron again and so on until found.

Figure B.1 presents an example of conversion from 2D triangular grid into any list of nodes. In the first step, the algorithm finds an intersection of domain of triangles (green) and domain of nodes (blue). This intersection is marked with red and forms a rectangle which is then split into 4 smaller ones. These four rectangles are associated to level 1. Each of the rectangles from the level 1 are then split again into four rectangles – thus one gets 16 rectangles in level 2 and so on. Finally we get 256 rectangles in level 4.

In the next step each tetrahedron form a list is associated with rectangles from an appropriated level. So, in Figure B.1, the smallest triangle marked in green is linked with two rectangles at level 4, the larger one is related to 4 cells at level 2 and the largest one is associated with 3 cells at level 1.

Then for each node of a new grid (asterisks marked in blue) a cell at the deepest possible level is found and all triangles, that are associated to this cell are checked for the inclusion of this node. This operation can be performed quickly, as only a few triangles are associated to each cell, irrespective of the size of triangle.

B.2   Generation of a surface model of the applicator

The 3D mesh generation program requires that the three dimensional objects be represented by 2D surfaces in 3D space. Those surfaces are to be defined by triangles. Thus, the program, which generates such surfaces, based on coordinates obtained from two radiographs, has been developed. The algorithm of the surface generation
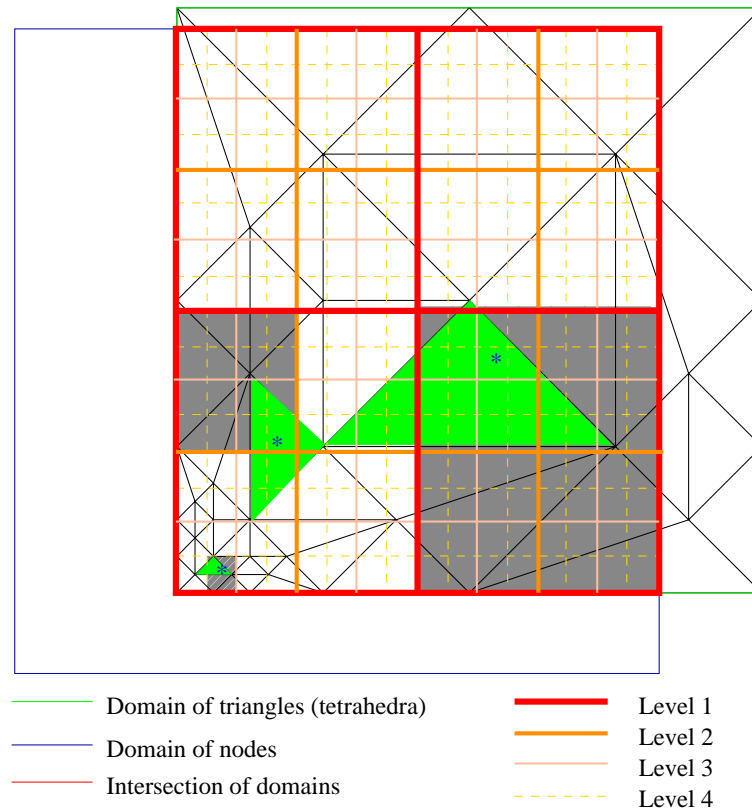
Figure B.1: *Two dimensional example of mesh interpolation routine.*

consists of four steps:

1. Reading description of objects (object are defined as `BODY, TANDEM and OVOID`);

2. The calculation of a number of nodes, triangles and patches for each object;

3. The calculation of the node's coordinates and a generation of a triangular mesh;

4. Writing the mesh to a specified output.

Each object (like a `TANDEM`) at the input is represented by a number of patches. Patches are required for a definition of boundary conditions and for a definition of adjacent media. Each patch can be assigned with different boundary condition. Each object has also defined adjacent medium type (it might be different medium for outside and inside of an object). A description of parameters for data input is shown in Table B.2.

Two of the parameters – `AspectUpperBound` and `TriangleSize` – which can be different for each object, influence the size and the quality of a tetrahedral grid. Thus
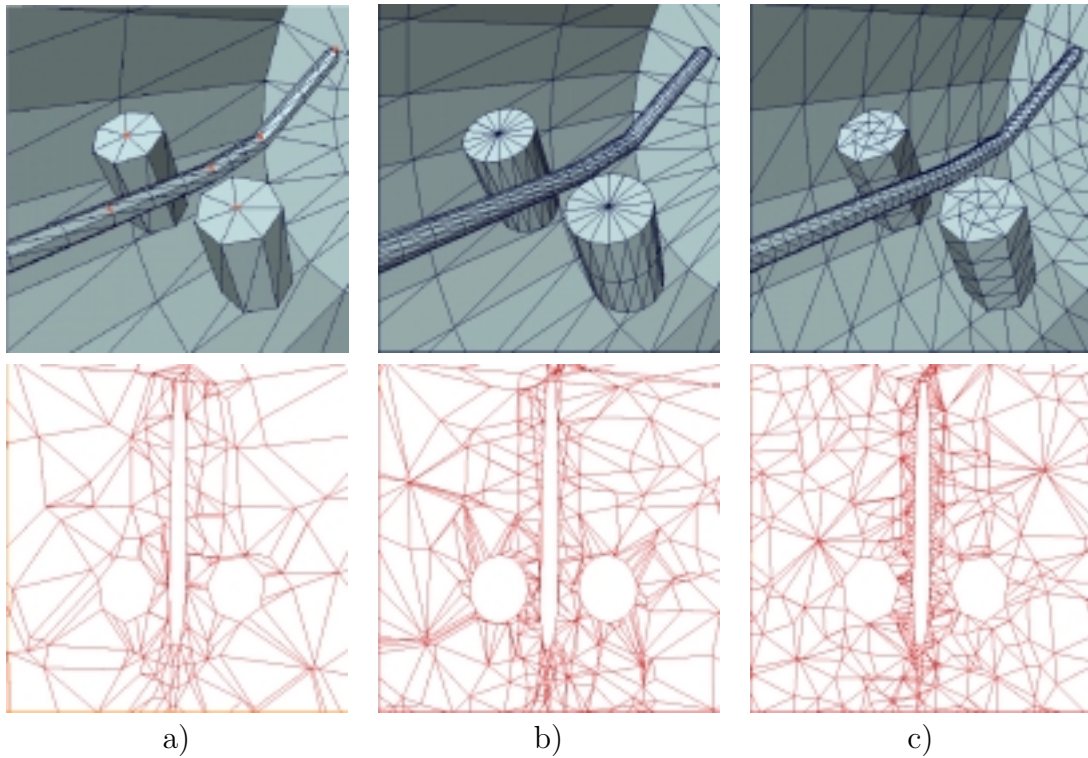
Figure B.2: *An effect of changes in* `AspectUpperBound` *and* `TriangleSize`*. The Figure presents a view of a generated 2D surfaces (upper row) and a cross–section of a tetrahedral grid generated by* `tetgen` *(lower row). Detailed values are shown in Table B.1*

examples with different values set for those parameters are presented in Figure B.2 and in Table B.1. Note, that changes in triangle size not only influence the quality of approximated shapes, but may also significantly increase the grid size and time required for its generation. Another parameter, `AspectUpperBound`, controls the ratio of generated triangles. The `tetgen` grid generator required this parameter to be below five. Also in this case a decrease in this value increases the grid size ant the time required for its generation.

Table B.2: *Input data format*

Name	Default value	Meaning
AspectUpperBound	5.0	The maximum aspect ratio set for triangle edges.
NoOfTandems	1	Number of tandems in domain. For this application only the default value is used (0 is also possible if only ovoids are present).
NoOfOvoids	2	Number of ovoids.
Triangle size	-	The maximum size of a triangle edge (in [mm]). Separately defined for each object.
X_radius	12	Half of a patient's width in [cm] (object BODY).
Y_radius	16	Half of a patient's height in [cm] (object BODY).
Segments	0	Defines number of walls of a right regular prism to approximate a cylinder. If 0, triangle size determines a number of segments.
Length	30	Length of a domain in [cm]
Inside	1	Determines a direction of node's numbering. If 1, counterclockwise.
FrontAspect	1	Additional parameter for controlling triangle aspect at the front of an object
EndAspect	1	Additional parameter for controlling triangle aspect at the end of an object
InnerRegion	Tissue or "-"	Medium type inside of an object. "-" defines no medium (or domain outside)
OuterRegion	Tissue or "-"	Medium type inside of an object. "-" defines no medium (or domain outside)
Shift	0.0 0.0 0.0	Defines an origin for the object BODY
Radius	0.3 (TANDEM) 1.0 (OVOIDS)	radius of an object
Parts	4	Number of segments for a definition of a TANDEM. This implies number of coordinate points for the input (as marked in red in Figure B.2
Ending	1	Determines an existence of rounded tip at the end of the *TANDEM*
P1...Pi	$i = 5$ (TANDEM) $i = 2$ (OVOIDS)	x, y, x coordinate points for each Pi

Appendix C

System Calibration

This appendix presents a method of calibration the *HT-2* hyperthermia system (described in Chapter 6) in order set correct phase–shifts between each pair of electrodes, depending on a patient's body impedance. The patient's body with three excited electrodes and surrouding metal foil belt can be represented as an electrical circuit presented in Figure C.1. Three current sources represent the excitation of each electrode. In order to fully describe the load of the system one needs to know six conductances – three, which represent relative conductances between each pair of the electrodes (G_{12}, G_{13}, G_{23}) and three, which represent conductance of each electrode to ground (G_{10}, G_{20}, G_{30}). The knowledge of the device output impedance (G_t) is also required.

The first step of the calibration process is the measurement of those impedances. If one sets equal voltage and no phase–shifts among electrodes, the electric current
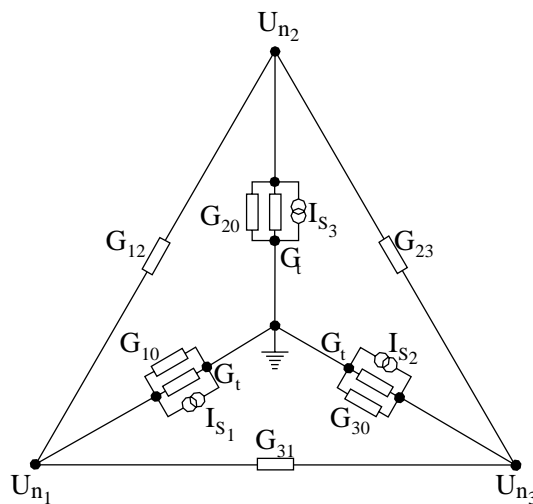

Figure C.1:

flows only to the metal foil belt (there is no flow of the electric current among electrodes) and thus the values of ground conductances are obtained (G_{10}, G_{20}, G_{30}). Relative conductances (G_{12}, G_{13}, G_{23}) are obtained by exciting one of the electrode, while grounding the others with detached metal foil belt. This measurement has to be repeated three times for each electrode. In such a case one gets three conductances, which can be written as:

$$G_A = G_{12} + G_{13} + G_{10} + G_t \tag{C.1}$$

$$G_B = G_{12} + G_{23} + G_{20} + G_t \tag{C.2}$$

$$G_C = G_{23} + G_{13} + G_{30} + G_t \tag{C.3}$$

Based on this equations, relative conductances are found easily:

$$G_{12} = \frac{1}{2}[G_A + G_B - G_C - G_{10} - G_{20} + G_{30} - G_t] \tag{C.4}$$

$$G_{23} = \frac{1}{2}[-G_A + G_B + G_C + G_{10} - G_{20} - G_{30} - G_t] \tag{C.5}$$

$$G_{13} = \frac{1}{2}[G_A - G_B + G_C - G_{10} + G_{20} - G_{30} - G_t] \tag{C.6}$$

All the measurements are performed by a voltage and current meter included in the *HT-2* system and are displayed on the screen.

The second step of the calibration process is the phase adjustment – i.e. the calculation of the source phase–shifts to be set in the device for the required phase–shifts between electrodes. This calculation is accomplished by a solution of the system of equations resulting from the nodal voltage method for the circuit presented in Figure C.1.

The voltage at each electrode is represented by the nodal voltages U_{n_i}, $i = 1 \ldots 3$ in the picture and thus the phase–shift between electrodes is equal to the difference of angle of nodal voltages U_{n_i}.

One can thus finds the required phases for the sources by using the method of nodal voltages and by a solution of the following matrix equation:

$$\boldsymbol{I}_s = \boldsymbol{G}\boldsymbol{U}_w \tag{C.7}$$

which is also equivalent to

$$\boldsymbol{U}_s = Z_t\boldsymbol{G}\boldsymbol{U}_w \tag{C.8}$$

where $\boldsymbol{U}_s = [U_{s_1}\ U_{s_2}\ U_{s_3}]^T$ is the voltage efficiency of the sources, $\boldsymbol{U}_n = [U_{n_1}\ U_{n_2}\ U_{n_3}]^T$ is the voltage at the applicator electrodes and $\boldsymbol{G}$ is the conductance matrix equal

to:

$$\boldsymbol{G} = \begin{bmatrix} G_{10} + G_{12} + G_{13} + G_t & -G_{12} & -G_{13} \\ -G_{12} & G_{20} + G_{12} + G_{23} + G_t & -G_{23} \\ -G_{23} & -G_{12} & G_{30} + G_{13} + G_{23} + G_t \end{bmatrix}$$

$$(\text{C}.9)$$

This calculations are performed by an additional software supplied with the device.

Acknowledgments

First of all, I would like to express my deep gratitude to my supervisor, Prof. Michał Mrozowski, for the scientific education, constant help, inspirations and support in many ideas that lead this work to a successful end.

This thesis would not have been possible without the help and support of my father, Dr. Piotr Dębicki, who has introduced me into hyperthermia and has always been stimulating my scientific interest. I greatly benefited from his deep practical knowledge and long experience in this field.

I respectfully thank to prof. Z. Petrovich from the University of Southern California, who presented the idea of using the Fletcher–Suit applicator in hyperthermia, sponsored the construction of the both hyperthermia devices and encouraged me to write publications.

I am indebted to prof. J. Zieliński, the head of the Department of Gynecologic Oncology in Center of Oncology, Warsaw and to Dr. N. Piotrkowicz for help, cooperation, medical education and for supervising the first clinical trials.

I wish to thank Dr. W. Szkudliński and M. Szkudliński for construction of the hyperthermia devices and to M. Stefaniak for writing the codes for the mesh interpolation and surface triangulation routines.

I thank to State Committee of Scientific Research, which has sponsored this work with two grants, under the contract numbers 8 T11E 021 10 and 8 T11E 015 20.

I appreciate the help of Krzysztof Nyka, especially common discussions concerning multigrid methods and grid generators. I also want to express my thank to my colleagues, I have shared a single room with for five years – Piotr Jędrzejewski, Jacek Mielewski, Piotr Przybyszewski and Michał Rewieński. The time spent together, common work and discussions on many subjects will always be a nice memory to me.

I am grateful to my mother, her prayers have always been supporting my work and to my grandma, Basia, who has never stopped asking me question *"Ain't you a doctor yet?"*.

Last but not least words of my appreciation and gratitude to my wife Agnieszka

Copyright note

Niniejszym wyrażam zgodę na wykorzystanie wyników mojej pracy, w tym tabel i rysunków, w pracach badawczych i publikacjach przygotowywanych przez pracowników Politechniki Gdańskiej lub pod ich kierownictwem. Warunkiem skorzystania z mojej zgody jest wskazanie niniejszej rozprawy doktorskiej jako źródła.

Bibliography

[1] R. Beck, P. Deuflhard, H.C. Hege Seebass M, and D. Stalling. Numerical algorithms and visualization in medical treatment planning. Technical Report SC-96-54, Konrad-Zuse-Zentrum für Informationstechnik Berlin, Heilbronner Str. 10, D-10711 Berlin-Wilmersdorf, December 1996.

[2] R. Beck, B. Erdmann, and R. Reiner. Kaskade 3.0, an object-oriented adaptive finite element code. Technical Report TR 95-4, ZIB Konrad-Zuse-Zentrum für Informationstechik, Berlin, Germany, 1995.

[3] R. Beck, B. Erdmann, and R. Reiner. An object oriented adaptive finite element code: Design issues na applications in hyperthermia treatment planninig. In E. Arge, A.M. Bruaset, and H.P. Langtangen, editors, *Modern Software Tools for Scientific Computing*, pages 105–124. Birkhäuser, Boston–Basel–Berlin, 1997.

[4] R. Beck, B. Erdmann, and R. Roitzsch. KASKADE User's Guide. Technical Report TR 95-11, ZIB Konrad-Zuse-Zentrum für Informationstechik, Berlin, Germany, December 1995.

[5] W.L. Briggs. *A multigrid tutorial*. SIAM, Philadeplphia, 1987.

[6] S.A. Cannistra and J.M. Niloff. Cancer of the uterine cervix. *New England Journal of Medicine*, 16(334):1030–8, 1996.

[7] C.K. Charny and R.L. Levin. A three-dimensional thermal and electromagnetic model of whole limb heating with a MAPA. *IEEE Transactions on Biomedical Engineering*, 38(10):1030–9, October 1991.

[8] S.T. Clegg, S.K. Das, E. Fullar, S. Anderson, J. Blivin, J.R. Oleson, and T.V. Samulski. Hyperthermia treatment planning and temperature distribution reconstruction: a case study. *Int. J. Hyperth. (UK)*, 1(12):65–76, January – February 1996.

[9] C.T. Coughlin, T.Z. Wong, T.P. Ryan, E.L. Jones, R.W. Crichlow, P.K. Spiegel, and R. Jeffery. Interstitial microwave-induced hyperthermia and iridium brachytherapy for the treatment of obstructing biliary carcinomas. *International Journal of Hyperthermia*, 2(8):157–71, March – April 1992.

[10] J. de Bree, J.F. van der Koijk, and J.J.W. Lagendijk. A 3-D SAR model for current source interstitial hyperthermia. *IEEE Transactions on Biomedical Engineering,*, 43(10):1038–45, October 1996.

[11] M.P. Debicki and P.S. Debicki. A new finger-type applicator for microwave hyperthermia. In *11th International Microwave Conference. MIKON - 96.*, volume 2, pages 628–32, Warsaw, Poland, May 1996.

[12] P.S. Debicki, M. Okoniewski, E. Okoniewska, P.N. Shrivastava, A.M. Debicka, L.V. Baert, and Z. Petrovich. Cooled microwave transrectal applicator with adjustable directional beam for prostate treatment. *International Journal of Hyperthermia*, 1(11):95–108, January – February 1995.

[13] I.K.K. Deurloo, A.G. Visser, M. Morawska, C.A.J.F. van Geel, G.C. van Rhoon, and P.C. Levendag. Application of a capacitive-coupling interstitial hyperthermia system at 27 MHz: study of different applicator configurations. *Phys. Med. Biol. (UK)*, 36(1):119–32, January 1991.

[14] J.D.P. Van Dijk, D. Gonzalez-Gonzalez, and L.C.E.M. Blank. Deep local hyperthermia with a four aperture array system of large waveguide radiators. Results of simulation and clinical application. In T. Sugahara and M. Saito, editors, *Hyperthermic Oncology, Summary Papers*, volume 1. Taylor & Francis, London, 1988.

[15] S. Egawa, K. Ishioka, and Y. Kawada. Trials of combined radiation and hyperthermia with various heating modalities in cancer therapy. *Radiation Medicine*, 4(2):260–4, October – December 1984.

[16] B. Emami, R.J. Myerson, C. Scott, .F Gibbs, C. Lee, and C.A. Perez. Phase I/II study, combination of radiotherapy and hyperthermia in patients with deep-seated malignant tumors: report of a pilot study by the Radiation Therapy Oncology Group. *International Journal of Radiation Oncology, Biology, Physics*, 1(20):73–9, January 1991.

[17] C.A. Van Es, H.K. Wyrdeman, de A.A. Leeuw, J. Mooibroek, J.J. Lagendijk, and J.J. Battermann. Regional hyperthermia of pelvic tumours using the

Utrecht 'Coaxial TEM' system: a feasibility study. *International Journal of Hyperthermia*, 2(11):173–86, March – April 1995.

[18] H.J. Feldmann, M. Molls, S. Adler, M. Meyer-Schwickerath, and H. Sack. Hyperthermia in eccentrically located pelvic tumors: excessive heating of the perineal fat and normal tissue temperatures. *International Journal of Radiation Oncology, Biology, Physics*, 5(20):1017–22, May 1991.

[19] H.J. Feldmann, M. Molls, S. Krumplemann, M. Stuschke, and H. Sack. Deep regional hyperthermia: comparison between the annular phased array and the sigma-60 applicator in the same patients. *International Journal of Radiation Oncology, Biology, Physics*, 1(26):111–6, April 1993.

[20] J. Gellermann, D. Stalling, W. Tillyt, P. Deuflhard, P. Wust, and R. Felix. Practical exercises with the hyperthermia treatment palnning. In *International Congress Hyperthermia in Clincal Oncology. Abstract book.*, page 18, Venice, Italy, May 1998.

[21] A.W. Guy and C-K. Chou. Physical aspects of localized heating by radiowaves and microwaves. In F.K. Storm, editor, *Hyperthermia in cancer therapy*, pages 279–304. G.K. Hall Medical Publishers, Boston, 1983.

[22] J.W. Hand, P.R. Blake, J.W. Hopewell, H.W. Lambert, and S.B. Field. A coaxial applicator for intracavitary hyperthermia of carcinoma of the cervix. *Progress in Clinical & Biological Research*, (107):635–9, 1982.

[23] K. Hasegawa, M. Kinugasa, R. Nishino, A. Kimura, N. Yukimura, F. Ohtsu, and K. Takeuchi. Cytological and histological effects of regional hyperthermia and radiation in cancer of the uterine cervix. *Nippon Gan Chiryo Gakkai Shi - Journal of Japan Society for Cancer Therapy.*, 8(24):1526–38, August 1989.

[24] J. Haveman. The pH of the cytoplasm as an important factor in the survival of *in vitro* cultured malignant cells after hyperthermia. Effects of carbonylcyanide 3 chlorophenyl hydrazone. *European Journal of Cancer*, (15):1281–1288, 1979.

[25] N.B. Hornback, R.E. Shupe, H. Shidnia, C.U. Marshall, and T. Lauer. Advanced stage IIIB cancer of the cervix treatment by hyperthermia and radiation. *Gynecologic Oncology*, 2(23):160–7, February 1986.

[26] M.F. Iskander, P.F. Turner, J.B. DuBow, and J. Kao. Two-dimensional technique to calculate the EM power deposition pattern in the human body. *Journal of Microwave Power*, 3(17):175–85, September 1982.

[27] R.D. Issels, J. Mittermuller, A. Gerl, W.Simon, A. Ortmaier, C. Denzlinger, H. Sauer, and W. Wilmanns. Improvement of local control by regional hyperthermia combined with systemic chemotherapy (ifosfamide plus etoposide) in advanced sarcomas: updated report on 65 patients. *Journal of Cancer Research & Clinical Oncology.*, Suppl 4(117):141–7, 1991.

[28] J. Jin. *The Finite Element Method in Electromagnetics.* John Wiley & Sons, New York, 1993.

[29] D.S. Kapp. Indications for the clinical use of deep local and regional hyperthermia in conjunction with radiation therapy. *Strahlentherapie und Onkologie*, 10(165):724–8, October 1989.

[30] E.R. Lee, T.R. Wilsey, P. Tarczy-Hornoch, D.S.Kapp, P. Fessenden, A. Lohrbach, and S.D. Prionas. Body conformable 915 MHz microstrip array applicators for large surface area hyperthermia. *IEEE Transactions on Biomedical Engineering*, 5(39):470–83, May 1992.

[31] G.T. Martin, M.G. Haddad, E.G. Cravalho, and H.F. Bowman. Thermal model for the local microwave hyperthermia treatment of benign prostatic hyperplasia. *IEEE Transactions on Biomedical Engineering*, 39(8):836–44, August 1992.

[32] S.F. McCormick. *Multilevel Adaptive Methods for Partial Differential Equations.* SIAM, New York, USA, 1992.

[33] A.J. Milligan, J.A. Metz, and D.B. Leeper. Effect of hyperthermia on the radiation response of Chinese hamster small intestine. *The British Journal of Radiology*, (58):741–744, 1985.

[34] M. Mrozowski and M.A. Stuchly. Parametrization of media dispersive propoerties for fdtd. *IEEE Transactions on Antennas and Propagation*, 45(9):1438–39, September 1997.

[35] R.J. Myerson, L. Leybovich, B. Emami, P.W. Grigsby, W. Straube, and D. Von Gerichten. Phantom studies and preliminary clinical experience with the BSD 2000. *International Journal of Hyperthermia*, 7(6):937–51, November – December 1991.

[36] O.S. Nielsen, J. Overgaard, and T. Kamura. Influence of thermotolerance on the interaction between hyperthermia and radiation in a solid tumour in vivo. *The British Journal of Radiology*, 56(664):267–73, April 1983.

[37] Nucletron Engineering BV., P.O. BOX 110, 3956 ZT Leersum, The Netherlands. *Selectron (company catalogue)*, 1985.

[38] E. Okoniewska, M. Okoniewski, and P. Debicki. Relative, $\sigma|E|^2$ heating patterns in multilayered biological tissue exposed to a cylindrical waveguide applicator. In *Sixth International Conference on Antennas and Propagation (ICAP 89)(Conf. Publ. No.301)*, Conventry, UK, April 1989.

[39] J. Overgaard. Simultaneous and sequential hyperthermia and radiation treatment of an experimental tumor and its surrounding tissue in vivo. *International Journal of Radiation Oncology, Biology and Physics*, (6):1507–1517, 1980.

[40] J. Overgaard. Hyperthermia as an adjuvant to radiotherapy. *Sthralentherapie and Onkologie*, 8949(163):453–457, 1987. Review of the randomized multicenter studies of the European Society Hyperthermic Oncology.

[41] J. Overgaard, D. Gonzalez-Gonzalez, M.C. Hulshof, G. Arcangeli, O. Dahl, O. Mella, and S.M. Bentzen. Hyperthermia as an adjuvant to radiation therapy of recurrent or metastatic malignant melanoma. A multicentre randomized trial by the European Society for Hyperthermic Oncology. *International Journal of Hyperthermia*, 1(12):3–20, January – February 1996.

[42] L.S. Parker, T. Tong, S. Bolden, and P.A. Wingo. Cancer statistics. *CA Cancer J. Clin.*, (65):5–27, 1996.

[43] K.D. Paulsen, X. Jia, and J.M Sullivan Jr. Finite element computations of specific absorption rates in anatomically conforming full-body models for hyperthermia treatment analysis. *IEEE Transactions on Biomedical Engineering*, 40(9):933–45, September 1993.

[44] K.D. Paulsen and D.R. Lynch. Elimination of vector parasities in finite element solutions. *IEEE Transactions on Microwave Theory & Techniques*, 39:395–404, 1991.

[45] H.H. Pennes. Analysis of tissue and arterial blood temperatures in the resting human forearm. *J. Appl. Phys.*, (1):93–122, 1948.

[46] C.A. Perez. International consensus meeting on hyperthermia final report. *International Journal of Hyperthermia*, (6):839–877, 1990.

[47] C.A. Perez, B. Emami, R.J. Myerson, and J.L. Roti Roti. Hyperthermia. In C.A. Perez and L. Brady, editors, *Principles and practice of radiation oncology*, pages 396–447. Lippincott, 1992.

[48] N. Piotrkowicz. Private communication, 1999.

[49] M. Piotrowska. Radiator do hipertermii mikrofalowej o osiowej charakterystyce promieniowania. Master Thesis, Technical University of Gdańsk, 1986.

[50] S.D. Prionas, D.S. Kapp, D.R. Goffinet, M.A. Bagshow, R. Ben-Yousef, J.L. Sokol, and P. Fessenden. Interstitial frequency–induced hyperthermia. In E. Gerner and T. Cetas, editors, *Hyperthermic Oncology 1992*, volume 2, pages 249–53, The Arisona Board of Regents, Arizona, 1992.

[51] H.S. Rainhold and B. Endrich. Tumour microcirculation as a target for hyperthermia. *International Journal of Hyperthermia*, (2):111–137, 1986.

[52] R.C. Rietbroek, M.S. Schilthuis, P.J. Bakker, van J.D. Dijk, A.J. Postma, D. Gonzalez Gonzalez, A.J. Bakker, van der J. Velden, T.J. Helmerhorst, and C.H. Veenhof. Phase II trial of weekly locoregional hyperthermia and cisplatin in patients with a previously irradiated recurrent carcinoma of theuterine cervix. *Cancer*, 5(79):935–43, March 1997.

[53] D. Roos, M.H. Seegenschmied, G. Klautke, J. Erb, and B. Sorbe. A new microwave applicator with integrated cooling system for intracavitary hyperthermia of vaginal carcinoma. *International Journal of Hyperthermia*, 12(6):743–56, November – December 1996.

[54] T.P. Ryan, J.H. Taylor, and C.T. Coughlin. Interstitial microwave hyperthermia and brachytherapy for malignancies of the vulva and vagina. I: Design and testing of a modified intracavitary obturator. *International Journal of Radiation Oncology, Biology, Physics*, 1(23):189–99, 1992.

[55] Y. Saad. *Iterative Methods for Sparse Linear Systems*. PWS Publishing Company, Boston, 1995.

[56] M. Sadiku. *Numerical Techniques in Electromagnetics*. CRC Press, Boca Raton, 1992.

[57] M.D. Sapozink, G. Joszef, M.A. Astrahan, F.A. Gibbs Jr, Z. Petrovich, and J.R. Stewart. Adjuvant pelvic hyperthermia in advanced cervical carcinoma. I. Feasibility, thermometry and device comparison. *International Journal of Hyperthermia*, 6(6):985–96, November – December 1990.

[58] P.F. Turner A. Tumeh T. Schaefermeyer. BSD-2000 approach for deep local and regional hyperthermia: physics and technology. *Strahlentherapie und Onkologie*, 10(165):738–41, October 1989.

[59] P.F. Turner T. Schaefermeyer. BSD-2000 approach for deep local and regional hyperthermia: clinical utility. *Strahlentherapie und Onkologie*, 10(165):700–4, October 1989.

[60] M. Seebass. Private communication, 1998.

[61] M. Seebass, D. Stalling, H.C. Hege, P. Wust, R. Felix, and P. Deuflhard. New Features of HyperPlan, a hyperthemia planning system. In *International Congress Hyperthermia in Clincal Oncology. Abstract book.*, page 16, Venice, Italy, May 1998.

[62] M.H. Seegenschmiedt, R. Sauer, C. Miyamoto, J.A. Chalal, and L.W. Brady. Clinical experience with interstitial thermoradiotherapy forlocalized implantable pelvic tumors. [review] [81 refs]. *American Journal of Clinical Oncology*, 3(16):210–22, June 1993.

[63] S. Sharma, S. Singhal, A.P. Sandhu, S. Ghoshal, B.D. Gupta, and N.S. Yadav. Local thermo-radiotherapy in carcinoma cervix: improved local control versus increased incidence of distant metastasis. *Asia-Oceania Journal of Obstetrics & Gynaecology*, 1(17):5–12, March 1991.

[64] D.S. Shimm, T.C. Cetas, K.H. Hynynen, D.N. Buechler, D.P. Anhalt, H.F. Sykes, and J.R. Cassady. The CDRH helix. A phase I clinical trial. *American Journal of Clinical Oncology*, 2(12):110–3, April 1989.

[65] D. Sullivan. Mathematical methods for treatment planning in deep regional hyperthermia. *IEEE Transactions on Microwave Theory & Techniques*, 39(5):864–72, May 1991.

[66] D.M. Sullivan, R. Ben-Yosef, and D.S. Kapp. Stanford 3D hyperthermia treatment planning system. Technical review and clinical summary. *International Journal of Hyperthermia*, 5(9):627–43, September – October 1993.

[67] A. Taflove, editor. Computational Electrodynamics. Artech House, Boston, London, 1995.

[68] D.E. Thrall, D.M. Prescott, T.V. Samulski, M.W. Dewhirst, J.M. Cline, J. Lee, R.L. Page, and J.R. Oleson. Serious toxicity associated with annular microwave array induction of whole-body hyperthermia in normal dogs. *International Journal of Hyperthermia*, 1(8):23–32, January – February 1992.

[69] N. Tsuda, K. Kuroda, and Y. Suzuki. An inverse method to optimize heating conditions in RF-capacitive hyperthermia. *IEEE Transactions on Biomedical Engineering*, 43(10):1029–37, October 1996.

[70] S. Uehara, J. Omagari, and K. Hata. Deep local and regional hyperthermia with annular phased array. *Strahlentherapie und Onkologie*, 10(165):715–6, October 1989.

[71] R. Valdagni, M. Amichetti, and L. Cristoforetti. Intracavitary hyperthermia: construction and heat patterns of individualized vaginal prototype applicators. *International Journal of Hyperthermia*, 4(5):457–66, September – October 1988.

[72] J. van der Koijk. *The multi–electrode current–source interstitial hyperthermia system*. PhD thesis, Universiteit Utrecht, the Netherland, 1997.

[73] J.F. van der Koijk, J. De Bree, J. Crezee, and J.J.W. Lagendijk. Numerical analysis of capacitively coupled electrodes for interstitial hyperthermia. *International Journal of Hyperthermia*, 13(6):607–19, November – December 1997.

[74] S.A. Vavasis. *QMG 1.1 Mesh Generation*. Cornell University,USA, http://www.cs.cornell.edu/home/vavasis/qmg1.1/meshgen.html, 1996.

[75] C-Q. Wang and O.P. Gandhi. Numerical simulation of annular phased arrays for anatomically based models using the fdtd method. *IEEE Transactions on Microwave Theory & Techniques*, 37(1):118–26, January 1989.

[76] C.C. Wárlám-Rodenhuis, A.A.C. De Leeuw, S.Y. El Sharouni, and P. Bouma. Regional hyperthermia in combination with radiotherapy in patients with locally advanced cervical cancer. In *International Congress Hyperthermia in Clincal Oncology. Abstract book.*, page 27, Venice, Italy, May 1998.

[77] P. Wessling. *An Introduction to Multigrid methods*. John Wiley & Sons, New York, 1992.

[78] A. Westra and W.C. Dewey. Variation in sensitivity to heat shock during the cell cycle of chinese hamster cells in *vivo*. *International Journal of Radiation Biology*, (19):467–477, 1971.

[79] P. Wust, M. Seebass, J. Nadobny, P. Deuflhard, G. Monich, and R. Felix. Simulation studies promote technological development of radiofrequency phased array hyperthermia. *Int. J. Hyperth. (UK)*, 12(4):477–94, July – August 1996.

[80] Q.R. Zhong, C.K. Chou, J.A. McDougall, K.W. Chan, and K.H. Luk. Intracavitary hyperthermia applicators for treating nasopharyngeal and cervical cancers. *International Journal of Hyperthermia*, 6(6):997–1004, November – December 1990.

[81] M. Zimmermann, J. Schorcht, and W. Andree. Theoretical and experimental investigations of a newly developed intracavitary applicator system for the radiothermotherapy of gynaecological tumours. *International Journal of Hyperthermia*, 3(9):463–77, May – June 1993.

Author's publications related to the subject of this thesis

[82] M. Debicki, M. Mrozowski, and P. Debicki. Localized current field hyperthermia in carcinoma of the cervix: 3-d computer simulation of sar distribution. In *XII International Microwave Conference MIKON'98*, volume 3, pages 760–764, Kraków, May 1998.

[83] M. Debicki, M. Mrozowski, and P. Debicki. Application of multigrid method for quick simulation of sar and temperature distribution during hyperthermia treatment of cervical malignancies. In *15th Annual Review of Progress in Applied Computational Electromagnetics (ACES 99)*, pages 697–704, Naval Postgraduate School, Monerey, California, USA, March 15-20 1999.

[84] M.P. Debicki, M. Mrozowski, P.S. Debicki, J. Zielinski, N. Piotrkowicz, and Z. Petrovich. Localized current field hyperthermia in carcinoma of the cervix: 3-D computer simulation. In *Hyperthermia in Clincal Oncology*, page 41, Venice, Italy, May 28-30 1998.

[85] M. Debicki, M. Mrozowski, P. Debicki, J. Zieliński, N. Piotrkowicz, and Z. Petrovich. Localized current field hyperthermia in carcinoma of the cervix: 3-D computer simulation of SAR distribution. *International Journal of Hyperthermia*, 15(5):427–440, September – October 1999.